Novel methods for heavy-quark physics from lattice QCD

by

Justin Foley

B.A. (Mod.), M.Sc.

A Thesis submitted to
The University of Dublin
for the degree of

Doctor in Philosophy

School of Mathematics
University of Dublin
Trinity College

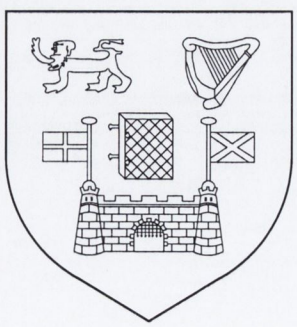

March, 2006

Declaration

This thesis has not been submitted as an exercise for a degree at any other University. Except where otherwise stated, the work described herein has been carried out by the author alone. This thesis may be borrowed or copied upon request with the permission of the Librarian, University of Dublin, Trinity College. The copyright belongs jointly to the University of Dublin and Justin Foley.

Signature of Author ..... Justin Foley .....

Justin Foley

22 March, 2006

Summary

The application of 3+1 anisotropic lattices to numerical simulations of hadrons containing heavy quarks is investigated. It is expected that using a fine temporal lattice spacing will suppress large mass-dependent errors which afflict discretisations of the Dirac action in the heavy-quark sector. An asymmetric discretisation of the Dirac action, specially formulated for anisotropic lattice, is used in this work.

Firstly, we consider the non-perturbative tuning of the quark anisotropy parameter in the quenched approximation. The anisotropy is easily tuned to a target value of 6.0 at the strange quark mass and shows negligible mass dependence up to the charm quark mass.

Secondly, the tuning of the fermion action is studied at one-loop in perturbation theory. For finite quark masses, this amounts to a determination of the rest mass renormalisation and the kinetic mass renormalisation of the lattice quark. The quantitative agreement between one-loop perturbation theory and numerical simulation is poor. However, much of the discrepancy can be attributed to two-loop effects which may be reduced by running on finer lattices or eliminated by performing further perturbative calculations.

Finally, we present results for a simulation of static-light hadrons on two-flavour dynamical background configurations. A new method was employed to evaluate the light quark propagators at all lattice sites. The resulting increase in statistics yields a dramatic improvement in signal compared to conventional point-propgator techniques. This study was performed on an anistropic lattice and the tuning of the quark and gauge anisotropies on dynamical configurations is described. We outline the construction of spatially-extended interpolating operators which are required to access orbitally-excited mesons. Numerical results show clear signals for the P-wave and D-wave states. The D-wave results may indicate the inversion of orbitally excited muliplets with respect to the usual atomic ordering, as has been predicted by quark models [56, 57]. Preliminary results are presented for static-light baryons.

Acknowledgements

First and foremost, I wish to thank to my supervisor Dr. Sinéad Ryan for her assistance, encouragement and enthusiasm over the past three years. Special thanks are also due to Dr. Mike Peardon who always found time to answer my questions. The work described in this thesis was done as part of a collaborative effort and, in particular, I would like to acknowledge the contributions of Alan, Bugra, Jimmy, Jon-Ivar and Richie. I have had a number of helpful discussions about lattice perturbation theory with Alessandra Feo and Giuseppe Burgio and I also wish to thank Ron Horgan and Quentin Mason for their hospitality and assistance. Thanks too to Martin for his advice on static quarks and his 'good afternoons'. I would also like to thank my officemates past and present Shane, Mick and Eoin for their good company. My housemates Matt, Azar and Mary also deserve considerable credit for keeping me sane this past year. Finally, I am very grateful for the financial support provided by an IRCSET Embark Initiative postgraduate award over the course of my Ph.D. studies.

To my family and friends.

Contents

List of Figures

List of Tables

Chapter 1

Introduction

Quantum Chromodynamics (QCD) is the accepted theory of the strong interaction. It describes the interaction of quarks through the exchange of gluons. A defining characteristic of QCD is that it is a confining theory, i.e., the strong coupling increases with decreasing energy scales. For this reason, under normal conditions, individual quarks and gluons are not observed in nature, rather they only appear in bound hadronic states. In the low-energy regime relevant to hadron physics, a perturbative treatment of QCD is not valid. However, lattice gauge theory can be used to make first-principles QCD predictions in the non-perturbative regime. The purposes of these calculations are two-fold. On one hand, lattice calculations will be able to confirm that QCD does describe the observed hadron spectrum. And secondly, more generally, hadronic matrix elements computed on the lattice will serve as inputs for tests of the Standard Model.

The energy scale at which the QCD coupling becomes strong is denoted Λ_{QCD} and is approximately 200 MeV. This scale naturally divides the quarks into two distinct sets. The light quarks are the up, down and strange quarks and they have masses that are less than Λ_{QCD}, while the charm, bottom and top quarks have masses that are much heavier than Λ_{QCD}. The ultimate aim of the work outlined in this thesis is the accurate simulation of heavy quark systems, i.e. hadrons which contain charm or bottom quarks.

This is an exciting time for heavy-quark physics. With regard to precision tests of the Standard Model, particular emphasis has been placed on the determination of the CKM matrix elements which parametrise the mixing of the quark mass eigenstates under the Weak interaction. A precise determination of these quantities will hint at sources of CP violation beyond the Standard Model. This will depend on accurate experimental data and precise theoretical inputs. The B-factories Babar and Bell are currently at the forefront of the experimental effort and additional B-physics data will become available when the LHC comes on-line in the near future. Accordingly, progress demands increasingly accurate lattice results for the heavy-quark sector. The high-precision charm data currently being generated at CLEO-c will test the predictive power of lattice QCD to an accuracy of $1 - 2\%$.

A response to these challenges must include a reappraisal of the techniques of lattice QCD, which forms the basis for this report. The research presented here concerns novel methods in lattice gauge theory and their application to heavy-quark simulations.

1.1 Thesis outline

The structure of the thesis is as follows:

- Chapter 2 describes some of the generic features of lattice QCD.
- The use of anisotropic lattices in numerical simulations is at the heart of the work described here, and the motivation for using anisotropic lattices and a description of the anisotropic formalism is given in Chapter 3.
- Chapter 4 reviews a non-perturbative determination of the bare anisotropy parameter in the fermion action. The study was performed on quenched background configurations which had previously been tuned for use in glueball spectroscopy.
- An analytic calculation of corrections to the fermion action at one-loop in lattice perturbation theory is described in Chapter 5. This is a generalisation of the calculation in Ref. [27] to anisotropic Symanzik-improved actions. However, unlike Ref. [27], this calculation was partially automated and twisted boundary conditions were employed to regulate intermediate infrared divergences.
- Finally, Chapter 6 details a study of orbitally-excited static-light hadrons on $N_f = 2$ dynamical background configurations. Similar studies can be found in Refs [58, 59]. Those investigations used all-to-all propagators for the light quark fields in order to obtain reasonable signals from static-light correlation functions. The work described here employed a new method of optimally estimating all-to-all propagators, which has been developed by the TrinLat Collaboration [45]. It was also the first such study performed on a dynamical anisotropic lattice, and our approach to operator construction differed from previous investigations and was designed to take advantage of static-light symmetries.

Chapter 2

QCD on a Computer

2.1 Discretising space-time

In order to study QCD on a computer, continuous space time is approximated by a hypercubic lattice of discrete points. For computational reasons, lattice QCD is formulated in Euclidean space time. The relative position of each lattice site is given by a four-vector x with components

$$x_\mu = n_\mu a_\mu, \quad n_\mu \in \mathcal{Z}, \quad 0 \leq n_\mu < N_\mu, \tag{2.1}$$

where a_μ is the lattice spacing along the direction denoted μ, and N_μ is the number of lattice sites along that direction.

The hypercubic lattice possesses a discrete translational symmetry which requires that energies and momenta occur in discrete units. The allowed momenta are

$$p_\mu = \frac{2\pi n_\mu}{N_\mu a_\mu}, \quad \text{(no summation)}. \tag{2.2}$$

Therefore, discretising space-time imposes a momentum cutoff corresponding to the minimum physical distance which can be modelled on a discrete grid and the lattice acts as an ultra-violet regulator for QCD.

2.2 Gauge fields on the lattice

The continuum QCD Lagrangian is formulated in terms of the vector potential, A_μ, which lies in the Lie algebra of SU(3). Transferring QCD to a discrete grid reduces the symmetries which constrain the continuum theory. It is essential, however, that the lattice formulation of QCD possesses an exact gauge symmetry. The loss of gauge invariance would mean that the quark-gluon, three-gluon and four-gluon couplings and the gluon mass would all have to be independently tuned in a simulation. This would make a numerical approach unfeasible.

A theory formulated in terms of the vector potential can possess only an approximate gauge symmetry at finite lattice spacing. In order to preserve an exact gauge invariance, the lattice theory is constructed from link variables: parallel transporters connecting adjacent sites on the lattice

$$\begin{aligned} U_\mu(x) &= \mathcal{P}\exp\left(i\int_x^{x+a_\mu\hat{\mu}} g_0 A_\mu(y)dy\right) \\ &\approx \exp\left(ig_0 a_\mu A_\mu\left(x+\frac{a_\mu\hat{\mu}}{2}\right)\right), \end{aligned} \tag{2.3}$$

where $\hat{\mu}$ denotes the unit vector in the direction labelled μ, $\mathcal{P}$ denotes path-ordering and g_0 is the bare gauge coupling. The link variables are elements of the gauge group and under a gauge transformation transform as

$$U_\mu(x) \to V(x)U_\mu(x)V^\dagger(x+a_\mu\hat{\mu}), \quad V(x) \in \mathrm{SU}(3). \tag{2.4}$$

This transformation property implies that the trace of the path-ordered product of link variables around a closed path, known as a Wilson loop, is gauge invariant. Lattice actions for the pure gauge sector are constructed from Wilson loops. The construction of gauge actions will be discussed in detail in Chapter 3.

2.3 Quarks on the lattice

The fermionic part of the continuum QCD action in Euclidean space is given by

$$\int d^4x \sum_f \bar{\psi}_f(\gamma_\mu D_\mu + m_f)\psi_f, \tag{2.5}$$

where the sum over quark flavours, f, is explicit while the Dirac and colour indices of the quark fields, ψ_f, have been suppressed. The Euclidean-space Dirac matrices are hermitian and satisfy

$$\{\gamma_\mu, \gamma_\nu\} = 2\delta_{\mu\nu}, \tag{2.6}$$

and the covariant derivative is

$$D_\mu = \partial_\mu - ig_0 A_\mu. \tag{2.7}$$

Quarks lie in the fundamental representation of the gauge group and the vector field appearing in the covariant derivative can be written

$$A_\mu = \sum_{a=1}^{8} A_\mu^a \frac{\lambda^a}{2}, \tag{2.8}$$

where A_μ^a are real-valued and the matrices, λ_a, are the 3×3 Gell-Mann matrices. Under a gauge transformation the quark fields and the covariant derivative transform as

$$\begin{aligned} &\psi(x) \to V(x)\psi(x), \quad \bar{\psi}(x) \to \bar{\psi}(x)V^\dagger(x), \\ &D_\mu\psi(x) \to V(x)D_\mu\psi(x), \quad V(x) \in \mathrm{SU}(3). \end{aligned} \tag{2.9}$$

Since the theory is relativistic, the action is invariant under Euclidean transformations, as well as space inversion, time reversal and charge conjugation. In addition,

for $m_f = 0$, the action is invariant under chiral transformations of the form

$$\psi(x) \rightarrow \exp(i\alpha\gamma_5)\psi(x), \quad \bar{\psi}(x) \rightarrow \bar{\psi}(x)\exp(i\alpha\gamma_5), \tag{2.10}$$

where α is a phase and γ_5 is a hermitian matrix which anti-commutes with the four Dirac matrices.

In nature, massless quarks do not exist. However, the u, d and s quarks are light enough to preserve an approximate chiral symmetry. A number of the lightest observed mesons (the pseudoscalar octet) is believed to be a set of Goldstone bosons generated by the spontaneous breaking of an approximate SU(3) chiral flavour symmetry.

A naive discretisation of the fermionic action for a single quark flavour is

$$S_f = \sum_x \bar{\psi}_f(x) M_f \psi_f(x) = \sum_x \bar{\psi}_f(x)(\gamma_\mu \nabla_\mu + m_f)\psi_f(x). \tag{2.11}$$

The action of the lattice covariant derivative on a quark field is

$$\nabla_\mu \psi(x) = \frac{1}{2a_\mu}[U_\mu(x)\psi(x+\hat{\mu}) - U_\mu^\dagger(x-\hat{\mu})\psi(x-\hat{\mu})]. \tag{2.12}$$

This symmetrised finite difference operator is anti-hermitian, which is necessary for a hermitian lattice Hamiltonian, and reproduces the continuum derivative to $\mathcal{O}(a^2)$. Unfortunately, this simple discretisation suffers from the fermion doubling problem. That is: in four dimensions, in the continuum limit, this action describes 16 degenerate quarks, the number of quarks doubling with each space-time dimension. This problem arises because, on the lattice, continuum derivatives are replaced by finite differences. The Fourier transforms of these operators are periodic functions of momentum. Therefore, although in the continuum, the momentum-space quark propagator has a single pole, on the lattice there are additional poles within the allowed range of momenta. The presence of these spurious states can make lattice simulations unworkable.

Theories describing a bosonic field, $\phi(x)$, do not suffer from doublers because they can be formulated in terms of single-step derivative operators

$$\partial_\mu^R \phi(x) = \frac{1}{a_\mu}[\phi(x+\hat{\mu}) - \phi(x)],$$
$$\partial_\mu^L \phi(x) = \frac{1}{a_\mu}[\phi(x) - \phi(x-\hat{\mu})], \tag{2.13}$$

and not the symmetrised derivative required to maintain unitarity in the fermionic theory. In momentum space, the resulting bosonic propagators are $2\pi/a_\mu$ periodic and do not have unphysical poles in the lattice Brillouin zone.

Removing the doublers is quite problematic. Their presence is a pathology of the lattice and they are strongly connected to chiral symmetry. In fact, the Nielsen-Ninomiya no-go theorem [1] states that it is impossible to construct a fermionic action which is simultaneously local, translationally invariant, hermitian, invariant under the chiral transformations in Eq. 2.10 and which does not suffer from doubling.

2.3.1 Wilson quarks

To solve the doubling problem, Wilson added a redundant operator to the naive quark action. The Wilson fermion matrix is given by

$$M_f^W = \gamma_\mu \nabla_\mu + m_f + \frac{r a_\mu}{2} \triangle_\mu, \tag{2.14}$$

where the second-order lattice derivative is defined as

$$\triangle_\mu \psi(x) = \frac{1}{a_\mu^2}[\psi(x+\hat{\mu}) + \psi(x-\hat{\mu}) - 2\psi(x)]. \tag{2.15}$$

This term solves the doubler problem by giving an additional mass to the spurious states. For a free fermionic theory at finite lattice spacing with the Wilson coefficient,

r, set to unity, the pole mass of the physical state is

$$m_{phys} = \frac{1}{a_t} \ln(1 + a_t m), \tag{2.16}$$

while the spatial doubler masses (on an isotropic lattice) are

$$m^n_{doubler} = \frac{1}{a_t} \ln(1 + a_t m + 2n), \quad n = 1, 2, 3. \tag{2.17}$$

These heavier doublers are less likely to contaminate lattice simulations. Their masses diverge as the continuum limit is taken; eventually the doublers become infinitely heavy and completely decouple from the theory.

The elimination of doublers comes at a price and the Wilson term breaks chiral symmetry at $\mathcal{O}(a)$. This is a real problem for light-quark simulations. Therefore, the alternative staggered formalism, which preserves a remnant of chiral symmetry, is commonly used for light quarks. The staggered formalism is itself problematic because it is not known if it can describe a local field theory, although numerical evidence is compelling [2, 3]. There exist formalisms, such as overlap and domain wall fermions, which satisfy the Ginsparg-Wilson definition of chiral symmetry [4] but these are very expensive and it will take some time before they can be widely used. In the meantime, Wilson-like discretisations can be used in studies of heavy-quark systems where the loss of chiral symmetry has less of an impact.

2.4 Numerical methods

On the Euclidean space-time lattice, the QCD partition function is given by

$$\mathcal{Z}_{QCD}^{\text{latt}} = \int DU D\bar{\psi} D\psi \exp\left(-S_F^{\text{latt}}(U, \bar{\psi}, \psi) - S_G^{\text{latt}}(U)\right), \tag{2.18}$$

where S_F^{latt} and S_G^{latt} are discretisations of the fermion and gauge actions respectively. Computationally, the fermionic part of this integral is problematic because it involves fields, $\bar{\psi}$, ψ, which anti-commute. However, these fields only appear in bilinear combinations in the fermion action and integration over the quark fields can be evaluated explicitly. This leads to the following expression for the partition function

$$\mathcal{Z}_{QCD}^{\text{latt}} = \int DU \prod_f \det\left(M_f(U)\right) \exp\left(-S_G^{\text{latt}}\right). \tag{2.19}$$

More generally, an arbitrary n-point vacuum expectation value can be written

$$\langle\Omega|\mathcal{O}_n(x_n).....\mathcal{O}_1(x_1)|\Omega\rangle = \frac{1}{Z_{QCD}^{\text{latt}}} \int DU \prod_f \det\left(M_f(U)\right) \mathcal{F}(U, M^{-1}(U)) \exp\left(-S_G^{\text{latt}}\right), \tag{2.20}$$

where the function $\mathcal{F}$ can be expressed in terms of the inverse fermion matrix and the link variables. Such integrals may be evaluated using importance sampling techniques. In this approach, an ensemble of background configurations is generated according to the probability density

$$P\left(U\right) = \prod_f \det\left(M_f(U)\right) \exp\left(-S_G^{\text{latt}}(U)\right). \tag{2.21}$$

An estimate of the n-point function is then obtained from the ensemble average of the function, $\mathcal{F}$, defined in Eq. 2.20.

2.5 The quenched approximation

The repeated evaluation of the non-local determinant of the fermion matrix, which is involved in the generation of background configurations, is computationally intensive and, until recently, it has been common practice to set the determinant to a constant in lattice simulations. This has the effect of excluding internal quark loops from the theory and is known as the quenched approximation.

There are limits on what can be computed in the quenched theory. For example, in full QCD, isosinglet mesons receive contributions from disconnected diagrams. The vacuum polarisation processes which generate these contributions do not occur in quenched QCD. Phenomenological arguments and comparison with experiment indicate that errors due to quenching are between 10 and 20 percent. In spite of this, quenched QCD has proven to be a valuable laboratory where lattice algorithms can be developed, where qualitative observations can be made and where systematic uncertainties can be studied and understood.

To simulate QCD exactly, internal quark loops need to be included. Because of the complexity of simulating full QCD, dynamical effects are still treated in an approximate way. For example, only two or three sea quark flavours may be considered; the contributions of heavier quarks to vacuum polarisation are thought to be small and are generally omitted [1]. Also, for practical reasons, the mass of the sea quarks may differ from the mass of the light valence quarks; this is called partially-quenched QCD. However, these approximations are expected to reproduce the bulk of the vacuum polarisation effects.

[1] Recently Nobes [10] has proposed a method of including heavy quark vacuum polarisation effects without incurring any additional computational costs. This approach uses the framework of an effective field theory to compute corrections to the gauge action.

2.6 Computing the hadron spectrum

Hadron energies are among the easier quantities to compute on the lattice; they can be determined from the two-point correlation function

$$C(t, \mathbf{p}) = \sum_{\mathbf{x}} e^{i\mathbf{p}\cdot\mathbf{x}} \langle \Omega | \mathcal{O}(\mathbf{x}, t) \mathcal{O}^{\dagger}(\mathbf{0}, 0) | \Omega \rangle, \tag{2.22}$$

where $\mathcal{O}$ is an interpolating operator for the hadron of interest. Inserting a complete set of energy-momentum eigenstates $\{|n\rangle\}$ yields

$$C(t, \mathbf{p}) = \sum_{n} \frac{1}{2E_n} |\langle \Omega | \mathcal{O} | n \rangle|^2 e^{-E_n(p)t}. \tag{2.23}$$

Assuming a discrete energy spectrum, as $t \to \infty$,

$$C(t, \mathbf{p}) \to \frac{1}{2E_n} |\langle \Omega | \mathcal{O} | n_0 \rangle|^2 e^{-E_0(p)t}, \tag{2.24}$$

where $|n_0\rangle$ is the lightest state which couples to the operator $\mathcal{O}$ and E_0 is the corresponding energy. Hadronic ground-state energies can therefore be computed by studying the corresponding two-point functions at large times.

In practice, one defines an effective mass by, for example,

$$a_t M_{\text{eff}}(t) = \ln \left(\frac{C(t, \mathbf{p})}{C(t+1, \mathbf{p})} \right). \tag{2.25}$$

At sufficiently large times, the effective mass converges to the ground-state energy; this manifests itself as a plateau in a plot of the effective mass as a function of t. The coefficients of the sum of exponentials in Eq. 2.23 are real-valued and positive, and, in this case, M_{eff} converges monotonically from above. This information is of practical significance because, with the exception of the pion correlator, statistical noise in lattice two-point correlators grows with t. Therefore, effective mass plateaux can be noisy and difficult to resolve to a high accuracy; some insight into the expected

behaviour of the effective mass can help in determining a plateau.

2.6.1 Meson correlators from point propagators

Among the simplest interpolating operators on the lattice are local meson operators which take the form

$$\mathcal{O}(x) = \bar{\psi}_f(x)\Gamma\psi_g(x), \tag{2.26}$$

where Γ is an element of the Dirac algebra and f, g are flavour indices. For simplicity, we have omitted the possibility of a sum over quark flavours.

To illustrate how the two-point function in Eq. 2.22 may be computed numerically, we first consider the meson propagator from the origin to another space-time point $x \equiv (t, \mathbf{x}); t \geq 0$,

$$G(t, \mathbf{x}) = \langle\Omega|\mathcal{O}(x)\mathcal{O}^\dagger(0)|\Omega\rangle \quad = \quad \langle\Omega|\bar{\psi}_f(x)\Gamma\psi_g(x)\bar{\psi}_g(0)\Gamma^\dagger\psi_f(0)|\Omega\rangle. \tag{2.27}$$

Wick contracting the quark fields, this function can be reexpressed in terms of fermion propagators

$$G(t, \mathbf{x}) = -\langle Tr(S_f(0, x)\Gamma S_g(x, 0)\Gamma^\dagger)\rangle + \delta_{fg}\langle Tr(\Gamma S_f(x, x))Tr(\Gamma^\dagger S_f(0, 0))\rangle. \tag{2.28}$$

$S_f(y, x)$ is the fermion propagator from x to y, which can be computed numerically by inverting the fermion matrix on a given background configuration, $S_f(y, x; U) = M_f(y, x; U)^{-1}$. The angle brackets denote an average over background configurations. The fermion propagator satisfies the hermiticity relation

$$S_f(x, y) \equiv \gamma_5 S_f(y, x)^\dagger \gamma_5. \tag{2.29}$$

Assuming a flavour non-singlet state, $f \neq g$, Eq. 2.27 can therefore be rewritten as

$$G(t, \mathbf{x}) = -\langle Tr(\gamma_5 S_f(x,0)^\dagger \gamma_5 \Gamma S_g(x,0)\Gamma^\dagger)\rangle, \tag{2.30}$$

and the meson correlation function at fixed momentum $\mathbf{p}$ is given by

$$C(t, \mathbf{p}) = \sum_{\mathbf{x}} e^{i\mathbf{p}\cdot\mathbf{x}} G(t, \mathbf{x}) = -\sum_{\mathbf{x}} e^{i\mathbf{p}\cdot\mathbf{x}} \langle Tr(\gamma_5 S_f(x,0)^\dagger \gamma_5 \Gamma S_g(x,0)\Gamma^\dagger)\rangle. \tag{2.31}$$

Therefore, the correlator can be constructed from point-propagators connecting the origin to all other sites on the lattice. Practically, this amounts to computing a single column (in space-time indices) of the inverse fermion matrix on each gauge configuration

$$\{M_f(x, 0; U)^{-1}\}. \tag{2.32}$$

This can be done using a conjugate-gradient algorithm.

Conversely, the disconnected contributions to flavour-neutral mesons require $S_f(x, x)$ at all sites on the lattice. Effectively, this means that the inverse of the full fermion matrix must be computed on each background configuration. In this case, standard inversion algorithms like the conjugate-gradient method are prohibitively expensive. In Chapter 6, a new method of stochastically estimating the inverse of the full fermion matrix will be discussed and put to practical use.

2.7 Symanzik's improvement program

In the limit as the lattice spacing goes to zero, the lattice theory defined by the Wilson quark action must reproduce continuum QCD. Although this limit can never be reached, at sufficiently small lattice spacing a scaling regime is reached. As the lattice spacing is reduced, measurements of physical quantities become independent of the details of the lattice formulation and reliable extrapolations to the continuum limit can be made.

There are, however, practical restrictions, (outlined in Chapter 3) on the minimum lattice spacing which can be used in simulations. One is therefore interested in constructing lattice operators which minimise the deviation from scaling at moderate lattice spacing.

Symanzik [5, 6] was the first to introduce a systematic method to quantify and correct cutoff effects in a lattice theory. He showed that a lattice theory can be described by a local effective Lagrangian, consisting of the renormalised continuum Lagrangian plus a linear combination of local lattice operators. These operators are multiplied by appropriate powers of the lattice spacing, a. In Symanzik's approach, the effective Lagrangian is expanded in powers of the lattice spacing.

$$\begin{aligned} S_{\text{latt}} &= \int d^4x \mathcal{L}_{\text{eff}}, \\ \mathcal{L}_{\text{eff}} &= \mathcal{L}_{QCD} + a \sum_i c_i^{(1)} \mathcal{O}_i^{(1)} + a^2 \sum_i c_i^{(2)} \mathcal{O}_i^{(2)} + ..., \end{aligned} \tag{2.33}$$

where $\{\mathcal{O}_i^{(n)}\}$ denotes the set of lattice operators of dimension $n+4$. Although, at non-zero lattice spacing, this expansion has an infinite number of terms, each term contains contributions from a finite number of operators permitted by the lattice symmetries. Therefore, in principle, it is possible to eliminate terms of a given order in a in the local effective Lagrangian by the inclusion of redundant operators in the lattice Lagrangian. At sufficiently small lattice spacing, the dominant lattice artifacts are contained in the lower-order terms of the expansion; the coefficients,

$c_i^{(n)}$, are determined by physics above the lattice cutoff and can be computed in perturbation theory. Systematically eliminating lattice artifacts order by order in a, brings the lattice theory 'closer' to the continuum limit. Lattice operators used to perform physical measurements can be improved in a similar fashion.

Symanzik studied the ϕ^4 theory [5] and the non-linear sigma model [6] and, in these cases, improvement can be implemented such that all Green's functions calculated in the improved theory are closer to the continuum. The extension of this program to a gauge theory is more involved. Lüscher and Weisz [7, 8, 9] were among the first to apply Symanzik's method to a lattice gauge theory. They found that it was necessary to relax the improvement conditions. Rather than demanding the improvement of all Green's functions, they tuned the lattice theory by requiring that only on-shell quantities be improved. The on-shell improvement program has been crucial to the development of lattice gauge theory.

Chapter 3

Anisotropic lattice QCD

3.1 Motivation

Conventionally, lattice simulations have been performed on isotropic lattices which have the same lattice spacing along each space-time direction. The isotropic formalism is the simplest space-time discretisation scheme. However, there are a number of reasons for formulating QCD on anisotropic lattices.

Quantum field theories are extremely complex and are difficult to simulate numerically. In order to accurately model QCD on a computer the lattice spacing should be much smaller than the typical length scales of the system under investigation while the lattice must be large enough to accommodate the system. For example, in Wilson's original formulation, lattice spacings as small as $0.05 - 0.1$ fm are necessary to reliably simulate QCD. Conversely, a spatial volume of approximately $(2\text{ fm})^3$ is required to realistically model a single meson, while a baryon may need about $(3\text{ fm})^3$. The computational cost of a lattice simulation increases linearly with the number of grid points. In addition, the algorithms used in the numerical integration undergo a 'critical slowing down' as the lattice spacing is decreased making this brute force approach to error control unfeasible. In many cases the use of improved lattice operators has made it possible to simulate QCD on much coarser lattices, however, there still exist a number of applications where the accuracy of numerical simulations is

severely constrained by limited computational resources.

Some of these computational limitations can be circumvented by using asymmetric lattices. For example, using a finer lattice spacing in the temporal direction, a_t, than in the spatial directions, a_s, gives improved resolution of correlation-function decays with a minimal increase in computational workload. This offers a particular advantage in studies of heavy hadrons where effective mass plateaux rapidly degenerate into noise. In particular, the $3+1$ anisotropic lattice has been used with great success in studies of the glueball spectrum [16].

Similarly, $3+1$ anisotropic lattices have been used in finite temperature QCD in order to make precise measurements of temperature-dependent transitions.

Much of this thesis explores the application of anisotropic lattices to the simulation of heavy quarks. Simulations of systems containing heavy quarks are problematic because discretising the Dirac action leads to lattice artifacts which scale as am_Q where m_Q is the quark mass. Since, in order to control these errors, we require that $a \ll 1/m_Q$, it is not presently possible to accurately simulate systems containing a relativistic bottom quark using standard discretisations of the Dirac action on an isotropic lattice.

Effective theories which do not suffer from large mass-dependent discretisation errors have proven more successful. For example, lattice NRQCD (Non-relativistic QCD) [11, 12] has been used with particular success in b-quark simulations. The effective action can be expanded in an infinite series of operators allowed by the symmetries of the lattice. In NRQCD, the action is written as an expansion in powers of the velocity of the heavy quark which is small and therefore higher order terms are expected to make successively smaller contributions to the quantities of interest. The coefficients of the leading order terms in the expansion can be computed by matching scattering amplitudes in the effective theory and continuum QCD. This matching is usually performed using perturbation theory. Lattice perturbation theory is extremely complicated and calculations are not often performed beyond the level of one or two loops. The accuracy of the effective theory is therefore limited both

by the truncation in the expansion of the effective action and by the perturbative determination of the expansion coefficients. Also, the continuum limit of lattice NRQCD is not well-defined since the effective theory depends on the lattice to provide an ultra-violet cutoff. One therefore relies on matching calculations to eliminate lattice artifacts and is constrained to work in a window where $m_Q a \gtrsim 1$.

On the other hand, the Fermilab approach [26], which is based on a non-relativistic interpretation of the Wilson fermion action, holds over the full range of quark masses and does have a well-defined continuum limit. The price one pays for this, is the introduction of a large number of irrelevant terms in the fermion action. The coefficients of these terms must be tuned in a mass-dependent way.

Using anisotropic lattices, it appears possible to accurately simulate relativistic heavy quarks with the computing resources which are currently available. This approach uses a discretisation of the Dirac action specifically formulated for the $3+1$ anisotropic lattice. In this formulation, to lowest order in the strong coupling, mass-dependent cutoff effects appear only in the combination $a_t m_Q$. These can be controlled by making the temporal direction sufficiently fine. Lattice artifacts which arise from the discretisation of the spatial directions couple to the three-momentum of the heavy quark. Since the heavy-quark momentum is quite small, a relatively coarse lattice spacing can be used along the spatial directions.

3.2 Anisotropic gauge actions

The simplest gauge action is constructed from the smallest Wilson loop allowed on the lattice, the plaquette

$$P_{\mu\nu}(x) = U_\mu(x)U_\nu(x+\hat{\mu})U_\mu^\dagger(x+\hat{\nu})U_\nu^\dagger(x). \tag{3.1}$$

Using Taylor's theorem, we can express the plaquette as an expansion in powers of the lattice spacing

$$P_{\mu\nu} = 1 + ia_\mu a_\nu g_0 F_{\mu\nu} - \frac{a_\mu^2 a_\nu^2}{2} g_0^2 F_{\mu\nu}^2 + \mathcal{O}(a^6). \tag{3.2}$$

For link variables in the fundamental representation of SU(3), the Wilson gauge action on the $3+1$ anisotropic lattice is written

$$S_g^W = \frac{\beta}{\xi_g}\Omega_s + \beta\xi_g\Omega_t = \frac{1}{2}\int d^4x \mathrm{Tr}\left(\mathrm{F}_{\mu\nu}^2\right) + \mathcal{O}(\mathrm{a_s^2}, \mathrm{a_t^2}), \tag{3.3}$$

where

$$\Omega_s = \sum_x \sum_{i<j} \frac{1}{3} \text{ Re Tr}[1 - P_{ij}(x)] \tag{3.4}$$

and

$$\Omega_t = \sum_x \sum_i \frac{1}{3} \text{Re Tr}[1 - P_{ti}(x)]. \tag{3.5}$$

ξ_g is the bare anisotropy, at the tree-level $\xi_g = a_s/a_t$, and $\beta = 6/g_0^2$ where, once again, g_0 is the bare coupling constant. It is worth noting that the bare coupling constant and the lattice spacing are not independent parameters; they are related by renormalisation group arguments. Higher values of β correspond to finer lattice spacings and in the continuum limit $g_0 = 0$.

Having detailed the construction of the simplest anisotropic lattice gauge action,

we now describe the modified gauge action used in our simulations. To improve scaling, this action incorporates the modifications described in the following sections.

3.2.1 Symanzik improvement of the gauge action

From Eq. 3.3, it is clear that in order to remove leading-order discretisation effects in the gauge action, operators of dimension 6 must be considered. There are 18 independent dimension-6 operators which satisfy gauge invariance and the symmetries of the anisotropic lattice. All of these can be constructed from linear combinations of the plaquettes and 6-link loops of the form shown in Figure 3-1.

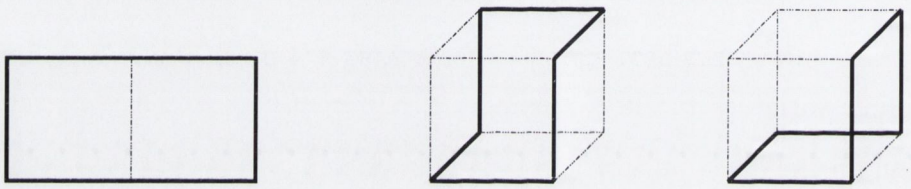

Figure 3-1: The six-link loops required to improve the gauge action to $\mathcal{O}(a^4)$. Only the rectangular loop is used in the construction of the anisotropic improved gauge action

Because of the large number of allowed operators there is some freedom in the choice of the operator coefficients. The criteria for choosing the coefficients are

- Additional terms in the gauge action should remove leading-order discretisation effects.
- The implementation of these additional terms in code should not significantly slow down the generation of gauge configurations.
- The improved action should retain the good properties of the simpler implementation such as reflection positivity. [1]

[1] In Euclidean space-time, a function F of the fields is said to be reflection positive if it satisfies $\langle \Theta\left(\overline{F}\right), F\rangle \geq 0$, where Θ denotes time reflection and $\overline{F}$ is the complex conjugate of F. The positivity of gauge-invariant observables of the lattice theory is required in order to define a positive transfer operator connecting adjacent timeslices on the lattice. If full reflection positivity is not realised it may still be possible to construct a positive transfer operator over two timeslices. However, the spectrum of the corresponding Hamiltonian may contain ghost states, lattice artifacts which can adversely affect numerical simulations.

Inclusion of bent-rectangle operators is not compatible with the second criterion listed above and the two-time-slice rectangle violates reflection positivity. Unfortunately, it is not possible to exclude all of these operators and remove all $\mathcal{O}(a^2)$ errors. However, since the action is designed for an anisotropic lattice, the improvement condition may be relaxed and $\mathcal{O}(a_t^2)$ errors can be ignored.

One action which satisfies the relaxed improvement condition and does not include bent-rectangular loops or two-timeslice rectangles is

$$S_g = \frac{\beta}{\xi_g}\left\{\frac{5}{3}\Omega_s - \frac{1}{12\xi_g}\Omega_s^{(R)} + \frac{4\xi_g}{3}\Omega_t - \frac{\xi_g}{12}\Omega_t^{(R)}\right\}. \tag{3.6}$$

The six-link terms are

$$\begin{aligned}\Omega_s^{(R)} &= \sum_x \sum_{i\neq j} \frac{1}{3}\text{Re Tr}[1 - R_{ij}(x)],\\ \Omega_t^{(R)} &= \sum_x \sum_i \frac{1}{3}\text{Re Tr}[1 - R_{it}(x)],\end{aligned} \tag{3.7}$$

where

$$R_{\mu\nu}(x) = U_\mu(x)U_\mu(x+\hat{\mu})U_\nu(x+2\hat{\mu})U_\mu^\dagger(x+\hat{\mu}+\hat{\nu})U_\mu^\dagger(x+\hat{\nu})U_\mu^\dagger(x). \tag{3.8}$$

3.2.2 Tadpole improvement

So far, we have only considered tree-level improvement of the gauge action; calculating the improvement coefficients at higher orders in perturbation theory quickly becomes extremely complicated. However, there exists a very simple procedure called mean field or tadpole improvement which can capture the bulk of these radiative corrections and drastically reduce discretisation errors.

The motivation for tadpole improvement came from investigations into the failure of early lattice perturbative calculations to reproduce the results of numerical simulations. Although calculations in continuum QCD indicated that perturbation theory

should be reliable at lattice spacings as large as 0.5 fm, large discrepancies were observed between simulation results and perturbative calculations above 0.05 fm.

Parisi [13] and Lepage and Mackenzie [14] realised that these discrepancies arose because of the choice of the bare lattice coupling as the expansion parameter in perturbative calculations.

Because the lattice theory is formulated in terms of link variables, which have an asymptotic expansion in powers of the coupling, lattice Feynman rules include an infinite number of gluon vertices that have no continuum analogue. These result in tadpole interactions which are purely lattice artifacts. Naively, one would expect the contributions of these tadpole interactions to be suppressed by powers of the lattice spacing and, therefore, to be quite small on moderately fine lattices. However, contracting the gauge fields in tadpole diagrams generates divergences which cancel exactly the lattice spacing suppression. Thus, the assumption that radiative corrections to the bare lattice coupling are small and that it is therefore a good expansion parameter for perturbative calculations is incorrect.

The simple remedy suggested was to reformulate the lattice theory in terms of rescaled link variables

$$U_t \to \frac{U_t}{u_t}, \quad U_i \to \frac{U_i}{u_s} \tag{3.9}$$

where

$$u_{s(t)} = \left\langle \frac{1}{3} \text{Re Tr} U_{i(t)} \right\rangle \tag{3.10}$$

contain most of the tadpole contributions. Tadpole improved lattice operators are considerably closer to their continuum counterparts and further improvement beyond the tree-level is often unnecessary.

The tadpole coefficients can be determined directly from simulations but this requires gauge-fixing. In practice, u_s is computed by inserting a trial value into the

action. This trial value is varied until it agrees with the value determined from the fourth root of the expectation value of the spatial plaquette

$$u_s \approx \left\langle \frac{1}{3} \mathrm{Re\ Tr} P_{ij} \right\rangle^{\frac{1}{4}}. \tag{3.11}$$

Once u_s has been fixed, u_t can be computed from the temporal plaquette. However, on highly anisotropic $3+1$ lattices, u_t is expected to be very close to unity (this will later be verified at 1-loop in perturbation theory) and, in all our simulations, we have set $u_t = 1$.

3.2.3 The addition of an adjoint term

The actions considered so far have been constructed from Wilson loops in the fundamental representation of SU(3). However, a general gauge action may involve a sum over representations.

Studies using gauge actions containing both fundamental and adjoint terms have shown the presence of a line of first-order phase transitions in the phase space of the fundamental and adjoint coupling constants [15]. This line crosses the adjoint axis into the first quadrant of the phase plane at a positive value of the adjoint coupling, β_A. The line ends in a second-order phase transition above the fundamental axis. There are no singularities along the positive fundamental coupling (β_F) axis and, in principle, it is safe to take the continuum limit along this line. However, some values of β_F typically used in simulations are quite close to the critical point. The results of simulations performed at these values of the coupling show the effects of this unphysical fixed point. For example, this was the reason for the 'scalar dip' observed in early investigations of the glueball spectrum by Morningstar and Peardon [16]. They used the improved gauge action and anisotropic lattices with rather coarse spatial lattice spacing (0.2 – 0.4 fm). They found that the mass of the scalar glueball, measured in lattice units, fell as the spatial lattice spacing was increased. The mass reached a minimum at $a_s \approx 0.25$ fm before rising again. The scalar glueball is the

lightest mass particle in the pure gauge sector of QCD and the dip was caused by the divergence of the correlation length close to the critical point.

To circumvent this problem, an adjoint-like term constructed from the product of two spatial plaquettes separated by a single time-slice

$$\Omega_s^{(2t)} = \frac{1}{2}\sum_{x,i>j}\left\{1 - \frac{1}{9}\mathrm{Re\ Tr}P_{ij}(x)\mathrm{Re\ Tr}P_{ij}(x+\hat{t})\right\} \tag{3.12}$$

was added to the action. This operator has an identical expansion in powers of the lattice spacing to Ω_s, up to $\mathcal{O}(a^4)$. Making the replacement

$$\Omega_s \to (1+\omega)\Omega_s - \omega\Omega_s^{(2t)} \tag{3.13}$$

in the gauge action is therefore compatible with tree-level Symanzik improvement. Choosing the free parameter ω to be positive allows us to run simulations below the fundamental axis, well away from the critical point. The exact form of the gauge action used in our simulations is

$$\begin{aligned} S_\omega &= \frac{\beta}{\xi_g}\left\{\frac{5(1+\omega)}{3u_s^4}\Omega_s - \frac{5\omega}{3u_s^8}\Omega_s^{(2t)} - \frac{1}{12u_s^6}\Omega_s^{(R)}\right\} \\ &\quad +\beta\xi_g\left\{\frac{4}{3u_s^2u_t^2}\Omega_t - \frac{1}{12u_s^4u_t^2}\Omega_t^{(R)}\right\}. \end{aligned} \tag{3.14}$$

3.3 Anisotropic fermion actions

Initial investigations into the application of anisotropic lattices to heavy quark simulations considered the anisotropic Sheikholeslami-Wohlert (SW) action. The SW action differs from the Wilson quark action by the inclusion of an $\mathcal{O}(a)$ improvement term, the so-called clover term. In Ref. [17], the free quark dispersion relation for the anisotropic SW action was studied. At low spatial momenta, the lattice energy-momentum relation should reproduce the continuum relativistic expression, $E^2 = M^2 + \mathbf{p}^2$, and mass-dependent corrections to this form were examined. It was found that, although the spatial Wilson parameter (r_s) can be tuned to remove large $a_s m_Q$ errors, at large anisotropies this tuning can lead to the reintroduction of doublers in numerical simulations. The authors conclude that anisotropic lattices are useful in charm-quark simulations, where only a moderate anisotropy, $\xi \approx 3$, is needed. However, for the SW action, the reappearance of doublers spoil simulations at the anisotropies required to accurately simulate relativistic b-quarks.

3.3.1 Anisotropic Rotated Improved fermion Action (ARIA)

We use an asymmetric Wilson-type action which has been specifically designed for large anisotropies, i.e. $\xi \geq 5$. In the case of the SW action, large $a_s m_Q$ corrections to the energy-momentum relation can arise from the cross-term of the contribution from the spatial Wilson term and the bare quark mass. The Wilson term is a dimension 5 operator and can significantly affect the low-momentum behaviour of the lattice theory. The action used in our simulations is Symanzik-improved and incorporates a dimension 7 operator to control spatial doublers. The contribution of this higher-order term is strongly suppressed by powers of the lattice spacing and it has a much milder effect on the low-momentum analysis than the Wilson term.

To construct the lattice action, we first consider the continuum fermion action

and apply rotations to the quark fields

$$\begin{aligned}\psi_r &= [1 - \frac{ra_t}{4}(\gamma_0 D_0 - m)]\psi, \\ \bar{\psi}_r &= \bar{\psi}[1 - \frac{ra_t}{4}(\gamma_0 D_0 - m)].\end{aligned} \tag{3.15}$$

At the tree-level, this is an isospectral transformation, leaving physical observables unchanged; at the quantum level, the Jacobian of this transformation does modify the path integral measure, but here we consider only tree-level improvement. The rotated continuum action is given by

$$\begin{aligned}S_r &= \bar{\psi}_r M_0 \psi_r \\ &\quad -\frac{ra_t}{2}\bar{\psi}_r\{D_0^2 + \gamma_0 D_0 \gamma_i D_i - m(\gamma_i D_i + m)\}\psi_r \\ &\quad -\frac{ra_t}{4}\bar{\psi}_r\{D_0^2 + \gamma_i D_i \gamma_0 D_0 - m(\gamma_i D_i + m)\}\psi_r \\ &\quad +\mathcal{O}(a_t^2),\end{aligned} \tag{3.16}$$

where $M_0 = \gamma_\mu D_\mu + m$. For simplicity, the integral over space-time has been dropped but it is implied. The fermion action can be written more concisely by introducing

$$M_r = \mu_r \gamma_i D_i + \gamma_0 D_0 + \mu_r m, \tag{3.17}$$

where $\mu_r = (1 + \frac{1}{2} r a_t m)$. Up to corrections of $\mathcal{O}(a_t^2)$ the continuum action is

$$S_r = \bar{\psi}_r M_r \psi_r - \frac{ra_t}{2}\bar{\psi}_r \left(D_0^2 - \frac{g}{2}\sigma_{i0} F_{i0}\right)\psi_r, \tag{3.18}$$

where the chromoelectric field F_{i0} is defined as

$$F_{i0} = -\frac{i}{g}[D_i, D_0], \tag{3.19}$$

and σ_{i0} is given by $\sigma_{\mu\nu} = \dfrac{1}{2i}[\gamma_\mu, \gamma_\nu]$.

The lattice action is constructed by discretising the rotated continuum action.

Discretising D_0^2 yields a Wilson term which eliminates temporal doublers, however, because this term is generated by a continuum field rotation, the lattice dicretisation is accurate to $\mathcal{O}(a_t)$. Following the work of Hamber and Wu [18], a higher-order irrelevant operator is introduced to remove spatial doublers

$$S_q = \bar{\psi}_r M_r \psi_r - \frac{r a_t}{2} \bar{\psi}_r \left(D_0^2 - \frac{g}{2} \sigma_{i0} F_{i0} \right) \psi_r + s a_s^3 \bar{\psi}_r \sum_i D_i^4 \psi_r, \tag{3.20}$$

where the positive real-valued coefficient, s, is analogous to the Wilson coefficient, r.

Since this action is intended for use on relatively coarse spatial lattice spacings, to eliminate $\mathcal{O}(a_s^2)$ cutoff errors an improved discretisation is used for the kinetic terms in the spatial directions, $\gamma_i D_i$. Neglecting the link variables, this improved lattice derivative is given by

$$\begin{aligned} \nabla_\mu^{imp} \phi(x) &= \frac{1}{a_\mu} \left\{ \frac{2}{3} [\phi(x+\hat{\mu}) - \phi(x-\hat{\mu})] - \frac{1}{12} [\phi(x+2\hat{\mu}) - \phi(x-2\hat{\mu})] \right\} \\ &= \frac{\partial \phi(x)}{\partial x_\mu} + \mathcal{O}(a_\mu^4). \end{aligned} \tag{3.21}$$

The Hamber-Wu term is discretised as

$$\begin{aligned} \triangle_\mu^{HW} \phi(x) &= \frac{1}{a_\mu^4} \{ [\phi(x+2\hat{\mu}) + \phi(x-2\hat{\mu})] \\ &\quad -4[\phi(x+\hat{\mu}) - \phi(x-\hat{\mu})] + 6\phi(x) \}. \end{aligned} \tag{3.22}$$

The chromoelectric field, F_{i0}, is constructed from a combination of four plaquettes in the $i-t$ plane. Including tadpole improvement, it is given by

$$g F_{i0} = \frac{1}{\xi_q a_t^2} \frac{1}{u_s^2 u_t^2} \frac{1}{8i} \left\{ C_i(x) - C_i^\dagger(x) \right\}, \tag{3.23}$$

where ξ_q is the quark field anisotropy, at tree-level $\xi_q = \xi_g$, and the clover operator is

$$\begin{aligned} C_i(x) &= U_i(x)U_t(x+\hat{\imath})U_i^\dagger(x+\hat{t})U_t^\dagger(x) \\ &\quad + U_t(x)U_i^\dagger(x-\hat{\imath}+\hat{t})U_t^\dagger(x-\hat{\imath})U_i(x-\hat{\imath}) \\ &\quad + U_i^\dagger(x-\hat{\imath})U_t^\dagger(x-\hat{\imath}-\hat{t})U_i^\dagger(x-\hat{\imath}-\hat{t})U_t(x-\hat{t}) \\ &\quad + U_t^\dagger(x-\hat{t})U_i(x-\hat{t})U_t(x+\hat{\imath}-\hat{t})U_i^\dagger(x). \end{aligned} \tag{3.24}$$

Finally, including link variables and tadpole improvement coefficients, the fermion matrix can be written

$$\begin{aligned} M_q\psi(x) &= \frac{1}{a_t}\left\{\left(\mu_r m a_t + \frac{18s}{\xi_q} + r + \frac{r a_t^2 g}{4}\sigma_{i0}F_{i0}\right)\psi(x)\right. \\ &\quad -\frac{1}{2u_t}\left[(r-\gamma_0)U_t(x)\psi(x+\hat{t}) + (r+\gamma_0)U_t^\dagger(x-\hat{t})\psi(x-\hat{t})\right] \\ &\quad -\frac{1}{\xi_q}\sum_i\left[\frac{1}{u_s}\left(4s - \frac{2}{3}\mu_r\gamma_i\right)U_i(x)\psi(x+\hat{\imath}) + \frac{1}{u_s}\left(4s + \frac{2}{3}\mu_r\gamma_i\right)U_i^\dagger(x-\hat{\imath})\psi(x-\right. \\ &\quad -\frac{1}{u_s^2}\left(s - \frac{1}{12}\mu_r\gamma_i\right)U_i(x)U_i(x+\hat{\imath})\psi(x+2\hat{\imath}) \\ &\quad \left.\left.-\frac{1}{u_s^2}\left(s + \frac{1}{12}\mu_r\gamma_i\right)U_i^\dagger(x-\hat{\imath})U_i^\dagger(x-2\hat{\imath})\psi(x-2\hat{\imath})\right]\right\}. \end{aligned} \tag{3.}$$

In the remainder of the thesis this asymmetric fermion action is referred to as ARIA. The acronym ARIA stands for Anisotropic Rotated Improved Action.

Chapter 4

Tuning anisotropies in the quenched approximation

In the description of Symanzik improvement it was mentioned that, for sufficiently fine lattice spacings, the coefficients in a lattice action could be computed perturbatively. However, it is also possible to tune some of the parameters non-perturbatively in lattice simulations. Action couplings can, for example, be tuned to restore a continuum symmetry, such as Euclidean invariance. This approach is preferable to a perturbative determination of the action parameters because it can correct for non-perturbative effects and because additional corrections to the couplings computed in this way only appear at higher orders in the lattice spacing.

The anisotropic formalism introduces two additional parameters, the quark and gauge anisotropies, ξ_q and ξ_g. As stated in Chapter 3, at the tree-level, these parameters are equal to the aspect ratio of the spatial and temporal lattice spacings, i.e. $\xi = \frac{a_s}{a_t}$. When the effects of radiative corrections are included, these parameters have to be tuned in a self-consistent way so that the renormalised anisotropies, ξ_q^R, ξ_g^R measured in simulations agree at some target value. In full QCD simulations this is quite a challenge. Because both the quark and gauge anisotropies enter into the generation of gauge configurations, they have to be tuned simultaneously. The tuning procedure for dynamical fermions will be outlined in Chapter 6.

Here, we describe how the anisotropy parameters can be tuned in the quenched approximation. This is considerably easier than in full QCD because the gluon anisotropy can first be tuned by considering the pure gauge sector. Once ξ_g has been fixed, fermions can be introduced and ξ_q may be determined.

4.1 The gauge anisotropy

In our work, the anisotropy for the pure Yang-Mills sector was determined from the static-interquark potential measured along coarse and fine directions [21]. In this method, the anisotropy is tuned by demanding that the measurements along the coarse and fine directions yield the same function of physical distance.

The (coarse) z-direction is chosen to be time and the interquark potentials are determined by measuring

$$a_s V_s(\mathbf{x}, z) = \ln\left(\frac{W_{ss}(\mathbf{x}, z)}{W_{ss}(\mathbf{x}, z+1)}\right), \quad a_s V_t(t, z) = \ln\left(\frac{W_{ts}(t, z)}{W_{ts}(t, z+1)}\right), \tag{4.1}$$

where $W_{ss}(\mathbf{x}, z)$ is a Wilson-loop in the coarse directions and $W_{ts}(t, z)$ involves the time direction. As $z \to \infty$, $V_s(\mathbf{x}, z) \to V_s(|\mathbf{x}|)$ and $V_t(t, z) \to V_t(t)$.

We tune the gauge anisotropy by first choosing a target value ξ, and then determining the input, ξ_g. To determine this input anisotropy, $V_s(|\mathbf{x}|)$ and $V_t(t)$ are computed for a fixed physical distance $r = |\mathbf{x}| = t$. The target anisotropy satisfies

$$r = n_r a_s = \xi n_r a_t, \quad n_r \in \mathcal{Z} \tag{4.2}$$

and ξ_g is tuned such that

$$V_s(n_r a_s) = V_t(\xi n_r a_t). \tag{4.3}$$

For the Symanzik and tadpole improved anisotropic gauge action, this method of calculating the anisotropy parameter was compared to the determination from the

dispersion relation of the torelon in Ref. [22]. If the anisotropic formalism is to be of any practical use, different determinations of the anisotropy parameter must agree to a high precision, and, in that case, the results of the two methods differed by at most 4%.

4.2 A non-perturbative determination of the quark anisotropy

To tune the quark anisotropy, the properties of hadronic bound states which contain quarks need to be considered. The renormalised anisotropy can, for example, be determined from the dispersion relation of a relativistic meson or baryon. In lattice simulations, energy and momentum appear only in the dimensionless combinations, $\hat{E} = a_t E$ and $\hat{p} = a_s p$. In terms of these variables, the relativistic dispersion relation is

$$\hat{E}^2(\mathbf{p}) = \hat{E}^2(\mathbf{0}) + \left(\frac{\hat{\mathbf{p}}}{\xi_q^R}\right)^2 + \mathcal{O}(p^4). \tag{4.4}$$

The renormalised anisotropy, ξ_q^R, is therefore given by the slope of the energy-momentum relation at low spatial momentum.

This section details an investigation into the calibration of the quark anisotropy parameter using meson dispersion relations. The main considerations in this study are

1. The uncertainty in the determination of the anisotropy.

   This includes statistical uncertainty and systematic errors. In order to quantify systematic errors a number of different mesons were considered.

2. The dependence of the renormalised anisotropy on the quark mass.

   Our principal motivation for using anisotropic lattices was to control mass-dependent errors.

number of configurations	100
Volume	$10^3 \times 120$
a_s	0.21 fm
ξ	6
$a_t m_q$	-0.04 , 0.1, 0.2, 0.3, 0.4, 0.5, 1.0, 1.5

Table 4.1: Simulation parameters.

4.2.1 Simulation details

The parameter values used in this study are summarised in Table 1.

A very fine temporal lattice spacing, $a_t \sim 0.04$, was used in this study so that errors were expected to be very small. Therefore, the chromoelectric term in the fermion action, which effects $\mathcal{O}(a_t)$ improvement, was omitted. For consistency, the coefficient μ_r, which multiplies the kinetic terms in the fermion action, was set to one. In this case, the quark action does not include field rotations.

A hundred gauge configurations had already been tuned to $\xi = 6$. The actual value of the target anisotropy is not particularly relevant to the tuning procedure and we can reformulate the problem in terms of another physical observable, $c = \xi_q^R \xi^{-1}$, which we call the speed of light. The bare anisotropy, ξ_q, is tuned so that the speed of light takes its continuum value of unity. The tuning procedure therefore amounts to a restoration of Euclidean invariance.

A broad range of quark masses was used. Bare mass values ranged from $a_t m_q = -0.04$ to $a_t m_q = 1.5$ in this study. Since our fermion action breaks chiral symmetry, quarks are subject to an additive mass renormalisation. Therefore, the lightest bare mass used in this study actually corresponds to a positive renormalised quark mass. Physically, this was found to be close to the strange quark mass. At the other end of the spectrum, the heaviest quarks used were found to lie above the b-quark.

Dispersion relations were computed for pseudoscalar ($J^{PC} = 0^{-+}$) and vector (1^{--}) mesons containing degenerate and non-degenerate quark combinations. The

interpolating operators used were

$$\mathcal{O}^{PS} = \bar{\psi}\gamma_5\psi, \ \mathcal{O}_i^V = \bar{\psi}\gamma_i\psi. \tag{4.5}$$

To enhance the vector signal, contributions to the correlator from the three spatial directions were averaged. In the case of non-degenerate quark combinations, one quark mass was fixed at $a_t m_q = -0.04$. Meson energies were computed for momenta $2\pi\mathbf{n}/a_s N_s$, where N_s is the number of lattice sites in the spatial directions, at $\mathbf{n} = (0,0,0)$, $(1,0,0)$, $(1,1,0)$ and $(1,1,1)$, averaging over equivalent directions.

4.2.2 Computing meson energies

A relativistic meson can propagate backwards in time and on a lattice of finite temporal extent T and (anti-)periodic boundary conditions, the two point correlator is given by

$$C(t,\mathbf{p}) = \sum_n C_n \left(e^{-E_n t} + e^{-E_n(T-t)}\right). \tag{4.6}$$

This correlator is symmetric about $t = T/2$ and the signal was enhanced by averaging $C(t,\mathbf{p})$ about this point. The correlator signal was further improved by averaging over four sources at timeslices 0, 30, 60 and 90.

The ground state can be determined from a fit to the correlator in the time interval

$$\frac{1}{E_0 - E_1} \ll t < \frac{T}{2}, \tag{4.7}$$

where E_1 is the energy of the first excited state of the meson. In this range

$$C(t,\mathbf{p}) \approx C_0 \left(e^{-E_0 t} + e^{-E_0(T-t)}\right), \tag{4.8}$$

and ground state energies were determined by fitting to this form.

The fits were done using a χ^2 minimisation algorithm which takes correlations

in the data into account. The statistical error in each fit was determined from 1000 bootstrap samples of the gauge ensemble.

Because of the improved resolution in the temporal direction provided by the anisotropic lattice, meson energies could be determined to a high precision. Although reasonable fit ranges could easily be found by simply looking at the effective mass

$$a_t M_{\text{eff}}(t) = \cosh^{-1}\left(\frac{C(t+1,\mathbf{p}) + C(t-1,\mathbf{p})}{C(t,\mathbf{p})}\right), \tag{4.9}$$

a more sophisticated, partially-automated approach was used to determine the optimal fit ranges. In this approach, the minimum and maximum timeslices of the fit were varied independently of each other. A fit was performed on each range and the results were plotted in histogram format; the fit values together with error estimates were plotted on one axis and the goodness of the fit on the other. Invariably, a number of overlapping ranges yielded good fits which were consistent with each other within errors. Of these, the optimal fit was that which included most timeslices. The quality of the fits were finally confirmed by eye.

Figure 4-1 shows effective mass plots for the pseudoscalar mesons containing degenerate quarks. The upper plot shows effective masses for the lightest quark mass for zero momentum and $\mathbf{n} = (1,1,1)$. The corresponding plot for $a_t m_q = 1.0$ is shown in the lower figure. Effective mass plots for the non-degenerate quark combinations were equally good and fits to the pseudoscalar correlator included 10 or more timeslices. Analogous plots for the vector meson are shown in Fig. 4-2.

4.2.3 Computing the dispersion relation

For a given meson, ground-state energies were computed over the range of spatial momenta. The quantity $(a_t E(\mathbf{p}))^2$ was plotted against $(a_s \mathbf{p})^2$, and the speed of light, which we denote c, was determined from a fit to the continuum form $E^2(\mathbf{p}) = E^2(\mathbf{0}) + c^2\mathbf{p}^2$. For the momenta considered and over the full range of quark masses there were no significant deviations from this form. Fits were performed using the

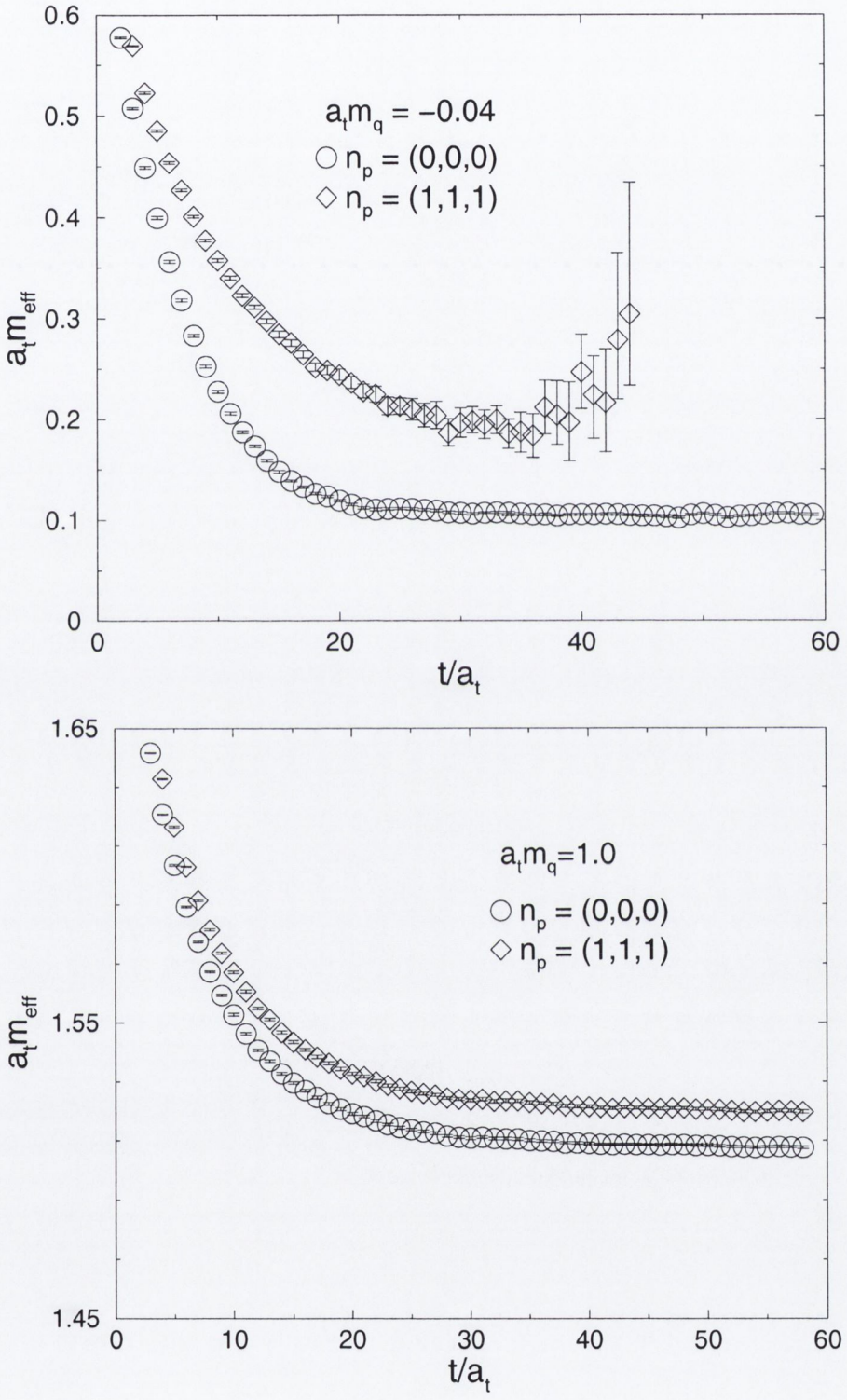

Figure 4-1: Pseudoscalar meson effective mass plots. These illustrate the good fits which are possible for a wide range of quark masses and meson momenta. Physically $a_t m_q = -0.04$ corresponds to the strange quark mass while $a_t m_q = 1.0$ is approximately equal to the b-quark mass.

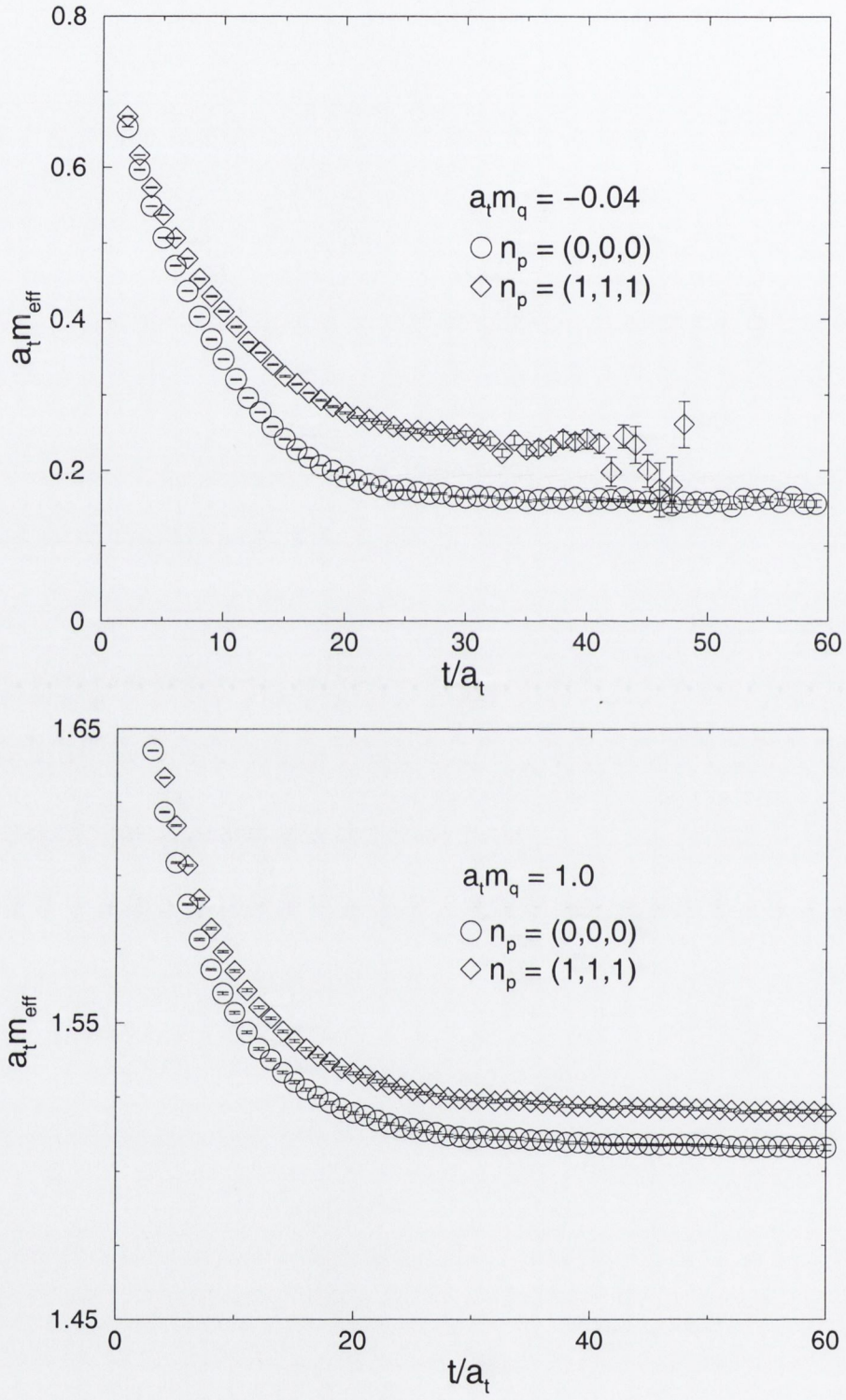

Figure 4-2: Vector meson effective mass plots. These show the same qualitative behaviour as the pseudoscalar effective mass plots.

χ^2 minimisation algorithm and the error on c was determined using the bootstrap algorithm.

4.2.4 Tuning the quark anisotropy

Initially, the input anisotropy was chosen to be $\xi_q = 6$ and c was determined from the pseudoscalar meson containing degenerate quarks with mass $a_t m_q = -0.04$.

The exact relation between the bare anisotropy and the measured anisotropy is a complicated function of the lattice parameters, which can be written

$$\xi_q^R = Z_\xi(g, m_q, \xi, \xi_q)\xi_q, \tag{4.10}$$

where

$$Z_\xi(0, 0, \xi, \xi_q) = 1. \tag{4.11}$$

To tune the anisotropy, we considered the effect of a small change in the bare anisotropy $\xi_q \to \xi_q + \delta\xi_q$, keeping the other parameters fixed. The corresponding change in Z_ξ is

$$Z_\xi(g, m_q, \xi, \xi_q + \delta\xi_q) = Z_\xi(g, m_q, \xi, \xi_q) + \mathcal{O}(g^2\delta\xi_q). \tag{4.12}$$

For sufficiently small $\delta\xi_q$, the change in Z_ξ is expected to be negligible so that the renormalised anisotropy varies in proportion to ξ_q. This naive argument suggests that we 'boost' the bare anisotropy, making the replacement

$$\xi_q \to \frac{\xi_q}{c}. \tag{4.13}$$

Therefore, quark propagators were regenerated using the new input anisotropy $\xi_q = 6.17$ and the energy-momentum relation for the pseudoscalar meson was recomputed. The value of c determined from this tuned data was 1.02 ± 0.01. This result seemed

to indicate that the anisotropy could be tuned to high-precision non-perturbatively. To check this, c was then measured from the vector dispersion relation. The result, $c = 0.97(2)$, is consistent with unity to within 1 sigma.

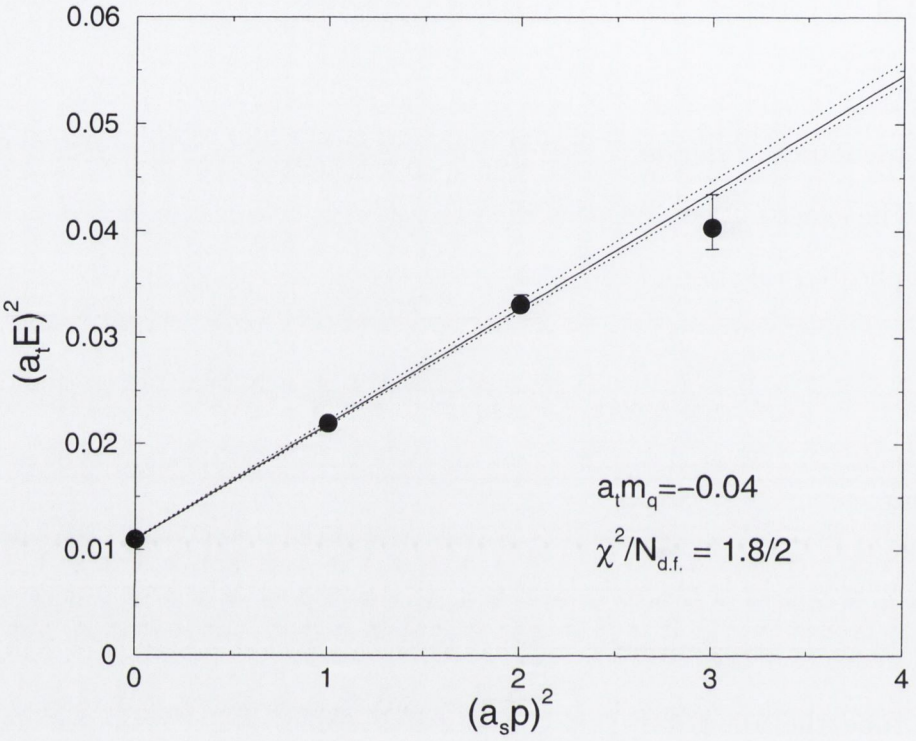

Figure 4-3: Dispersion relation for the lightest degenerate meson. For the range of momenta considered the plot shows no significant deviation from the continuum form $E^2 = M^2 + c^2\mathbf{p}^2$. The fit yields $c = 1.02 \pm 0.01$

Mass dependence of the anisotropy.

The reader will have noticed a slight discrepancy between the tree-level definition of the bare anisotropy $\xi = \xi_q$ and the non-perturbative determination. Since the quark action has $\mathcal{O}(a_t)$ discretisation errors, we expect mass-dependent corrections to the relativistic dispersion relation even at the tree level. Even in the isotropic formalism, c is modified by mass-dependent corrections so that a hadron's rest mass, $E(\mathbf{0})$, is not generally equal to its kinetic mass, $(\partial^2 E(\mathbf{0})/\partial p^2)^{-1}$. However, the premise for using the anisotropic quark action is that, as long as $a_t m_q \ll 1$, mass-dependent errors are negligible. This implies that a single determination of the action parameters should

hold over a range of masses. To test this, ξ_q was fixed at 6.17 and c was computed for a range of quark masses. Tables 4.2 and 4.3 show the speed of light determined from the dispersion relations for each quark mass for both pseudoscalar and vector mesons.

	Pseudoscalar			Vector		
$a_t m_q$	$a_t M_{PS}$	c	χ^2/N_{df}	$a_t M_V$	c	χ^2/N_{df}
-0.04	0.1045^{+5}_{-5}	1.02^{+1}_{-1}	6.3/2	0.161^{+2}_{-2}	0.97^{+2}_{-2}	0.66/2
0.10	0.3831^{+4}_{-4}	0.983^{+6}_{-7}	2.8/2	0.3934^{+4}_{-4}	0.982^{+8}_{-8}	2.1/2
0.20	0.5418^{+3}_{-4}	0.995^{+7}_{-7}	0.33/2	0.5472^{+4}_{-4}	0.990^{+8}_{-8}	2.1/2
0.30	0.6887^{+4}_{-4}	1.010^{+8}_{-7}	2.4/2	0.6924^{+4}_{-4}	0.997^{+9}_{-9}	4.5/2
0.40	0.8269^{+4}_{-4}	1.022^{+5}_{-5}	0.65/2	0.8294^{+4}_{-4}	1.011^{+5}_{-5}	2.3/2
0.50	0.9569^{+4}_{-4}	1.035^{+5}_{-5}	1.3/2	0.9587^{+4}_{-4}	1.025^{+5}_{-5}	1.6/2
1.00	1.5086^{+3}_{-3}	1.069^{+5}_{-5}	1.3/2	1.5092^{+3}_{-3}	1.072^{+5}_{-5}	1.2/2
1.50	1.9428^{+3}_{-3}	1.075^{+5}_{-5}	0.081/2	1.9431^{+3}_{-4}	1.072^{+5}_{-5}	0.058/2

Table 4.2: Ground state rest masses for pseudoscalar and vector mesons with degenerate quarks. The speed of light determined from the dispersion relation for each quark mass is shown with the corresponding χ^2/N_{df}. The errors shown are statistical only.

	Pseudoscalar			Vector		
$a_t m_q$	$a_t M_{PS}$	c	χ^2/N_{df}	$a_t M_V$	c	χ^2/N_{df}
0.1	0.2610^{+6}_{-6}	0.98^{+1}_{-1}	0.23/2	0.2802^{+8}_{-8}	0.98^{+2}_{-2}	0.19/2
0.2	0.3466^{+6}_{-6}	1.01^{+2}_{-2}	0.56/2	0.3601^{+8}_{-8}	0.99^{+2}_{-2}	0.64/2
0.3	0.4254^{+7}_{-7}	1.02^{+2}_{-2}	2/2	0.4351^{+8}_{-8}	1.00^{+2}_{-2}	0.45/2
0.4	0.4987^{+7}_{-7}	1.01^{+2}_{-2}	1.5/2	0.5056^{+8}_{-9}	0.99^{+2}_{-2}	1.4/2
0.5	0.5668^{+8}_{-8}	1.02^{+2}_{-2}	1.7/2	0.5720^{+9}_{-9}	1.00^{+2}_{-2}	1.6/2
1.0	0.8521^{+10}_{-10}	1.00^{+2}_{-2}	2.6/2	0.854^{+1}_{-1}	1.02^{+3}_{-3}	0.62/2
1.5	1.074^{+1}_{-1}	1.02^{+3}_{-3}	2.1/2	1.075^{+1}_{-1}	1.01^{+3}_{-4}	1.8/2

Table 4.3: Ground state rest masses for pseudoscalar and vector mesons with non-degenerate quarks. Other details are as for Table 2.

Of the mesons containing degenerate quarks, the lightest mass combinations were the noisiest. Non-degenerate combinations, which contain the lightest quark, were also noisier than their degenerate counterparts. This is not unexpected; on a given set of configurations, relative fluctuations in the low-lying eigenmodes of the fermion matrix, which are relevant to hadronic physics, increase with decreasing quark mass.

There was no significant difference between pseudoscalar and vector particles for a given quark combination at any mass. However, mesons containing degenerate quarks showed a stronger mass dependence than non-degenerate particles. This is illustrated in figures 4-4 and 4-5. In both cases, the x-axis plots the mass of the mesons containing degenerate quarks.

The stronger mass dependence of the degenerate quark combinations arises because -onium states containing heavy quarks are tightly bound with a small Bohr radius and are therefore more susceptible to discretisation effects.

For degenerate quark combinations, the change in c over the range of masses considered was $\approx 9\%$. In the case of the non-degenerate combinations the relative change was about 4%. However, the discrepancy between the two determinations only becomes significant for $a_t m_q \geq 0.5$. On this lattice, $a_t m_q = 0.2$ is close to the charm quark mass and the change in any determination of c over this range is at most 3%. This result confirms the feasibility of quenched charm simulations at this anisotropy.

In order to perform b-quark simulations on this lattice, we require $a_t m_q \approx 1$. In this range, the action couplings must be tuned in a mass-dependent way in order to regain continuum QCD. This is the Fermilab approach [26] which has proven successful in studies of the charmonium spectrum and b-physics. We therefore attempted to retune the anisotropy at $a_t m_q = 1.0$.

The dependence of the measured speed of light on the bare anisotropy for both pseudoscalar and vector mesons is shown in Fig. 4-6. Note the discrepancy between the value of c determined from degenerate and non-degenerate quark combinations for each value of the input anisotropy. The value of c determined from the -onium states moves closer to its target value of unity while c determined from the non-degenerate quark combinations moves away from this value. However, once again, values computed from pseudoscalar and vector mesons for a given quark combination are in agreement. Such an inconsistency was first reported in simulations performed with an isotropic clover action in Ref. [19]. The issue was resolved in Ref. [20] which

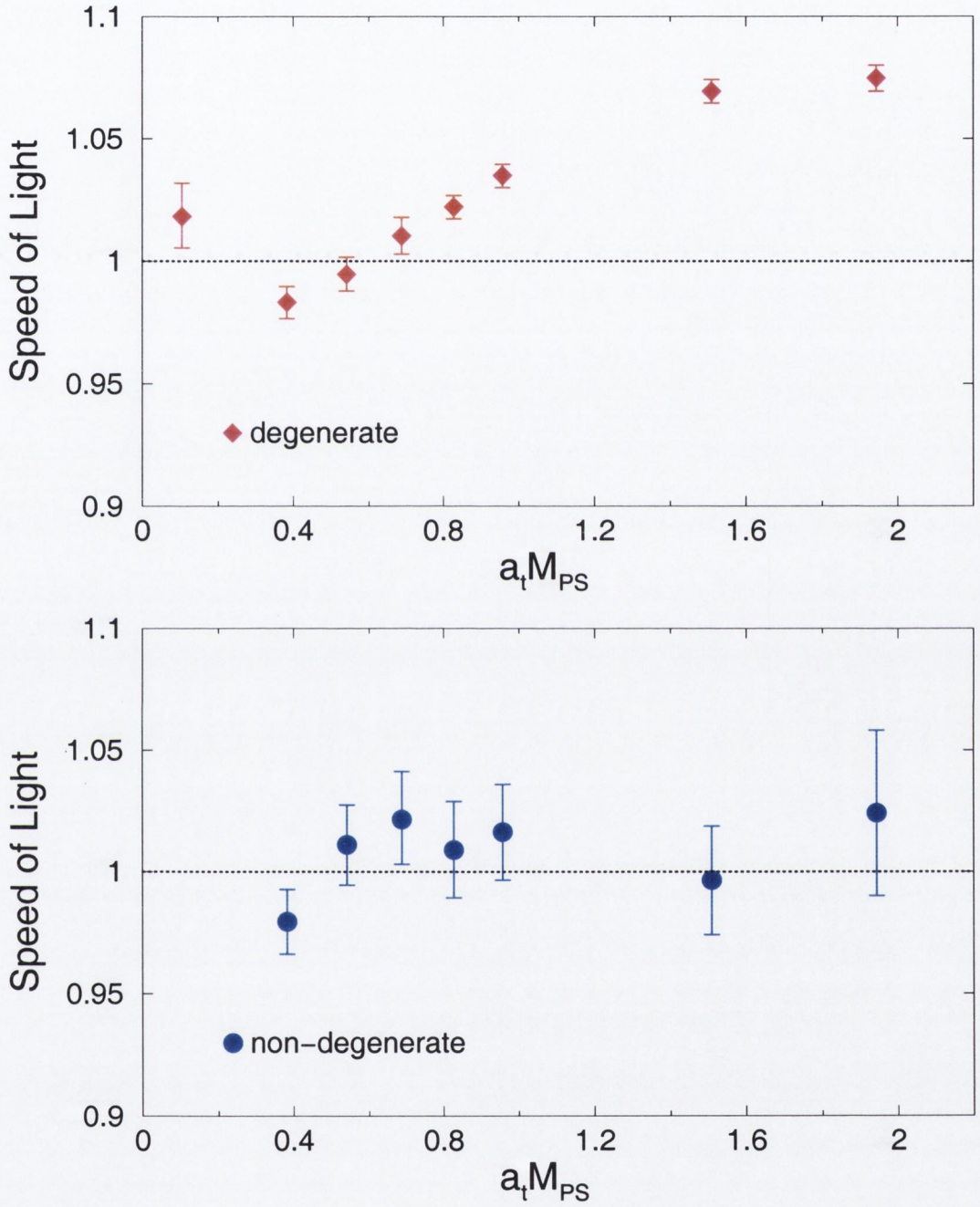

Figure 4-4: The mass-dependence of the speed of light determined from the pseudoscalar dispersion relations for $\xi_q = 6.17$. The plot shows mesons with degenerate and non-degenerate quark mass combinations. The x-axis plots the mass of the meson containing degenerate quarks.

demonstrated that the anomaly could be eliminated by including higher-order mass-dependent improvement terms in the quark action.

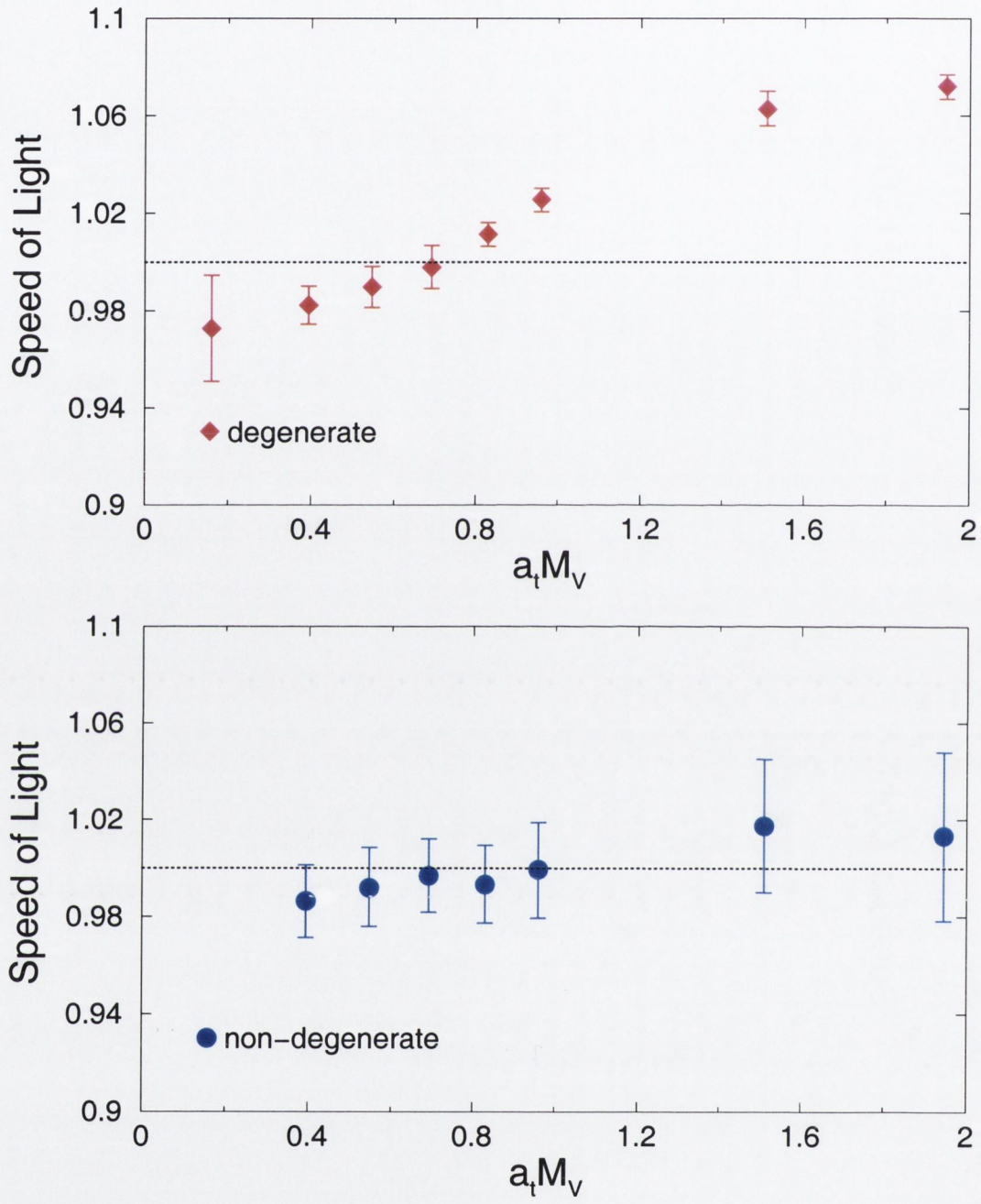

Figure 4-5: The mass-dependence of the speed of light determined from the vector dispersion relations with $\xi_q = 6.17$. Both degenerate and non-degenerate quark combinations are shown.

4.3 Conclusions

In this chapter, we described the non-perturbative tuning of the quark and gauge anisotropies. We considered the quenched approximation where this difficult task

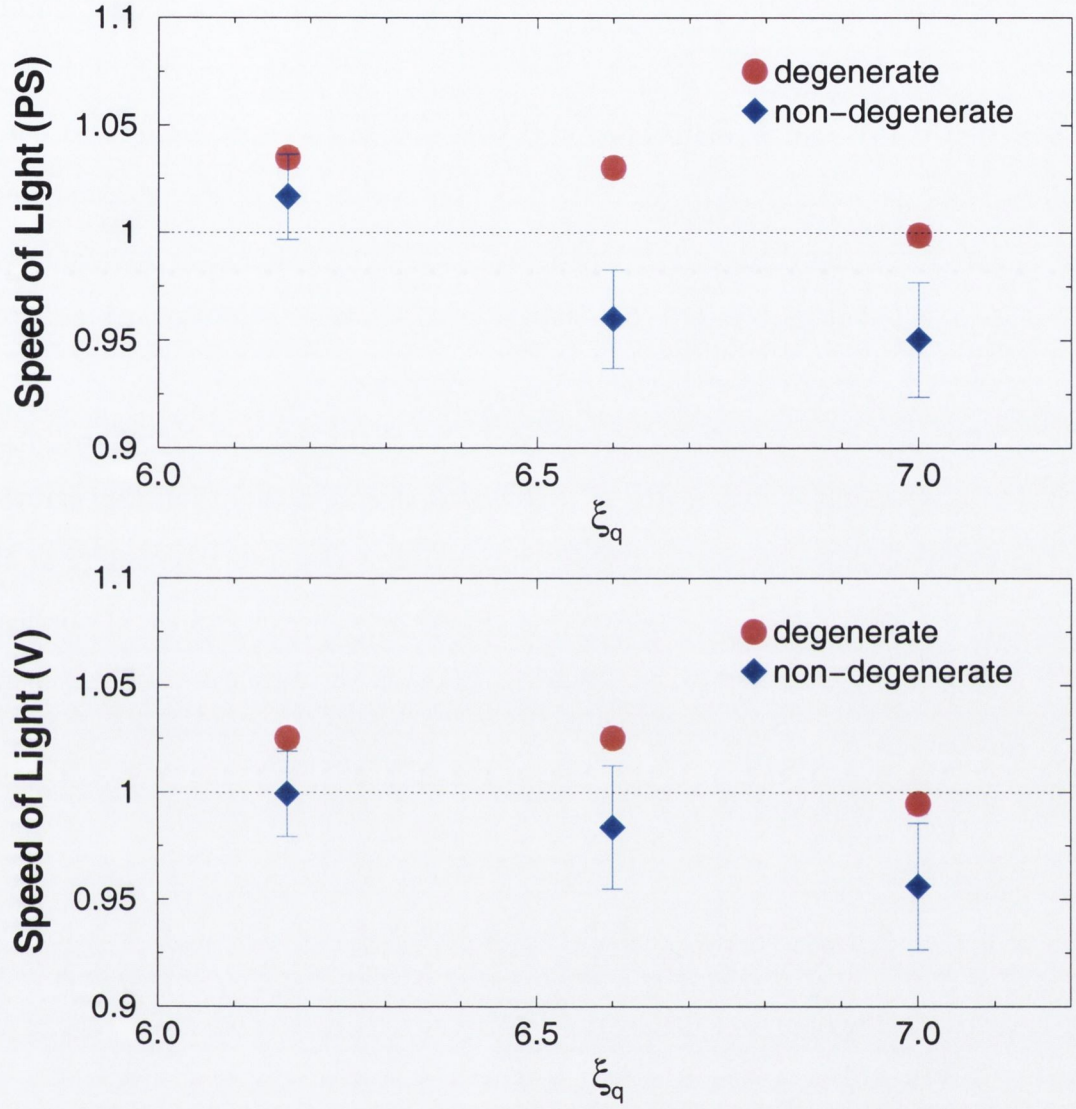

Figure 4-6: The speed of light measured from pseudoscalar (PS) and vector (V) dispersion relations as a function of the bare anisotropy, ξ_q. In both plots the quark mass is fixed at $a_t m_q = 1.0$, which is expected to lie outside the range of applicability of the anisotropic lattice. In spite of this, discrepancies between degenerate and non-degenerate quark combinations are only of the order of a few percent.

factorises into two simpler problems.

The tuning of the anisotropy in the pure Yang-Mills sector was outlined; however, we focused on the non-perturbative determination of the quark anisotropy parameter. This was done by demanding that meson dispersion relations have the correct relativistic form at small momenta. The improved resolution offered by the anisotropic lattice allowed us to compute dispersion relations to a high precision.

On the anisotropic lattice, provided $a_t m_q \ll 1$, mass-dependent cutoff effects should be heavily suppressed. We found that a single determination of the anisotropy at the lightest quark mass $a_t m_q = -0.04$ held up to $a_t m_q \approx 0.5$, so that lattice artifacts were small even for $a_s m_q > 1$. Over this range, pseudoscalar and vector mesons containing both degenerate and non-degenerate quark combinations yield consistent results. These results indicated that relativistic charm quarks could be accurately simulated on this lattice.

We then considered a mass-dependent tuning of the anisotropy at $a_t m_q = 1$. In this case, we found inconsistencies between degenerate and non-degenerate mesons and further improvement of the fermion action is required to simulate at these parameter values. However, $a_t m_q = 1$ is outside the intended range of applicability of the anisotropic action and it should be possible to simulate b-physics using larger anisotropies.

Chapter 5

A perturbative investigation of the fermion action

In this section, we turn our attention to an analytic investigation of the fermion action using weak-coupling perturbation theory. First, we review the properties of the fermion action at the tree-level. Then, we detail our determination of corrections to the speed of light, measured from the lattice quark dispersion relation, at the one-loop order. This quark action has already been investigated at one-loop in perturbation theory in Ref. [28]. That study was performed in the limit of continuous time, $a_t \to 0$, $\xi \to \infty$, where undesirable $\mathcal{O}(a_s m_q)$ errors are manifest. The authors found that the one-loop correction to the speed of light was almost linear in $a_s m_q$. They were unable, however, to make any quantitive prediction for the magnitude of this correction or to examine the functional dependence of the correction on the bare anisotropy. With our work, we aimed to address these issues.

Furthermore, having performed a numerical investigation of the quark action, we were in a position to assess the validity of one-loop perturbation theory on spatially coarse but temporally fine asymmetric lattices. This is perhaps the most important point because our ability to make reliable physical predictions using anisotropic lattices depends on the accuracy of perturbative matching calculations.

We present results for the renormalisation of the quark rest mass. We also com-

pute the mass and anisotropy dependence of the speed of light renormalisation and compare with the results of our numerical investigation.

5.1 Lattice perturbation theory

The trouble with lattice perturbation theory

Lattice perturbation theory (LPT) is extremely complicated. Although the lattice does provide an ultra-violet cutoff, it is not Euclidean invariant. Loop integrands on the lattice are complicated trigonometric functions of momentum and integrals can only be evaluated numerically. Also, as we mentioned earlier, because the gauge sector of the lattice theory is formulated in terms of link variables, there are an infinite number of interaction vertices which have no continuum counterparts but which have a significant effect on the physics at finite lattice spacing. Add to this the fact that each lattice action defines a different regularisation with different Feynman rules and it is easy to understand why, until recently, progress in LPT has been slow, with few calculations beyond the one-loop order.

Automating Perturbation Theory

To circumvent the difficulties outlined above, a number of groups [23, 24] have invested considerable effort in automating perturbative calculations, substituting numerical power for complicated manipulations of lattice integrands. Their software is not optimised for a particular lattice discretisation but is designed to be action independent. Therefore, once a suite of code to compute a particular quantity has been written, the calculation may be repeated for a range of lattice actions. The manipulation of loop integrands by hand can be a considerable source of error in perturbative calculations. By automating this procedure the opportunities for error are considerably reduced, allowing for increasingly ambitious calculations involving a large number of Feynman diagrams and sophisticated actions.

Actually, much of the framework for a fully automated approach has been in place for some time. In their seminal 1986 paper, Lüscher and Weisz proposed an algorithm for automatically generating interaction vertices in the pure gauge theory. Lepage's numerical integrator, VEGAS [25], which is commonly used to evaluate loop integrals has existed for even longer. However, only recently, have computers become sufficiently powerful that a numerical brute-force approach to LPT can yield accurate results in a range of calculations.

Later, we will describe how we incorporated some of this automated framework into our study, thereby paving the way for more advanced perturbative investigations.

5.2 Lattice Feynman rules

In order to perform perturbative calculations, it is necessary to define a generating functional for the lattice Feynman rules. We cannot simply add source terms to the lattice partition function given in Eq. 2.18 as it stands. There are two reasons for this: firstly, it is necessary to fix a gauge. Although gauge-fixing is not required in numerical calculations of physical observables, the perturbative expansion is ill-defined unless a gauge is fixed. Secondly, one needs to consider contributions from the path integral measure. Since the perturbative expansion is in powers of the coupling g_0 and hence the gauge fields A_μ, we must reformulate the measure in terms of the gauge fields themselves.

Gauge fixing

Weak-coupling perturbation theory involves an expansion about a classical minimum of the gauge action. This minimum is degenerate with respect to gauge transformations and a gauge must be fixed to remove this degeneracy. A general gauge fixing condition suitable for the lattice theory is

$$\partial^L_\mu A^a_\mu(x) = \chi^a(x), \;\; a = 1, \ldots, 8, \tag{5.1}$$

where ∂_μ^L, is the left lattice derivative and χ^a is an arbitrary scalar field. Fadeev and Popov proposed an elegant way of implementing the gauge-fixing condition which preserves the path integral measure. This is done by inserting the following expression for the identity into the path integral

$$1 = \triangle_{FP}[U;\chi] \int Dg\ \delta(\partial_\mu^L A_\mu^g - \chi), \tag{5.2}$$

where g denotes a gauge transformation, A_μ^g being the gauge transform of A_μ, and $\triangle_{FP}$ is the Fadeev-Popov determinant. Because it is defined in terms of an integral over the gauge group manifold, the determinant is gauge invariant. Therefore, in the expectation value of a gauge invariant operator, the integral over the group manifold in Eq. 5.2 factors out, leaving

$$\langle \mathcal{O}(\bar{\psi},\psi,U)\rangle = \frac{1}{Z}\int DU D\bar{\psi} D\psi\ \mathcal{O}(\bar{\psi},\psi,U)\ \triangle_{FP}[U;\chi] \prod_x \delta(\partial_\mu^L A - \chi) e^{-S_{\text{latt}}}. \tag{5.3}$$

The Fadeev-Popov determinant can be rewritten as an integral over Grassman-valued ghost fields. The expectation value in Eq. 5.3 must not depend on a particular choice of the fields χ^a and the delta function can be eliminated by averaging over χ^a with a Gaussian weighting factor. The gauge-fixed expectation value is then given by

$$\langle \mathcal{O}(\bar{\psi},\psi,U)\rangle = \frac{1}{Z}\int DU D\bar{\psi} D\psi D\bar{c} Dc\ \mathcal{O}(\bar{\psi},\psi,U) e^{-S_{\text{eff}}}, \tag{5.4}$$

where $S_{\text{eff}} = S_{\text{latt}} + S_{FP} + S_{GF}$. The Fadeev-Popov part of the effective action is

$$S_{FP} = \sum_x \bar{c}^a(x) D_\mu^{ab}(A) c^b(x) \tag{5.5}$$

where $\bar{c}, c$ are the spinless but colourful ghost fields and D_μ is a discretisation of the covariant derivative in the adjoint representation of $SU(3)$. The gauge-fixing term is

$$S_{GF} = \sum_x \frac{1}{2\alpha}(\partial_\mu^L A_\mu^a)^2 = -\sum_x \frac{1}{2\alpha} A_\mu^a \partial_\mu^R \partial_\nu^L A_\nu^a, \tag{5.6}$$

where α is the Gaussian weighting factor.

The integration measure

While gauge-fixing is also a feature of continuum perturbation theory, the contribution of the path-integral measure to Feynman diagrams is purely a lattice artifact. The gauge-invariant measure can be written

$$DU = e^{-S_{\text{meas}}} DA, \tag{5.7}$$

where $DA = \prod_{xa\mu} dA^a_\mu(x)$. The explicit form of S_{meas} appearing in the Jacobian is not required for our calculations and we note only that, as expected, it contributes an infinite number of gluon vertices to the lattice Feynman rules and the lowest-order vertex is $\mathcal{O}({g_0}^2)$.

The Lattice Generating Functional

Drawing on our previous discussions, we find an expression for the lattice generating functional including source terms

$$\begin{aligned} Z[J,\eta,\bar{\eta},\xi,\bar{\xi}] &= \int DAD\bar{\psi}D\psi D\bar{c}Dc \exp\left(-S_{\text{tot}} + \sum_x J_\mu A_\mu + \bar{\eta}\psi + \bar{\psi}\eta + \bar{\xi}c + \bar{c}\xi\right), \\ Z[J,\eta,\bar{\eta},\xi,\bar{\xi}] &= \int DAD\bar{\psi}D\psi D\bar{c}Dc \exp\left(-S_{\text{tot}} + \sum_x J_\mu A_\mu + \bar{\eta}\psi + \bar{\psi}\eta + \bar{\xi}c + \bar{c}\xi\right), \end{aligned} \tag{5.8}$$

which contains the total action

$$S_{\text{tot}} = S_{\text{eff}} + S_{\text{meas}}. \tag{5.9}$$

Momentum-space vertices

Our calculations were performed in momentum space and, here, we define the Fourier transforms of the lattice variables. These are

$$\begin{aligned} \psi(x) &= \int_p e^{ipx}\tilde{\psi}(p), \\ \bar{\psi}(x) &= \int_p e^{-ipx}\tilde{\bar{\psi}}(p), \\ A_\mu(x) &= \int_k e^{ikx}\tilde{A}_\mu(k), \end{aligned} \tag{5.10}$$

with similar expressions for the Fadeev-Popov ghost fields. For brevity we have used the shorthand notation

$$\int_q \equiv \int_{-\frac{\pi}{a_\mu}}^{\frac{\pi}{a_\mu}} \frac{d^4q}{(2\pi)^4}, \tag{5.11}$$

where we assume a lattice of infinite extent so that the momentum is continuous. [1]

Our calculation required the free quark propagator and quark-gluon vertices which can be computed by Taylor expanding the fermion action and Fourier transforming into momentum space

$$\begin{aligned} S_q &= \sum_x \bar{\psi} M_q \psi, \\ &= \int_p \tilde{\bar{\psi}}(p) S_0^{-1}(p) \tilde{\psi}(p) \\ &\quad + \sum_{r=1}^{\infty} \frac{(ig_0)^r}{r!} \int_p \int_q \int_{k_1} .... \int_{k_r} \sum_{\mu_1,...\mu_r} \tilde{A}^{a_1}_{\mu_1}(k_1).....\tilde{A}^{a_r}_{\mu_r}(k_r) \\ &\quad \delta^4_{2\pi}\left(p - q + \sum_{i=1}^{r} k_i\right) \tilde{\bar{\psi}}(p) V_r(p, q; k_1, \mu_1, a_1; ....; k_r, \mu_r, a_r)\tilde{\psi}(q), \end{aligned} \tag{5.12}$$

where $S_0(p)$ is the free quark propagator and V_r denotes a vertex involving r glu-

[1] This is standard practice in many perturbative calculations. We will later consider perturbation theory on a lattice which is of finite extent along certain directions; we will then have to redefine the Fourier transforms to be consistent with the lattice boundary conditions.

ons. The subscript 2π on the delta functions indicates that momentum is conserved modulo $2\pi/a_\mu$.

We also need the gluon propagator, $D_{\mu\nu}$, which can be determined from that part of the action which is quadratic in the gauge fields only

$$S_{\text{tot}}^{Quad}(g_0 = 0) \; = \; \int_k \tilde{A}_\mu(k) D_{\mu\nu}^{-1}(k) \tilde{A}_\nu(k). \tag{5.13}$$

Therefore, the gauge-fixing term only enters into the perturbative calculation through the gluon propagator. Without this term, the matrix appearing in the integrand of Eq. 5.13 is singular and the free gluon propagator cannot be computed.

5.3 A tree-level investigation of the fermion action

In our study, we considered the momentum-space quark propagator $S(p)$ given by

$$a_t S^{-1}(p) = a_t S_0^{-1}(p) + a_t \Sigma(p), \tag{5.14}$$

where $\Sigma(p)$ is the quark self-energy,

$$\Sigma(p) = \sum_{n=1}^{\infty} g^{2n} \Sigma^{(n)}(p). \tag{5.15}$$

To begin with, we investigated the quark dispersion relation at the tree-level in perturbation theory. We first considered general values of the parameters r and s which appear in the action, given in Eq. 3.25.

The dispersion relation is obtained by solving for a pole in the free quark propagator. Equivalently, one can consider the free fermion matrix in momentum space, $\tilde{M}(p) \equiv S_0^{-1}(p)$. This is simply the Fourier transform of M_q in Eq. 3.25 with the link variables and tadpole improvement coefficients set to unity.

The energy-momentum relation is obtained by solving

$$\det \tilde{M} = 0 \tag{5.16}$$

for $E = -ip_0$. For a general value of r, this yields two relations

$$\cosh(a_t E_\pm) = \frac{r^2 + r\omega(p)}{r^2 - 1} \pm \frac{\sqrt{(r + \omega(p))^2 + (1 - r^2)(1 + a_t^2 \tilde{\mathbf{p}}^2)}}{r^2 - 1}, \tag{5.17}$$

where $\omega(p)$ and $\tilde{\mathbf{p}}$ are defined as

$$\omega(p) = a_t \mu_r m_0 + a_t s \sum_i a_s^3 \hat{p}_i^4, \tag{5.18}$$

$$\tilde{\mathbf{p}} = \mu_r \bar{p}_i (1 + \frac{1}{6} a_s^2 \hat{p}_i^2), \tag{5.19}$$

with $\bar{p}_i = \frac{1}{a_s} \sin(a_s p_i)$ and $\hat{p}_i = \frac{2}{a_s} \sin(a_s p_i / 2)$. As stated in Chapter 3, $\mu_r = \left(1 + \frac{1}{2} r a_t m_0\right)$ and m_0 is the bare quark mass. One of these relations describes an unphysical state; it is a remnant of temporal doubling which persists for $r \neq 1$ in the fermion action. Such states can occur because, for $r \neq 1$, the fermion matrix is not reflection positive and therefore does not have a positive-definite transfer operator connecting adjacent time-slices.

To identify the physical state, we set the spatial momentum and the bare quark mass to zero. In this limit, Eq. 5.17 becomes

$$\cosh(a_t E_-) = 1, \tag{5.20}$$

$$\cosh(a_t E_+) = \frac{r^2 + 1}{r^2 - 1}. \tag{5.21}$$

From this, we deduce that E_- is the energy of the physical state and note that in the limit $r \to 1$, the spurious state becomes infinitely massive, corresponding to the restoration of full reflection positivity.

Since we are interested in the infrared properties of the fermion action, we expand

the physical solution in powers of the spatial momentum about $\mathbf{p} = 0$ to give

$$E^2(\mathbf{p}) = M_1^2 + \frac{M_1}{M_2}\mathbf{p}^2 + \mathcal{O}(p^4). \tag{5.22}$$

The rest mass, M_1, and kinetic mass, M_2, were previously discussed in relation to relativistic hadrons. The quark rest mass is

$$M_1 = \frac{1}{a_t}\cosh^{-1}\left(\frac{r^2 + \mu_r m_0 r a_t - \sqrt{1 + 2\mu_r m_0 r a_t + m_0^2\mu_r^2 a_t^2}}{r^2 - 1}\right), \tag{5.23}$$

and the kinetic mass is given by

$$\frac{1}{M_2} = \frac{\mu_r^2 a_t}{\sqrt{1 + 2\mu_r m_0 r a_t + m_0^2\mu_r^2 a_t^2}}\left[\left(\frac{r^2 + \mu_r m_0 r a_t - \sqrt{1 + 2\mu_r m_0 r a_t + m_0^2\mu_r^2 a_t^2}}{r^2 - 1}\right)^2 - 1\right]. \tag{5.24}$$

These results show that, at the tree level, M_1 and M_2 and hence their ratio, i.e. the speed of light, do not depend on $\mathcal{O}(a_s m_q)$ terms or on the anisotropy, ξ.

All of our simulations were performed with $r = 1$, which simplifies the analysis considerably. For this particular choice of r, the dispersion relation is

$$4\sinh\left(\frac{E a_t}{2}\right) = \frac{a_t^2\tilde{\mathbf{p}}^2 + \omega^2(p)}{1 + \omega(p)}, \tag{5.25}$$

with

$$M_1 = \frac{1}{a_t}\ln(1 + \mu_r m_0 a_t), \tag{5.26}$$

$$\frac{1}{M_2} = \frac{2\mu_r}{m_0(2 + \mu_r m_0 a_t)}, \tag{5.27}$$

where now $\mu_r = (1 + \frac{1}{2}a_t m_0)$.

The free-quark dispersion relation for a massive quark is shown in Figure 5-1. In this figure, the anisotropy is $\xi_q = 6$, and $a_t m_0 = 0.2$ is the bare quark mass.

The dispersion relation is shown up to the edge of the lattice Brillouin zone. The parameter s in the quark action must take a positive value to remove spatial doublers. In our work, s was fixed at $1/8$ by requiring that the dispersion relation does not have a negative slope within the Brillouin zone.

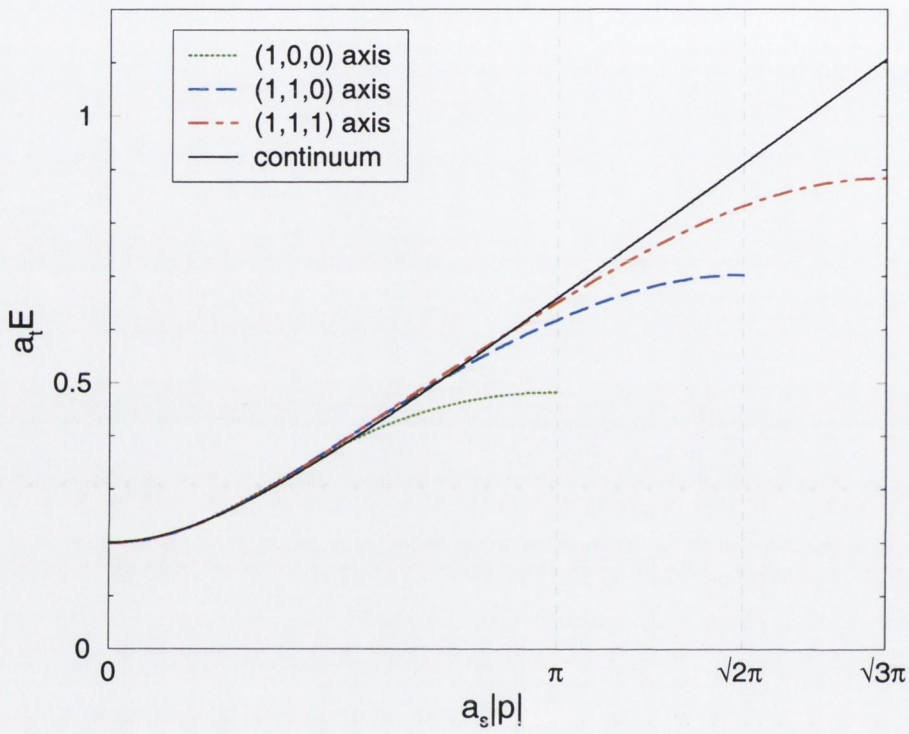

Figure 5-1: The dispersion relation with $\xi_q = 6$, $r = 1$ and $s = 1/8$. In this plot $a_t m_q = 0.2$. The dotted and dashed lines indicate quark momenta directed along different lattice axes. The line labelled 'continuum' is given by $E^2 = M_1^2 + \mathbf{p}^2$.

Figure 5-2 shows the deviation of this lattice dispersion relation from the continuum form for fixed $a_s m_q$ and varying anisotropy. Momentum is directed along a single spatial axis. As the anisotropy is increased, corrections to the relativistic behaviour are suppressed.

Mass-dependent tuning of the fermion action

In analogy to the previous chapter, the parameters of the fermion action can be tuned by demanding a relativistic dispersion relation for lattice quarks in the infrared regime, i.e. by requiring that $M_1 = M_2$. This mass-dependent improvement condition

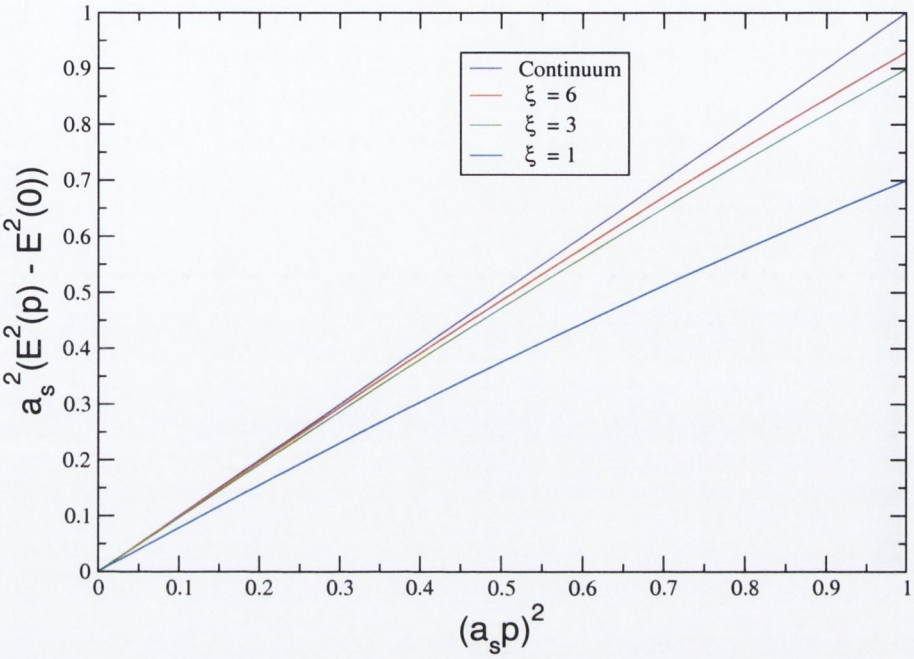

Figure 5-2: Deviation of lattice dispersion relations from the continuum form for $a_s\mathbf{p} < 1$ and $a_s m_q = 1.0$. As in the previous plot, $r = 1$ and $s = 1/8$. The figure clearly shows that at the tree-level mass-dependent corrections are suppressed on the anisotropic lattice.

was first suggested in Ref. [26].

To simplify improvement, we first redefine the bare quark mass

$$\mu_r m_0 \rightarrow m_0. \tag{5.28}$$

Tuning the action parameters to satisfy the improvement condition then amounts to a redefinition of μ_r,

$$\mu_r^{(0)} = \sqrt{\frac{a_t m_0(2 + a_t m_0)}{2\ln(1 + a_t m_0)}}, \tag{5.29}$$

which leaves the action unchanged at $\mathcal{O}(a_t)$ and is therefore consistent with the field rotations used to construct the original quark action. Although this implementation may seem at odds with our previous study, where corrections to the relativistic dispersion relation were absorbed into a redefinition of the bare anisotropy, it is the ratio μ_r/ξ_q which must be tuned to restore Euclidean invariance. Choosing to rede-

fine μ_r emphasises the point made earlier: that mass-dependent corrections to the relativistic dispersion relation are not specific to anisotropic lattices. At non-zero quark mass, the speed of light is modified even in the isotropic formalism, and at the tree-level corrections to μ_r are independent of ξ.

5.4 A 1-loop calculation of the quark rest mass and speed of light parameter

To proceed beyond the tree-level, we must compute the contributions of the quark self energy to the fermion propagator. On the lattice, the dimensionless quark self-energy has the following form

$$a_t\Sigma(p) = i\gamma_\mu \mathcal{A}_\mu(p)\sin(a_\mu p_\mu) + \mathcal{C}(p). \tag{5.30}$$

As was pointed out by Mertens et al. [27], in a Euclidean-invariant regularisation $\mathcal{A}_\mu$ must be independent of the direction μ, and $\mathcal{A}_\mu$ and $\mathcal{C}$ are functions of p^2. On the lattice, the constraints on the form of the self-energy are less strict. However, parity and time-reversal symmetry still require that $\mathcal{A}_\mu$ and $\mathcal{C}$ be even functions of the four-momentum, and invariance under spatial rotations means that, for example, $\mathcal{A}_1(0,p,0,0) = \mathcal{A}_2(0,0,p,0)$. The explicit form of the free-fermion propagator is given in Appendix A. Here, we need only note that the free propagator must have the same general form as the self energy, i.e.

$$a_t S^{-1}(p) = i\gamma_\mu \mathcal{P}_\mu(p)\sin(a_\mu p_\mu) + \mathcal{M}(p), \tag{5.31}$$

and that the simple symmetric discretisation of the temporal derivative in this quark action gives $\mathcal{P}_0 = 1$. For Wilson-like quarks with $r = 1$, solving for the pole in the

fermion propagator and setting $p_0 = iE$ yields

$$1 + \omega(p) - \cosh(a_t E) - C = \sqrt{(1 - \mathcal{A}_0)^2 \sinh^2(a_t E) + \sum_i (\mathcal{P}_i^2 - \mathcal{A}_i^2) \sin^2(a_s p_i)}, \tag{5.32}$$

where

$$\mathcal{M}(p, m) = 1 - \cos(a_t p_0) + \omega(p). \tag{5.33}$$

Setting $\mathbf{p} = 0$ yields an expression for the quark rest mass, M_1,

$$1 + a_t m_0 - \mathcal{C} - \cosh(a_t M_1) = (1 - \mathcal{A}_0) \sinh(a_t M_1). \tag{5.34}$$

Differentiating Eq. 5.32 twice with respect to p_i and imposing the mass-shell condition $p = (iM_1, \mathbf{0})$, fixes the kinetic mass in terms of M_1 and the parameters of the action. For ARIA, we find

$$\begin{aligned} \frac{e^{a_t M_1} - \mathcal{A}_0(iM_1, \mathbf{0}) \cosh(a_t M_1)}{\xi^2 a_t M_2} &= \frac{[\mu_r/\xi_q - A_1(iM_1, \mathbf{0})]^2}{[1 - A_0(iM_1, \mathbf{0})] \sinh(a_t M_1)} \\ &+ \frac{d^2}{d(a_s p_i)^2} [\mathcal{A}_0(iM_1, \mathbf{0}) \sinh(a_t M_1) - C(iM_1, \mathbf{0})]. \end{aligned} \tag{5.35}$$

These relations were first derived for isotropic lattices in Ref. [27] and generalised to anisotropic lattices in Ref. [28]. They are valid at all orders in perturbation theory. The precise relationship between M_1, M_2 and the parameters of the action can be be determined to any loop-order by expanding these expressions in powers of the gauge coupling. In particular, Eq. 5.35 allows us to compute corrections to the quark dispersion relation. Note that, in this expression, we have maintained the distinction between the action parameter ξ_q, and the physical ratio of scales ξ. At the tree-level, setting $\xi_q = \xi$ and imposing the relativistic constraint, $M_1 = M_2$, leads back to the

expression for $\mu_r^{(0)}$ in Eq. 5.29. Also, it is clear that higher-order radiative corrections can be absorbed into a redefinition of μ_r.

Evaluating the self-energy

The remainder of our calculation reduces to a determination of the quark self-energy and its derivatives with respect to external momentum at one-loop in perturbation theory.

The following Feynman diagrams contribute to the one-loop quark self-energy,

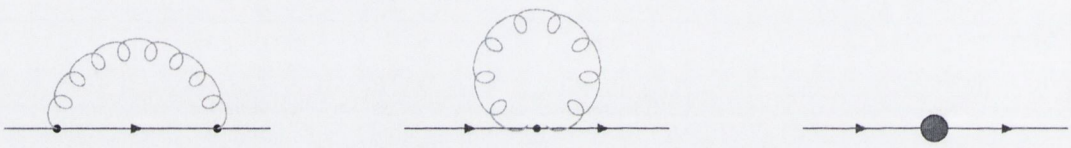

1-loop contributions to the quark self-energy.

Only the first graph, the rainbow diagram, exists in the continuum. The second diagram is a tadpole contribution and the third diagram is a counter-term coming from mean-field improvement. In order to evaluate these integrals, expressions for the free quark and gluon propagators, the 1-gluon–2-quark and the 2-gluon–2-quark vertices are needed. These were initially calculated by hand and the results were verified by repeating the calculation with Mathematica.

With the Wilson gauge action and the gauge-fixing term in Eq. 5.6, the choice $\alpha = 1$, i.e. Feynman gauge, yields a propagator which is proportional to the identity:

$$D_{\mu\nu}^{\alpha=1}(k) = \frac{\delta_{\mu\nu}}{\hat{k}^2}, \quad \hat{k}_\mu = \frac{2}{a_\mu} \sin\left(\frac{a_\mu k_\mu}{2}\right). \tag{5.36}$$

This simplifies perturbative calculations considerably and many calculations involving Wilson glue are performed in Feynman gauge only. However, the Symanzik-improved gluon propagator is much more complicated and this simplification no longer arises. We therefore calculated the gluon propagator for a general value of α and were able to check that physical results were invariant under a change of gauge.

In practice, loop integrands were constructed from dimensionless vertices, which were obtained by multiplying their dimensionful counterparts by powers of the temporal lattice spacing, a_t. Integrals were reformulated in terms of dimensionless loop momentum $k_\mu^{'} = a_\mu k_\mu$; so that, for example, the rainbow contribution to the self-energy is

$$a_t \Sigma_R^{(1)}(p) = \frac{1}{\xi^3} \int_{-\pi}^{\pi} \frac{d^4 k^{'}}{(2\pi)^4} \mathrm{Tr} \left[V_1(p^{'} - k^{'}, p; k^{'}, \mu) \hat{S}_0(p^{'} - k^{'}) V_1(p^{'}, p^{'} - k^{'}; -k^{'}, \nu) \hat{D}_{\mu\nu}(k^{'}) \right], \tag{5.37}$$

where the trace is over colour matrices and the hat symbols on the quark and gluon propagators indicate that they are dimensionless. Note that the limits of integration contain no reference to the anisotropy.

Implementation in software

In the early stages of this project, the loop integrands were evaluated explicitly using Mathematica. This involved tying the vertices and propagators together, performing the spinor algebra to project out the required components of the self-energy, differentiating with respect to external momenta where necessary, and setting the integrand on the mass shell. We then used symmetries of the self-energy to eliminate redundant terms in the integrands. The resulting expressions were written as functions in C which served as input for numerical integration packages.

However, these expressions were very unwieldy and difficult to check, even for this one-loop calculation. Furthermore, any variation of this calculation would require the generation of new expressions. It quickly became clear that our time would be better spent automating the evaluation of the lattice integrands. To that end, we wrote a suite of code in C++, which can take vertices derived from arbitrary lattice actions, contract the Lorentz indices, manipulate the spin matrices and compute derivatives

as required.

Our approach is based on that in Refs. [33] and [34] and incorporates the following features:

In a numerical evaluation of the loop integrals, traces over the relevant spin matrices are evaluated at the outset. Indices labeling the required vertex components along with the corresponding trace values are saved and do not have to be recomputed each time the integrand function is called in the integration package.

For given four-momenta, derivatives of the integrand are evaluated using automatic differentiation [36] which employs repeated application of the chain rule to compute the derivatives of complicated functions. Note that, because we do not need explicit expressions for the derivatives, we are free to route the external momentum as we wish when we evaluate the loop integrals. Optimal routing of the loop momenta can significantly assist numerical integration.

These features are implemented in a transparent way using the class and operator overloading capabilities of C++. The result is a versatile suite of software which is essentially action independent and can easily be adapted for other calculations. All of the results presented here have been computed or checked using this automated approach.

Numerical Integration

The lattice integrals which did not involve derivatives, were evaluated using the adaptive Monte Carlo integration package VEGAS. In all of our VEGAN integrals we transformed to hyperspherical coordinates. The Jacobian of this transformation suppresses peaks in the integrands and, in some cases, can drastically improve convergence to the exact solution.

In other more complicated cases, it was better to approximate the loop integrals by discrete sums over hypercubic lattices. To eliminate zero-modes in the quark and gluon propagators, we applied twisted boundary conditions.

Twisted LPT

In the pure gauge theory, twisted periodic boundary conditions are implemented by requiring that the link variables satisfy

$$U_\mu(x + L\hat{\nu}) = \Omega_\nu U_\mu(x)\Omega_\nu^\dagger, \tag{5.38}$$

where L is the length of the twisted directions denoted $\hat{\mu}$ and $\hat{\nu}$. Here, we have chosen to apply the twist to two directions and we take the other directions to be infinite in extent. The twist matrices are constant $SU(3)$ matrices which obey

$$\Omega_\mu\Omega_\nu = \exp(2\pi i/3)\,\Omega_\nu\Omega_\mu, \quad \Omega_\mu^3 = \Omega_\nu^3 = 1. \tag{5.39}$$

Note that these conditions fix the twist matrices up to a unitary transformation only. Expanding the link variables in powers of the coupling yields the same boundary conditions for the vector potential

$$A_\mu(x + L\hat{\nu}) = \Omega_\nu A_\mu(x)\Omega_\nu^\dagger, \tag{5.40}$$

The Fourier transform of the twisted field is

$$A_\mu(x) = (3L^2)^{-1} \sum_{k_\perp} \int_{k_{||}} e^{-ikx}\Gamma_k \tilde{A}_\mu(k), \tag{5.41}$$

with a sum over twisted momenta $k_\perp$, and the usual integral (sum) over momenta $k_{||}$ along the other directions. Momentum-dependent colour matrices Γ_k replace the usual Gell-Mann matrices, and, according to Eq. 5.40, these new matrices must satisfy

$$\Omega_\mu\Gamma_k\Omega_\mu^\dagger = e^{ik_\nu L}\Gamma_k. \tag{5.42}$$

This places the following constraint on the momenta in the twisted directions

$$k_\nu = \frac{2\pi n_\nu}{3L}, \quad n_\nu \in \mathcal{Z}. \tag{5.43}$$

A number of the properties of the Γ_k matrices are listed in Ref. [9]; the property which most concerns us here is

$$\Gamma_k = 1, \quad \text{if } k_\perp = 0, \text{ mod}(3). \tag{5.44}$$

The usual trace condition on the vector potential, $\text{Tr}A_\mu = 0$, therefore implies that

$$\tilde{A}_\mu(k) = 0, \quad \text{if } k_\perp = 0, \text{ mod}(3). \tag{5.45}$$

It is easy to see that the free gluon propagator on the twisted lattice is

$$D_{\mu\nu}^{twist}(k) = \chi_k \, z(k,k) D_{\mu\nu}(k), \tag{5.46}$$

where $z(k,k)$ is a momentum-dependent function which depends on the choice of the twist matrices and hence Γ_k; and χ_k is a veto function

$$\chi_k = \begin{cases} 1 & \text{if } k_\perp \neq 0, \text{ mod}(3), \\ 0 & \text{if } k_\perp = 0, \text{ mod}(3). \end{cases} \tag{5.47}$$

Therefore, the twisted boundary conditions eliminate the zero-mode in the gluon propagator.

Twisted LPT proceeds in much the same way as the infinite volume LPT, with the integral over the twisted momenta replaced by a sum. In perturbative calculations, we do not need to construct the Γ_k matrices explicitly, we only need to evaluate the relevant traces. The trace over colour matrices then leads to the appearance of additional momentum dependent factors in the lattice integrands. The twist matrices should therefore be chosen carefully to simplify the integrands as much as possible.

Wohlert [31] generalised twisted lattice perturbation theory to calculations involving quarks. Drawing on the work of Parisi [32], he attributed to the quark fields an additional degree of freedom — smell — so that the quark fields could be represented as 3×3 matrices in smell-colour space. The same arguments presented for the twisted gauge fields then hold for quarks except that there is no analogous trace condition on the quark fields which means that zero modes in the quark propagator are allowed. These are excluded by applying anti-periodic boundary conditions, so that the twisted quark momenta can only occur in half-integer multiples of the effective gluon mass, $2\pi/(3L)$.

Discrete summation tends to work quite well for lattice Feynman integrals and the convergence of the sums is greatly assisted by the mass gap introduced by the twist. However, in order to obtain a final result, it is necessary to remove the infrared cutoff. To do this, we repeat our calculations for a number of lattice sizes and extrapolate to the infinite volume limit using the asymptotic form [9]

$$\Sigma(p; L) \approx_{L\to\infty} \sum_{n=0}^{\infty} \left(c_n^{(0)} + c_n^{(1)} \ln(L)\right) L^{-n}. \tag{5.48}$$

The quantities that we computed were infrared-finite and so $c_0^{(1)} = 0$.

Tadpole improvement

At one-loop, the contribution of mean-field improvement to the self energy is given by the difference of the free inverse propagator and the tadpole-improved inverse propagator. The tadpole-improved propagator is determined from the Fourier transform of the quark matrix with the link variables set to unity but the tadpole coefficients retained; we denote this $S_{\text{T.I.}}^{-1}$. The mean-field contribution is

$$\Sigma_{\text{T.I.}}^{(1)}(p) = \frac{1}{g_0^2}\left[S_{\text{T.I.}}^{-1}(p) - S_0^{-1}(p)\right]. \tag{5.49}$$

In this work the mean link in Landau gauge was used to define the improvement coefficients. The tadpole coefficients can be expanded as

$$u_\mu = 1 - g_0^2 u_\mu^{(1)} + \mathcal{O}(g_0^4). \tag{5.50}$$

On the 3+1 anisotropic lattice, the one-loop coefficients are given by

$$u_t^{(1)} = \frac{C_F}{2\xi^3} \int_{-\pi}^{\pi} \frac{d^4k}{(2\pi)^4} \hat{D}_{00}^{\alpha=0}(k), \tag{5.51}$$

$$u_i^{(1)} = \frac{C_F}{2\xi} \int_{-\pi}^{\pi} \frac{d^4k}{(2\pi)^4} \hat{D}_{ii}^{\alpha=0}(k), \tag{5.52}$$

where the colour factor, $C_F = 4/3$ for $SU(3)$. From the additional powers of anisotropy in its denominator, we might expect the one-loop contribution to the temporal tadpole coefficient to be small relative to the spatial tadpole coefficient on highly anisotropic lattices. This is exactly what was observed when the coefficients were evaluated numerically. Table 5.1 shows the one-loop coefficients for a range of anisotropies. These one-loop results support our choice of $u_t = 1$ in the non-perturbative investigation.

Hart et al. have computed the Landau-gauge tadpole improvement parameters to two-loop order for the Symanzik-improved anisotropic gauge action in the fundamental representation [35]. Their gluon propagator, which they do not express explicitly but rather evaluate numerically, is identical to the one used in this study and our values of the one-loop coefficients are in precise agreement with their results.

5.4.1 Rest mass renormalisation

It is not difficult to compute the quark rest mass to one-loop order. An expression for the one-loop coefficient in terms of the components of the quark self-energy is easily derived from Eq. 5.34 and the resulting loop integrals are straightforward to evaluate using VEGAS. However, we first corrected for the additive quark mass renormalisation, so that zero bare mass does in fact correspond to massless quarks.

ξ	$u_s^{(1)}$	$u_t^{(1)}$
1	0.06308(1)	0.064644(12)
2	0.08679(2)	0.016933(32)
3	0.09563(2)	0.007365(1)
4	0.09951(2)	0.004076(1)
5	0.10152(2)	0.002584(1)
6	0.10268(2)	0.001784(1)
7	0.10334(2)	0.001306(1)

Table 5.1: One-loop tadpole improvement coefficients for various anisotropies.

The critical quark mass, m_c, is defined as the bare-mass value which gives $M_1 = 0$. From Eq. 5.34, it follows that

$$a_t m_c = \mathcal{C}(0, \mathbf{0}). \tag{5.53}$$

and we can reformulate Eq. 5.34 as

$$1 + a_t m_{\text{sub}} - \mathcal{C}_{\text{sub}} - \cosh(a_t M_1) = (1 - A_0)\sinh(a_t M_1), \tag{5.54}$$

where the subtracted bare mass is given by

$$m_{sub} = m_0 - m_c, \tag{5.55}$$

and $\mathcal{C}_{\text{sub}} = \mathcal{C} - a_t m_c$. Note that the physical quark mass vanishes for $m_{\text{sub}} = 0$. This reparametrisation can be absorbed into a redefinition of the bare mass so that the effective tree-level rest mass is

$$M_1^{(0)} = \frac{1}{a_t}\ln(1 + a_t m_{\text{sub}}). \tag{5.56}$$

The one-loop correction is then given by

$$a_t M_1^{(1)} = e^{-a_t M_1^{(0)}} \text{Tr}\left[\left(\frac{\gamma_0 + 1}{4}\right)\left(a_t\Sigma^{(1)}(iM_1^{(0)}, \mathbf{0}) - a_t\Sigma^{(1)}(0, \mathbf{0})\right)\right]. \tag{5.57}$$

ξ	unrotated	ARIA
1	−0.0642903(4)	−0.023163(14)
2	−0.0333631(3)	−0.016544(8)
3	−0.0205977(3)	−0.0112296(65)
4	−0.0143917(2)	−0.0084007(51)
5	−0.0108892(2)	−0.0067190(43)
6	−0.00868868(14)	−0.0056192(37)
7	−0.00719597(14)	−0.0048389(33)

Table 5.2: Critical quark masses for a range of anisotropies. All the results are tadpole-improved. The column on the left contains one-loop coefficients for the action used in the numerical study described in Chapter 4. The column on the right contains the corresponding values for the rotated quark action. The uncertainties are VEGAS error estimates.

Eq. 5.53, which defines the critical mass, is not in closed form so that it is difficult to compute m_c exactly. However, to one-loop precision, we can replace m_{sub} by the original bare mass, m_0, when evaluating loop integrals. All the results in this chapter are given in terms of the subtracted bare mass.

Table 5.2 shows one-loop critical quark masses over a range of anisotropies. Tadpole-improved results for the rotated quark action and the unrotated action used in the simulations are given. As expected, corrections to the rotated action are slightly smaller. Note, however, the decrease in the magnitude of the critical quark masses with increasing anisotropy.

Figure 5-3 shows the one-loop correction to the rest mass as a function of the tree-level rest mass for the unrotated action used in our simulations for a range of anisotropies. The figure shows tadpole-improved corrections only. The coefficients were again evaluated using VEGAS. The external momentum was routed through the quark propagator to prevent a pole in the integrand from crossing the real k_0 axis [27]. Corresponding data are given in Table 5.3. Table 5.4 contains rest mass corrections for ARIA for the same bare anisotropy values.

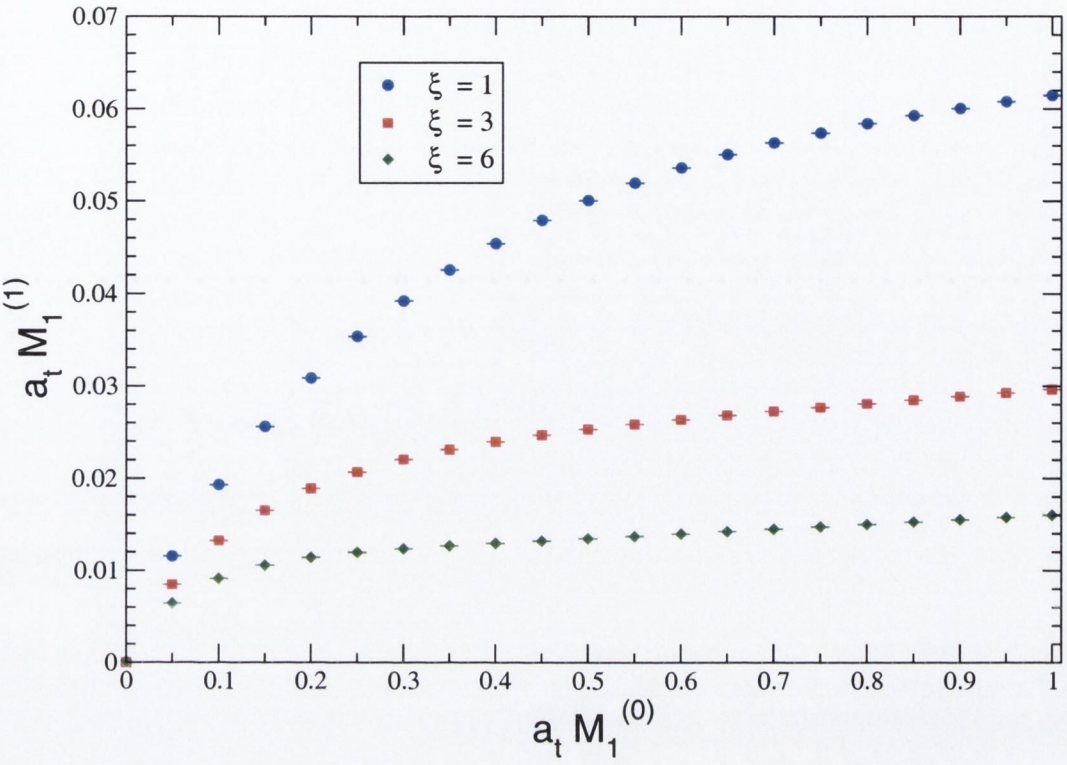

Figure 5-3: Rest mass corrections for the unrotated quark action used in our simulations. The plot shows corrections for three different anisotropies.

5.4.2 Speed of light renormalisation

With the tree-level value of μ_r tuned according to Eq. 5.29, the one-loop coefficient can be expressed as

$$\mu_r^{(1)} = \left(\frac{e^{2a_t M_1^{(0)}}}{\mu_r^{(0)}} - \mu_r^{(0)} \right) \frac{M_1^{(1)}}{2M_1^{(0)}} + \frac{\mu_r^{(0)}}{2} Z_{M_2}^{(1)}, \tag{5.58}$$

where the kinetic mass renormalisation factor,

$$Z_{M_2} = \frac{\mu_r^2 M_2}{\sinh(a_t M_1)} e^{-a_t M_1}, \tag{5.59}$$

gives a measure of the difference between M_1 and M_2 due to radiative corrections. To one-loop order $M_1^{(1)}$ and $Z_{M_2}^{(1)}$ are independent of $\mu_r^{(1)}$ and Eq. 5.58 is a closed expression for the correction to the action. Explicitly, the one-loop kinetic mass

	$a_t M_1^{(1)}$		
$a_t M_1^{(0)}$	$\xi = 1$	$\xi = 3$	$\xi = 6$
0	0.000000(0)	0.000000(0)	0.000000(0)
0.1	0.019283(10)	0.013246(3)	0.009100(1)
0.2	0.030843(9)	0.018920(3)	0.011394(1)
0.3	0.039171(10)	0.022061(3)	0.012327(2)
0.4	0.045359(9)	0.023980(3)	0.012917(2)
0.5	0.050011(10)	0.025318(3)	0.013432(2)
0.6	0.053551(10)	0.026396(3)	0.013947(2)
0.7	0.056259(10)	0.027277(3)	0.014480(2)
0.8	0.058353(10)	0.028195(3)	0.015004(2)
0.9	0.060000(10)	0.028920(3)	0.015519(3)
1.0	0.061418(15)	0.029700(3)	0.016029(3)

Table 5.3: Rest mass renormalisation for the unrotated action. These values are plotted in Figure 5-3.

renormalisation is

$$\begin{aligned} Z_{M_2}^{(1)} &= 2\frac{\xi}{\mu_r^{(0)}}\mathcal{A}_i^{(1)}(iM_1,\mathbf{0}) - \left[1+\cosh\left(a_tM_1^{(0)}\right)e^{-a_tM_1^{(0)}}\right]\mathcal{A}_0^{(1)}(iM_1,\mathbf{0}) \\ &\quad -\xi^2 a_tM_1^{(0)}e^{-a_tM_1^{(0)}}\frac{d^2}{d(a_sp_i)^2}\left[\mathcal{A}_0^{(1)}(iM_1,\mathbf{0})\sinh\left(a_tM_1^{(0)}\right) - C^{(1)}(iM_1,\mathbf{0})\right], \end{aligned} \tag{5.60}$$

or, in a form more suited to automated evaluation

$$\begin{aligned} Z_{M_2}^{(1)} &= \frac{\mathrm{Tr}}{4}\left[\left(-i\frac{2\xi}{\mu_r^{(0)}}\gamma_i\frac{\partial}{\partial(a_sp_i)} + i\gamma_0\mathrm{cosech}\left(a_tM_1^{(0)}\right)\right)a_t\Sigma^{(1)}(p)\right]_{p=(iM_1^{(0)},\mathbf{0})} \\ &\quad +e^{-a_tM_1^{(0)}}\left[\left(\xi^2a_tM_1^{(0)}\frac{\partial^2}{\partial(a_sp_i)^2} + i\frac{\partial}{\partial(a_tp_0)}\right)\mathrm{Tr}\left(\left(\frac{\gamma_0+1}{4}\right)a_t\Sigma^{(1)}(p)\right)\right]_{p=(iM_1^{(0)},\mathbf{0})}. \end{aligned} \tag{5.61}$$

For massless quarks, the correction to the dispersion relation is greatly simplified

	$a_t M_1^{(1)}$		
$a_t M_1^{(0)}$	$\xi = 1$	$\xi = 3$	$\xi = 6$
0	0.00000(0)	0.00000(0)	0.00000(0)
0.1	0.02417(2)	0.01538(4)	0.01018(1)
0.2	0.03991(2)	0.02299(4)	0.01344(1)
0.3	0.05181(2)	0.02779(4)	0.01506(1)
0.4	0.06108(2)	0.03101(4)	0.01608(1)
0.5	0.06834(2)	0.03328(5)	0.01681(1)
0.6	0.07403(2)	0.03492(5)	0.01738(1)
0.7	0.07846(2)	0.03611(5)	0.01787(1)
0.8	0.08191(2)	0.03704(5)	0.01832(1)
0.9	0.08458(2)	0.03781(5)	0.01869(1)
1.0	0.08657(2)	0.03839(5)	0.01949(1)

Table 5.4: Rest mass renormalisation for ARIA. All values are coefficients of ${g_0}^2$.

and is given by

$$\begin{aligned} \mu_r^{(1)} &= \xi \mathcal{A}_1(0,\mathbf{0}) - \mathcal{A}_0(0,\mathbf{0}) \\ &= -i\mathrm{Tr}\left[\xi \frac{\gamma_1}{4}\frac{\partial \Sigma(p)}{\partial p_1} - \frac{\gamma_0}{4}\frac{\partial \Sigma(p)}{\partial p_0}\right]_{p=(0,\mathbf{0})}, \end{aligned} \tag{5.62}$$

which corresponds to the tuning criterion used in Ref. [39]. The partial derivatives appearing in the lower term in Eq. 5.60 and in Eq. 5.62 are separately infrared divergent with the logarithmic divergences cancelling in the full terms. Since the lattice theory approximates the infrared behaviour of the continuum, divergences only appear through the rainbow contribution to the self-energy.

Numerically, such integrals are problematic. VEGAS cannot handle the sharp peaks in the lattice integrands. Therefore, it is a good idea to integrate over k_0 analytically [27, 37, 38]; the remaining 3-D integrals can then be evaluated numerically. However, with our complicated gluon propagator this was not feasible.

The easiest way to circumvent this problem is to compute the one-loop energy for a range of small external momenta and extract the required coefficients from fits to polynomials in the momenta. Unfortunately, we were unable to achieve the desired level of accuracy using this approach.

It was therefore necessary to introduce an infrared regulator to evaluate the integral. Two different regulators were tried. In the first instance, we introduced a small gluon mass, λ. We could then evaluate the integrals using VEGAS for different values of λ and extrapolate to $\lambda = 0$ with a fit similar to Eq. 5.48

$$\Sigma(p;\lambda) \approx \sum_{n=0}^{\infty} \left(c_n^{(0)} + c_n^{(1)} \ln(a_t^2\lambda^2)\right) (a_t\lambda)^{2n}. \tag{5.63}$$

The gluon mass is a gauge invariant regulator up to two-loop corrections allowing us to check the gauge invariance of $\mu_r^{(1)}$ for finite λ.

This procedure worked quite well for light quarks. However, with increasing quark mass, peaks in the quark propagator and its derivatives become sharper and integrals are more difficult to estimate accurately with VEGAS. The extrapolation to the final result therefore became increasingly unreliable. In this case, the possibility of improving the convergence of the numerical integration package by subtracting from the lattice integrands suitable analytic expressions was also explored. More specifically, we followed the example of Ref. [41] and considered continuum-like integrands, defined within a hypersphere contained inside the lattice Brillouin zone. However, at finite lattice spacing, these expressions must be tuned to match exactly the complicated low-momentum behaviour of the lattice integrands. Our tuning criteria differ from those used in Ref. [41] and suitable expressions were not readily identifiable.

In the second approach, the loop integrals were replaced by discrete sums on finite lattices. We applied doubly-twisted periodic boundary conditions along the $\mu = 2, 3$ spatial directions. For the one-loop integrands considered, the zero-momentum veto function in the twisted gluon propagator is enough to eliminate singularities in the lattice integrands, and we did not have to resort to anti-periodic boundary conditions to eliminate fermionic zero modes. The untwisted directions were made sufficiently large to approximate the infinite volume limit. To increase the effective mass gap and, hence, improve the convergence of the mode summation, we made the following change of variables along these directions: $k'_\mu \to k'_\mu - \alpha_\mu \sin(k'_\mu)$ with $0 \leq \alpha_\mu < 1$.

We now present results for $\mu_r^{(0)}$ at zero quark mass for a range of anisotropies. To obtain these results, the rainbow and tadpole contributions were computed together on a sequence of lattices. We allowed the extent of the twisted directions to vary between 20 and 40 lattice sites. Derivatives with respect to external momenta were taken along the untwisted directions, in which case, the colour matrices could be chosen such that there were no additional momentum-dependent factors in the twisted integrands. With $\alpha_\mu \sim 1$, varying the extent of the untwisted directions between 100 and 150 lattice sites had a negligible effect on the results of the mode summation. The infinite-volume results were obtained from least-squares fits to the asymptotic expansion in Eq. 5.48. To perform the fit, the expansion was truncated after terms of $\mathcal{O}(1/L^2, \ln(L)/L^2)$. However, the difference between the asymptotic value and the sum for any finite length, L, was a fraction of a percent. Therefore, in practice, to a high precision the extrapolation to infinite L was unnecessary.

In Figure 5-4, we plot the one-loop correction for the unrotated asymmetric quark action as a function of the anisotropy. The figure shows coefficients obtained using both naive and tadpole-improved perturbation theory. The corresponding values are given in Table 5.5. The third column contains the contribution of the field rotations which can be added to the corresponding values in the preceding columns to obtain results for the rotated action. The unimproved coefficients have been rounded to 5 decimal places. The errors on the values in the other columns are VEGAS estimates.

At finite quark mass, the one-loop coefficient of μ_r proved much more difficult to evaluate. To reduce computation, the results presented here were obtained in Feynman gauge where we separated the problematic term in the kinetic mass renormalisation into a piece which involves the diagonal elements of the gauge propagator and a piece containing contributions from the off-diagonal elements. The off-diagonal contribution does not appear in the continuum and is easy to evaluate. The diagonal contribution was evaluated using doubly-twisted mode summation. The extent of the twisted directions was varied between 14 and 25 lattice sites. This time, the mode sums showed a much stronger dependence on the extent of the untwisted directions

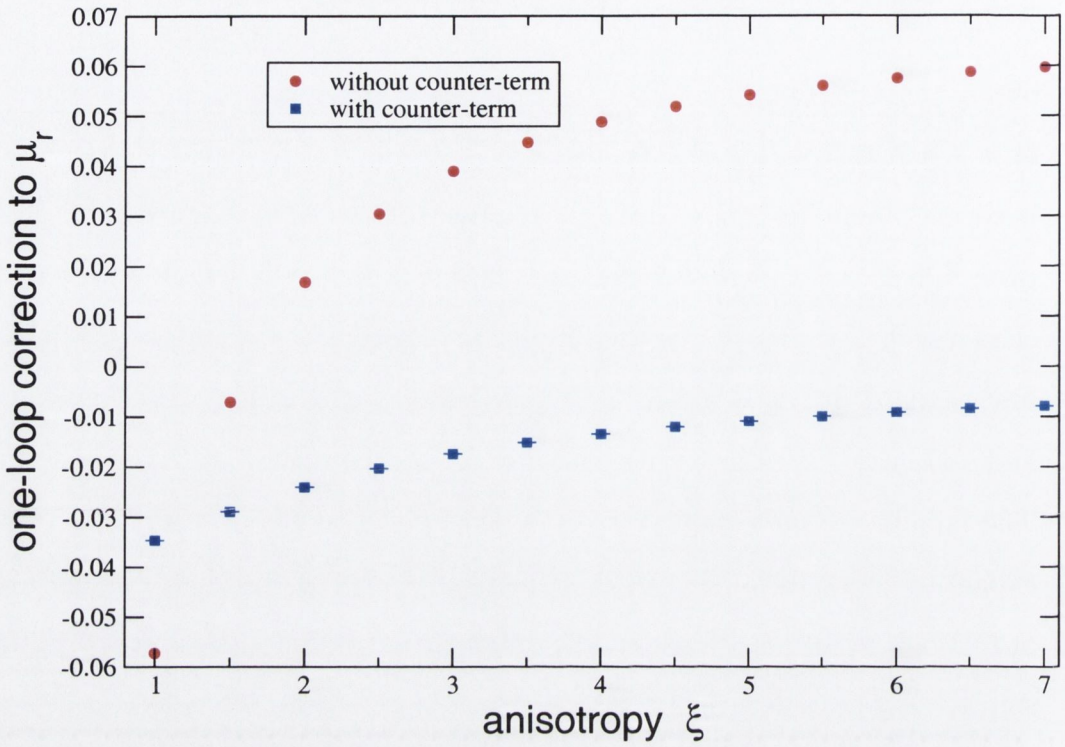

Figure 5-4: One-loop coefficient of μ_r at $m_q = 0$ for the unrotated anisotropic quark action. The plot shows results for both naive and tadpole-improved perturbation theory.

than in the case of the massless integrals. To approximate an infinite extent along the untwisted directions required about 300 lattice sites. Varying the extent of the untwisted directions from 300 to 400 lattice sites affected the results of the sum, at most, in the sixth significant digit. The extrapolated results themselves constitute only a very small part of the final answers and we ignored this very slight variation in our extrapolations to the infinite-volume limit. Table 5.6 contains the one-loop coefficients of μ_r for the unrotated anisotropic quark action at an anisotropy of 6. The data is plotted in figure 5-5. The data shows a mild, slightly non-linear mass dependence. The tadpole-improved coefficient changes by less than 0.1 over the range of bare mass values considered.

ξ	μ_r	μ_r with T.I.	rotation
1.0	−0.05724	−0.03462(2)	0.016153(6)
1.5	−0.00705	−0.02887(2)	0.005022(3)
2.0	0.01692	−0.02399(2)	−0.000043(3)
2.5	0.03048	−0.02027(2)	−0.003335(2)
3.0	0.03899	−0.01739(2)	−0.004700(2)
3.5	0.04473	−0.01516(2)	−0.005984(2)
4.0	0.04882	−0.01344(2)	−0.006940(1)
4.5	0.05186	−0.01206(3)	−0.007698(3)
5.0	0.05419	−0.01090(3)	−0.008296(2)
5.5	0.05603	−0.00996(2)	−0.008799(2)
6.0	0.05751	−0.00911(2)	−0.008837(3)
6.5	0.05873	−0.00839(2)	−0.009582(3)
7.0	0.05975	−0.00782(2)	−0.009905(3)

Table 5.5: One-loop corrections to μ_r at zero quark mass. Results are shown with and without tadpole improvement

$a_t m_{sub}$	μ_r	μ_r with T.I.
0.0	0.05751(0)	-0.00911(2)
0.1	0.02160(7)	-0.02053(9)
0.2	-0.00872(9)	-0.03087(12)
0.3	-0.03450(13)	-0.04013(16)
0.4	-0.05654(15)	-0.04834(18)
0.5	-0.07573(18)	-0.05585(22)
0.6	-0.09258(19)	-0.06274(23)
0.7	-0.10734(23)	-0.06896(28)
0.8	-0.12026(24)	-0.07451(29)
0.9	-0.13187(25)	-0.07969(30)
1.0	-0.14237(26)	-0.08469(32)

Table 5.6: One-loop corrections to μ_r, at $\xi = 6$, as a function of the subtracted bare quark mass.

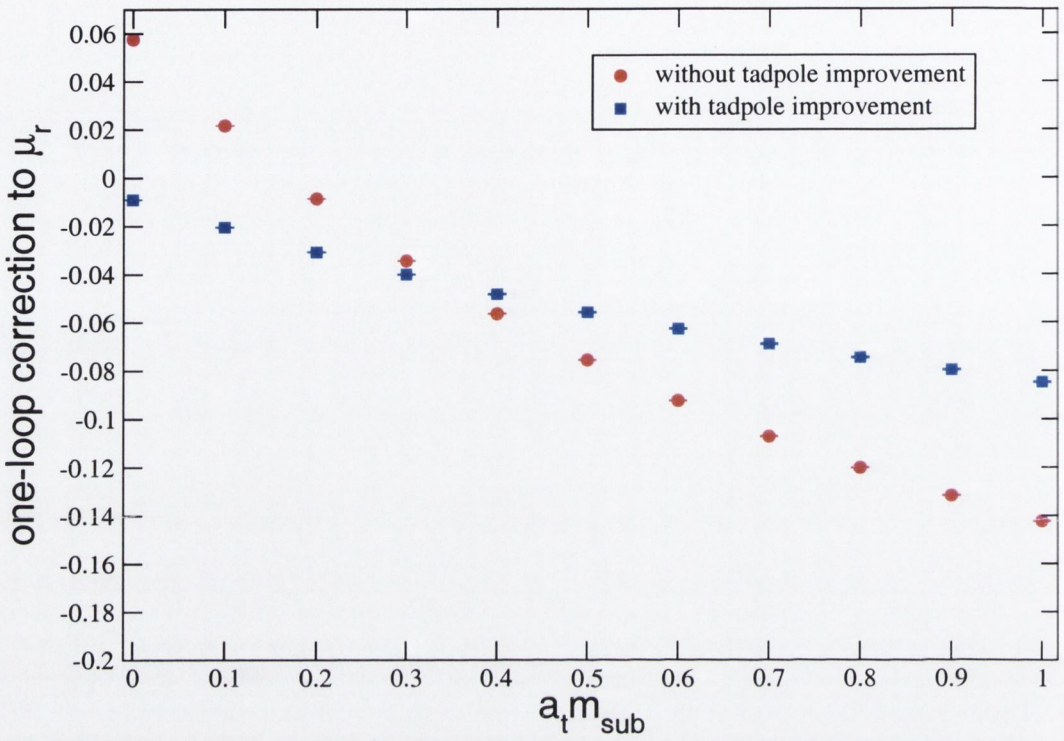

Figure 5-5: One-loop coefficient of μ_r at $\xi = 6$ as a function of the subtracted bare mass for the unrotated anisotropic quark action. The plot shows results for both naive and tadpole-improved perturbation theory.

5.4.3 A comparison with simulation

At sufficiently fine lattice spacings, radiative corrections are dominated by one-loop effects and it should be possible to tune the action couplings perturbatively. We therefore compared the perturbative results with the results of the non-perturbative study of the fermion action detailed in Chapter 4. However, before we present our findings, it is necessary to comment on our definitions of the tadpole improvement coefficient. Clearly, the fourth root of the average plaquette, which was used to define the tadpole coefficient in our simulation, and the mean link in Landau gauge must agree qualitatively. However, it is not clear a priori how precisely these independent estimates should agree. Shakespeare and Trottier [29] have compared both tadpole renormalisation schemes in quenched simulations. That study involved the NRQCD fermion action and an $\mathcal{O}(a^2)$ tadpole-improved gauge action on isotropic lattices. At a lattice spacing of approximately 0.21 fm, they find that the tadpole coefficient

determined from the average plaquette agrees with the mean link computed numerically to within about 6%.[2] The discrepancy increases on coarser lattices where the Landau gauge definition of the tadpole coefficient is more effective in reducing radiative corrections. Although it is not possible to draw direct conclusions from that study, it seems reasonable to infer that on the anisotropic lattice used in our quenched simulation, which had a spatial lattice spacing of 0.21 fm, the two definitions of the tadpole coefficient should differ by no more than a few percent.

The anisotropic tadpole-improved coupling used in the simulation was $\beta = 2$ and the expectation value of the spatial plaquette used to define the tadpole improvement coefficient was $\langle P_{ij} \rangle = 0.3817$. If one-loop effects are dominant, substituting these values into Eq. 5.50 should yield an estimate for the one-loop coefficient which is consistent with the result $u_s^{(1)} = 0.10268(2)$ given in Table 5.1. However, this estimate yields a value of approximately 0.0713 which differs substantially from the perturbative prediction. This mismatch again manifests itself in the determination of the critical quark mass. Multiplying the one-loop critical quark mass coefficient by the tadpole improved coupling used in our numerical investigation yields a critical quark mass of -0.0261. On the other hand, in the numerical study, a bare mass of $a_t m_q = -0.04$ corresponded to a physical value which was close to the strange quark mass.[3]

We therefore deduce that, on the spatially coarse lattice used in the quenched numerical investigation, the action coefficients cannot be determined to a satisfactorily high precision using one-loop perturbation theory. One may then ask whether the discrepancies mentioned above are due to non-perturbative effects or if they can be attributed to higher-order radiative corrections which can be controlled by using a finer lattice spacing or eliminated by performing higher-loop perturbative calculations. With regard to this question, it is possible to make a few tentative remarks.

[2]The mean link in Landau gauge is slightly smaller than the fourth root of the average plaquette.

[3]In this case, however, one should also remember that the critical mass is quite sensitive to the choice of tadpole renormalisation scheme since the corresponding calculation involves the cancellation of a large tadpole contribution to leave a small remainder.

At a bare anisotropy of two and for bare coupling values $g_0^2 < 2$, Hart et. al [35] find excellent agreement between the Landau-gauge mean link computed at second order in perturbation theory and the corresponding numerical value. Their results differ from ours due to the appearance of the adjoint term in the gauge action used in our work. In addition, they have not computed two-loop coefficients for a bare anisotropy of 6 which has been considered here. However, at an anisotropy of 4, their second-order coefficient is approximately 10% of the one-loop coefficient. A similar two-loop contribution in our calculations could account for the discrepancies noted above.

Finally, note that the tadpole-improved bare coupling has been used to compare the perturbative calculation with numerical results. A better choice of expansion parameter might be a renormalised coupling, determined numerically by computing some suitable physical quantity at the optimal momentum scale as outlined in Ref. [14]. However, because the lattice theory has been formulated in terms of tadpole-improved links, one expects the bare coupling to be a good expansion parameter at moderate lattice spacings. The use of a renormalised coupling is not expected to change the results significantly.

5.5 Conclusions

In this chapter, we investigated the properties of the anisotropic fermion action, both at the tree-level and at one-loop in perturbation theory. Unlike the anisotropic SW action discussed in Ref. [17], at the tree-level the dispersion relation for ARIA is free of both large $a_s m_q$ errors and doubler effects. Corrections to the dispersion relation of order $a_t m_q$ can be absorbed into a redefinition of the 'speed of light' parameter, μ_r, which multiplies the kinetic term in the fermion action.

Beyond the tree-level, the speed of light parameter can be tuned from the quark self-energy. This was done at one-loop in perturbation theory for both massless quarks and finite quark masses.

Lattice perturbative calculations are extremely complicated and, to reduce the chances for error, the evaluation of the spinor algebra and momentum derivatives in the lattice loop integrands was automated.

At finite quark mass, corrections to the dispersion relation were obtained from the rest mass and kinetic mass renormalisation factors. The rest mass renormalisation was straightforward to evaluate. However, the kinetic mass was more difficult to calculate numerically because of intermediate infrared divergences. Similarly, corrections in the zero mass limit also exhibit intermediate divergences. To overcome such problems, previous studies have integrated over the temporal loop momentum analytically. In our case, because of the complexity of the gauge action, this was not practical. In any case, it is not in keeping with an automated approach to perturbation theory. To evaluate these loop integrals, we introduced an intermediate infrared regulator. A small gluon mass can be used as a gauge invariant regulator for the class of diagrams considered in this study. However, more accurate results were obtained using mode summation on a lattice with doubly-twisted periodic boundary conditions.

Results were presented for the one-loop tadpole improvement coefficients which are in exact agreement with the results presented in Ref. [23]. Values for the critical quark mass and the rest mass renormalisation were determined for a range of anisotropies. Finally, we presented one-loop corrections to the speed of light at zero-quark mass for a range of anisotropies and for a number of quark masses at a fixed value of the anisotropy, $\xi = 6$.

It had been intended to build on the framework which was developed in this calculation and compute additional corrections to the fermion action at one-loop in perturbation theory. However, direct comparison between the one-loop perturbative results and the non-perturbative determination of the critical quark mass and tadpole-improvement coefficient at $\xi = 6$ did not show quantitative agreement. A comparison with a similar calculation indicated that the discrepancy may be due to two-loop contributions. This argument is by no means conclusive and can only

be resolved by running on finer lattices or performing second-order perturbative calculations. In the next chapter, the non-perturbative determination of the bare anisotropies on dynamical background configurations will be described. The inclusion of sea quarks greatly complicates the non-perturbative renormalisation program and the possibility of performing precise perturbative calculations on spatially-coarse anisotropic lattices would be a great advantage to the development of the anisotropic formalism.

Chapter 6

Static-light hadrons on a dynamical anisotropic lattice

In this chapter, we describe a study of heavy-light hadrons in the static quark limit. First, a review is in order. In Chapter 4, we investigated the non-perturbative tuning of the quark anisotropy parameter in the quenched approximation. That study indicated that relativistic charm quark simulations are feasible on the anisotropic lattice at $\xi = 6$. Simulations of the b-quark on spatially-coarse lattices requires the use of a larger anisotropy which necessitates a retuning of the action parameters. More work is therefore required before we can accurately simulate QCD at the b-quark mass. In the meantime, using ARIA, simulations can be performed close to the charm quark mass and the results extrapolated to that of the b-quark. In studies of hadrons containing a single heavy quark these extrapolations are guided by heavy quark effective theory (HQET). More reliable predictions can be made by performing a simulation in the static limit where the heavy quark becomes infinitely massive, transforming the extrapolation in the heavy quark mass into an interpolation. Simulations of static quarks are possible because, in the static limit, the hadron dynamics are independent of the heavy quark mass and discretisations of the static quark action do not suffer from mass-dependent cutoff effects.

Simulations of heavy-light hadrons in the static limit can yield important phys-

ical results in their own right. Experimentally, little is known of the excited state spectrum of mesons and baryons which contain a single b-quark and this is an area of immediate applicability for static-light simulations.

In the static limit, the heavy quark reduces to a static colour source. Jaffe [44] has recently proposed that static-light systems be used to investigate colour non-singlet states which may exist inside hadrons. This formalism can be used to study the contribution of internal quark correlations to the observed properties of hadrons.

6.1 The static approximation

Heavy-light systems share the following features: the spatial extent of the hadron is determined by the light degrees of freedom and is of the order of $1/\Lambda_{\rm QCD}$. Therefore, interactions between the heavy quark and the light degrees of freedom typically involve the exchange of soft gluons. On the other hand, the Compton wavelength of the heavy quark is approximately $1/m_Q$, where m_Q denotes the heavy quark mass. This is much less than the typical gluon wavelength inside the hadron. Therefore, the light degrees of freedom find it difficult to resolve the heavy quark structure. This leads to an approximate symmetry where the observable properties of heavy-light hadrons are insensitive to the spin and flavour of the constituent heavy quark. In the static limit, $m_Q \to \infty$, this approximate symmetry becomes exact.

Formally, the static limit coincides with the lowest-order term in the $1/m_Q$ expansion of the HQET Lagrangian. The effective theory is derived by integrating out the heavy quark fields appearing in the QCD Lagrangian. To see how this is done consider a single heavy quark moving at the hadron's velocity, v, and interacting with the light constituents of the hadron. The heavy quark is slightly off-shell and has momentum

$$p = m_Q v + k, \tag{6.1}$$

where k is the residual momentum due to the interactions and is of order $\Lambda_{\rm QCD}$ and v is a four-vector which, therefore, satisfies $v^2 = 1$. To simplify matters we work in the rest frame of the hadron where $v = (1, \mathbf{0})$. To proceed, the heavy quark field is separated into upper and lower components[1], h and ϕ, by

$$h(x) = e^{im_Q t} P_+ \psi_h(x), \quad \phi(x) = e^{im_Q t} P_- \psi_h(x), \tag{6.2}$$

where the projection operators P_+ and P_- are given by

$$P_\pm = \frac{1 \pm \gamma_0}{2}. \tag{6.3}$$

By construction, the two-component fields in Eq. 6.2 are parity eigenstates with

$$\gamma_0 h = h, \quad \gamma_0 \phi = -\phi, \tag{6.4}$$

and the heavy quark field can be written

$$\psi_h(x) = e^{-im_Q t} \left[h(x) + \phi(x) \right]. \tag{6.5}$$

Inserting this expression into the heavy quark part of the QCD Lagrangian and using the properties of Eq. 6.5 yields

$$\begin{aligned} \mathcal{L}_{HQ} &= \bar{\psi}_h (i\gamma_\mu D_\mu - m_Q) \psi_h \\ &= \bar{h} i D_0 h - \bar{\phi}(iD_0 + 2m_Q)\phi \\ &\quad + \bar{h} i \gamma_i D_i \phi + \bar{\phi} i \gamma_i D_i h. \end{aligned} \tag{6.6}$$

The ϕ field therefore corresponds to excitations of mass $2m_Q$. It describes virtual heavy quark processes which are integrated out to obtain the effective theory. In the limit $m_Q \to \infty$, these processes die away and the heavy-quark Lagrangian is given

[1] We assume a non-relativistic realisation of the Dirac matrices.

by

$$\mathcal{L}_{\text{stat}} = \bar{h} i D_0 h. \tag{6.7}$$

Because heavy-quark pair creation cannot occur, the field h annihilates a quark but does not create a static-antiquark. The static quark Lagrangian has a U(1) symmetry which relates to the heavy quark conservation. The Lagrangian also has a manifest SU(2) symmetry associated with conservation of the heavy quark spin. For N_h heavy-quark flavours, this becomes an SU($2N_h$) spin-flavour symmetry.

In HQET, corrections to the static limit are organised as an expansion in $k/m_Q \sim \Lambda_{QCD}/m_Q$. The next-to-leading order term in the HQET Lagrangian includes a contribution from the heavy quark kinetic energy and a spin-spin interaction term. For the b-quark $\Lambda_{QCD}/m_Q \sim 0.1$, which indicates that corrections to the static-limit are of the order of 10%.

6.2 The static-light energy spectrum

In the continuum, heavy-light hadrons are classified according to their total angular momentum and parity, J^P. For mesons described by the constituent quark model, $J = S + L$, where S is the sum of the spins of the constituent quarks and L is the orbital angular momentum between them. The parity of these mesons is given by $P = (-1)^{L+1}$.

In the static limit, the heavy quark spin and hence the total angular momentum of the light degrees of freedom are conserved quantities. Because hadrons which differ only in the spin of the static quark are degenerate, it is more appropriate to label static-light channels J^P_ℓ where J_ℓ denotes the total angular momentum of the light degrees of freedom. Table 6.1 lists the S-wave, P-wave and D-wave static-light mesons. The column on the right lists the corresponding heavy-light states.

In addition, baryons containing a single static quark can be distinguished by the

L	J_ℓ^P	J^P	
0	$\frac{1}{2}^-$	0^-	1^-
1	$\frac{1}{2}^+$	0^+	1^+
1	$\frac{3}{2}^+$	1^+	2^+
2	$\frac{3}{2}^-$	1^-	2^-
2	$\frac{5}{2}^-$	2^-	3^-

Table 6.1: Static-light mesons for different orbital angular momenta (L). The rightmost column lists the corresponding channels once hyperfine interactions are included.

flavour content of their constituent light quarks. This study includes the static-light counterparts of the Λ_b and Σ_b baryons which transform as an isosinglet and isotriplet respectively. The Λ_b has $J_\ell^P = 0^+$ and for the Σ_b, $J_\ell^P = 1^+$.

6.3 Static quarks on the lattice

The static-quark lattice action used in our work was first proposed by Eichten and Hill [43] and is given by

$$S_{\text{stat}} = a_s^3 \sum_x \left[\bar{h}(x) \left(h(x) - U_t^\dagger(x - \hat{t}) h(x - \hat{t}) \right) \right]. \tag{6.8}$$

In position space, the static-quark propagator from a space-time point x to a point y is given by

$$G^Q(y, x) = \theta(y_0 - x_0)\delta(\mathbf{x} - \mathbf{y}) U_t^\dagger(y_0 - \hat{t}, \mathbf{x}) .... U_t^\dagger(x_0, \mathbf{x}) P_+. \tag{6.9}$$

By analogy, we define a static anti-quark propagator as

$$G^{AQ}(y, x) = \theta(y_0 - x_0)\delta(\mathbf{x} - \mathbf{y}) U_t(x_0 \mathbf{x}) .... U_t(y_0 - \hat{t}, \mathbf{x}) P_-. \tag{6.10}$$

Although the static quark propagator is inexpensive to compute, simulations of static-light systems are challenging. Using single point propagators for the light quark fields means that the source and sink operators of static-light correlators are confined to a

single spatial lattice site. This severely restricts the statistical accuracy with which measurements can be made. This restriction is compounded by the fact that the noise to signal ratio of static-light correlators grows exponentially with increasing temporal separation. For a static-light meson, the rate at which the ground-state signal degenerates into noise is given by [40, 42]

$$R_{NS}(t) = \sigma(t)/C(t) \sim e^{(\mathcal{E}_0 - (m_\pi + V(0))/2)t}. \tag{6.11}$$

$\mathcal{E}_0$ is the measured binding energy of the meson

$$\mathcal{E}_0 = \lim_{m_Q \to \infty} (E_0 - m_Q)\,. \tag{6.12}$$

$V(0)$ is the static inter-quark potential at zero separation and m_π is the mass of the pion on the lattice. Because the quark mass has been removed from the theory, in the static approximation the exponents appearing in two-point correlators are non-observable energy differences, $\mathcal{E}_n = \lim_{m_Q \to \infty}(E_n - m_Q)$. These energy differences contain a contribution from the static quark self-energy which diverges linearly with the inverse lattice spacing. For the Eichten-Hill action, $V(0) = 0$ and because of the linear divergence of the static-light binding energy, on realistic lattices, $\mathcal{E}_0 > m_\pi/2$. This leads to the exponential increase in the noise to signal ratio. To ameliorate the situation the Alpha collaboration [40] have proposed alternative discretisations of the static quark action. The parallel transporter in Eq. 6.8 is chosen so that the zero-separation interquark potential $V(0)$ assumes a positive value and cancels out some of the contribution of the binding energy in Eq. 6.11.

We, on the other hand, use a method called dilution [45] to evaluate the light quark propagators from all sites on the lattice to all other lattice sites. Using these all-to-all propagators allows us to place source and sink operators for static-light correlators at all spatial lattice sites yielding a dramatic increase in statistics. The dilution algorithm combines exact inversion of the fermion matrix with stochastic

estimation to optimally evaluate all-to-all propagators.

6.4 Computing all-to-all propagators

On realistic lattices the fermion matrix is too large to invert exactly and stochastic methods must be employed to estimate all-to-all propagators. A naive stochastic estimate of the inverse fermion matrix is obtained by first generating an ensemble of $\mathrm{N_r}$ noise vectors $\{\eta_{[1]}, \eta_{[2]} ..... \eta_{[N]}\}$. These noise vectors have the same form as the lattice quark fields and satisfy

$$\langle \eta(\alpha) \otimes \eta(\beta)^\dagger \rangle = \delta_{\alpha\beta}, \tag{6.13}$$

where α and β denote the collective quark field indices and the angle brackets denote an average over the ensemble. Both Z_2 and Gaussian noise vectors will satisfy this requirement. For a given gauge configuration, U, one solves for

$$\psi_{[i]} = M^{-1}(U)\eta_{[i]} \tag{6.14}$$

for each noise-vector in the ensemble. The full inverse fermion matrix is then approximated by

$$M^{-1}(U)_{\alpha\beta} \approx \langle \psi(\alpha) \otimes \eta(\beta)^\dagger \rangle. \tag{6.15}$$

This estimate only becomes exact in the limit $\mathrm{N_r} \to \infty$. It is not an efficient means of computing the full inverse fermion matrix because it relies on the cancellation of $\mathcal{O}(1)$ noise to extract a signal which, due to confinement, decays exponentially.

To improve the rate of convergence of the stochastic estimator we use Z_2 noise and partition each original noise vector

$$\eta_{[r]} = \sum_i \eta^{(i)}_{[r]}, \tag{6.16}$$

where the partitioning is implemented so that

$$\eta_{[r]}^{(i)} \otimes \eta_{[r]}^{(j)\dagger} = 0, i \neq j. \tag{6.17}$$

In the dilution algorithm this partitioning is done in a systematic way. For example, time dilution breaks each noise vector into pieces which have support only on a single time slice

$$\eta(\mathbf{x}, t) = \sum_{i=0}^{N_t - 1} \eta^{(i)}(\mathbf{x}, t), \tag{6.18}$$

with $\eta^{(i)}(\mathbf{x}, t) = 0$ if $i \neq t$. Following this example, the noise vectors may be diluted in any or all quark field indices. Each original noise vector, $\eta_{[r]}$, then provides an unbiased estimate of the inverse fermion matrix

$$M^{-1} \approx \sum_{i}^{N_{dil}} \psi_{[r]}^{(i)} \otimes \eta_{[r]}^{(i)\dagger}, \tag{6.19}$$

where, as in Eq. 6.14

$$\psi_{[r]}^{(i)} = M^{-1}(U)\eta_{[r]}^{(i)}. \tag{6.20}$$

We then average these estimates over the ensemble. Each component of the Z_2 noise vectors has modulus 1 and full dilution on a single noise vector corresponds to the exact inversion of the fermion matrix. Unlike the naive stochastic estimate, the dilution algorithm yields the exact propagator in a finite number of matrix inversions and gives more accurate results than the naive approach with a comparable number of inversions. This is clearly illustrated in Figure 6-1. This plot shows the effect of time dilution on a pseudoscalar correlator computed using quenched background configurations on a $12^3 \times 24$ lattice. The expected form of the correlator is given by Eq. 4.6. The circular points were obtained using a naive stochastic estimate of the inverse fermion matrix. 24 Z_2 noise sources were used for each fermion propagator.

The diamonds are were obtained from single noise sources which were diluted in time. This plot is shown in Ref. [45] and full details of the simulation are contained therein.

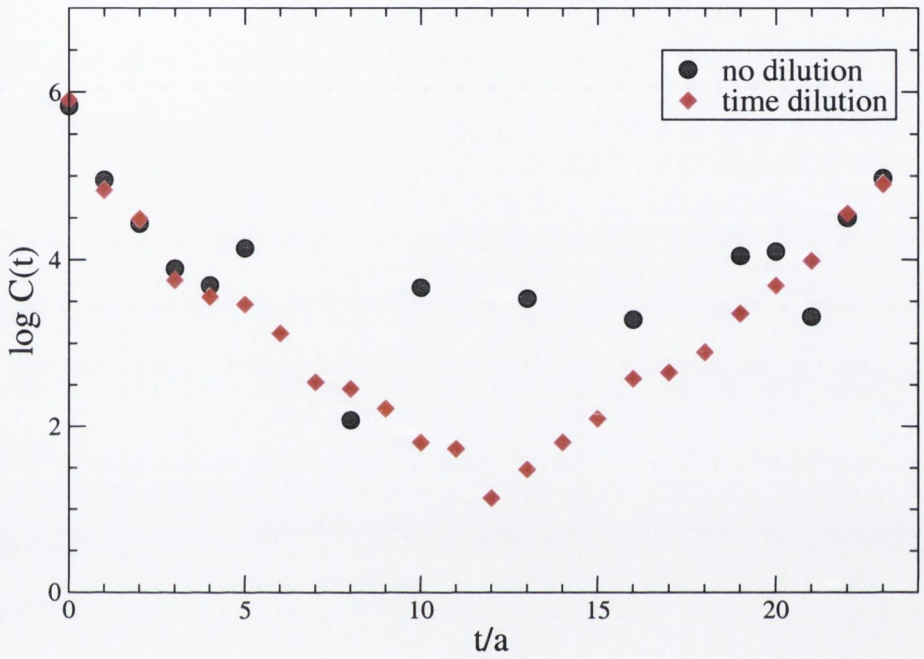

Figure 6-1: A comparison of a pseudoscalar correlator obtained using a pair of time-diluted noise vectors with a naive stochastic estimate which uses the same number of matrix inversions.

The all-to-all propagator algorithm used in this simulation incorporates an important additional feature. There is strong evidence to suggest that the low-lying eigenmodes of the fermion matrix play a particularly important role in hadronic interactions. This information suggests the the contribution of these low-lying modes to the fermion propagator should be computed exactly. This has been incorporated into a generalisation of the dilution algorithm in which the contribution of the lower-lying eigenmodes can be evaluated using a truncated spectral sum. The contribution of the higher eigenmodes is then estimated using the dilution algorithm. A suite of software has been developed which combines the truncated spectral sum and the diluted stochastic estimate in a seamless manner. The output from this program is a set of 'source' and 'solution' vectors, $\{\eta_i, \psi_i\}$, which are combined to form the full fermion propagator. The exact implementation of the program is described in detail

in Ref. [46].

6.5 Tuning anisotropies on a dynamical background

So far, we have described the tuning of the anisotropy parameters, ξ_q and ξ_g, in the quenched approximation. This allowed us to check that the mild mass dependence of the parameters of the fermion action is maintained beyond the tree-level. For physically realistic simulations, however, the anisotropy must be tuned on dynamical background configurations. When sea-quark effects are included ξ_g and ξ_q can no longer be determined separately, since the bare quark anisotropy will enter into the generation of gauge configurations through the fermionic determinant. Therefore, ξ_q and ξ_g must be tuned simultaneously so that the renormalised anisotropies determined from the static-quark potential and hadronic dispersion relations agree on the target value, ξ. The tuned point in the bare anisotropy parameter space is denoted (ξ_q^*, ξ_g^*).

The measured anisotropies for any set of bare values can be written as Taylor expansions about the tuned point. Close to the tuned point, to a good approximation, this gives the equation of a plane. For example, the measured quark anisotropy is

$$\xi_q^R(\xi_q, \xi_g) = \xi + \alpha(\xi_q - \xi_q^*) + \beta(\xi_g - \xi_g^*) \tag{6.21}$$

Setting the renormalised quark anisotropy to its target value defines a straight line in parameter space

$$\alpha\xi_q + \beta\xi_g = Q, \quad Q = \alpha\xi_q^* - \beta\xi_g^*. \tag{6.22}$$

Similarly, for the gauge anisotropy one can write

$$\gamma\xi_q + \delta\xi_g = G. \tag{6.23}$$

The intersection of these straight lines gives the tuned point, (ξ_q^*, ξ_g^*).

In order to solve for the intersection point we need the plane equations which define the renormalised anisotropies close to the target value. To do this we measure the quark and gauge anisotropies for three points in (ξ_q, ξ_g) parameter space which, guided by the results of the quenched study, we estimate to be close to the target point. These measurements yield the required planar equations.

The tuning procedure is intricate because three measurements must be made before the location of the target point can be estimated. The tuning runs may not be close enough to the target anisotropy for the planar approximations to hold. In addition, if the target point lies outside the area defined by the tuning runs, it may be difficult to determine ξ_q^* and ξ_g^* to the desired precision. The tuning of the dynamical configurations used in this study is described in more detail in Ref. [47].

6.6 Power divergences

The power divergence of the static quark self-energy arises because the reduced symmetries of the static limit allow the mixing of the derivative term, $\bar{h}D_0h$, appearing in the static quark action and the lower dimensional operator, $\bar{h}h$ [48]. At any rate, the exponents of the two-point correlators are not themselves physically meaningful. However, these power divergences cancel in the difference of the exponents allowing us to compute hadron mass differences.

6.7 Angular momentum on the lattice

The angular momentum and parity quantum numbers used to classify hadronic channels in the continuum correspond to irreducible representations (irreps) of the improper rotation group O(3), which is a symmetry group of these systems.

The irreducible representations include bosonic (single-valued) and fermionic (double-valued) representations of dimension $2J+1$. The projection of the angular momentum

onto some axis, J_z, labels the rows of the representation.

The lattice breaks continuum rotational symmetries and, on a spatially-isotropic lattice, O(3) reduces to the cubic point group O_h and eigenstates of the lattice Hamiltonian transform under definite irreducible representations of O_h. States which in the continuum have the same J^P quantum numbers but have different J_z values are, in general, separated across the lattice irreps. To reliably extract information from lattice correlators, it is necessary to use hadronic operators which couple strongly to particular lattice eigenstates. This is difficult to achieve using operators constructed according to continuum symmetries. We therefore construct interpolating operators which transform according to the irreps of O_h.

Using these operators, it should be possible to obtain good signals for the lowest-lying states in the lattice representations. It is then relatively straight-forward to determine the quantum numbers of these states. The Lattice Hadron Physics Collaboration is currently applying this approach to operator construction to the baryon spectrum on a grand scale [49, 50] and the construction of meson operators was discussed in Ref [51].

Irreducible representations of O_h

The cubic group O_h can be written as a direct product of two subgroups

$$O_h = O \times \{I, I_s\}, \tag{6.24}$$

where I_s denotes the space inversion operator and O is the group of proper rotations allowed by the isotropic cubic lattice.

We first consider the irreps of the subgroup O. This group has 24 elements which are divided into 5 conjugacy classes. With respect to Cartesian coordinate axes with the origin at the centre of a cube and the axes parallel to the edges of the cube the conjugacy classes and their constituent rotations are

- C_1 : the identity class.

- C_2 : an eight element class consisting of rotations of $\pm 2\pi/3$ about the body diagonals of the cube.
- C_3 : rotations of π about the coordinate axes (3 elements).
- C_4 : rotations of $\pm\pi/2$ about the coordinate axes (6 elements).
- C_5 : rotations of $\pm\pi$ about the planar diagonals of the cube (6 elements).

Because O is a finite group the number of conjugacy classes is equal to the number of single-valued irreducible representations. These consist of two 1-dimensional irreps labelled A_1 and A_2, a 2-dimensional irrep denoted E and two 3-dimensional representations, T_1 and T_2. Matrices for these representations can be found in Ref. [52].

To identify which continuum states can occur in a particular lattice representation, we note that O is a subgroup of SO(3). Therefore, restricting the irreps of SO(3) (labelled by J) to the rotations allowed by the lattice, generates representations for O which are, in general, reducible. This method of generating representations is known as subduction. The number of times a particular irreducible representation of O, labelled by the superscript α, occurs in the subduction of the continuum J irrep is given by

$$n_J^{(\alpha)} = \frac{1}{N_G} \sum_k n_k \chi_k^{(\alpha)} \chi_k^{(J)} \tag{6.25}$$

where N_G is the number of elements of the group, in this case $N_G = 24$, and k labels the conjugacy classes of that group. $\chi_k^{(\alpha)}$ is the character of the class k in the lattice irrep and $\chi_k^{(J)}$ is the corresponding character in the subduced representation. Note that the projection formula in Eq. 6.25 only holds for single-valued representations. Table 6.2 shows the subduction of the single-valued irreps of SO(3) to the group O for low-lying angular momenta.

To determine the fermionic representations of O, its double group O^D must be considered. This 48-element group is obtained by adding to O a negative identity

J	Irreducible representation of O
0	A_1
1	T_1
2	$E + T_1$
3	$A_2 + T_1 + T_2$

Table 6.2: Subduction of the single-valued irreducible representations of SO(3) to the group of proper cubic rotations, O.

corresponding to rotations through 2π. The double group is, therefore, the group of rotations in which one returns to the identity only after a rotation through 4π. This group has 8 single-valued irreps. In five of these, a rotation through 2π is represented by the identity matrix and these representations coincide with the single-valued irreps of O discussed above. The remaining three representations are labelled G_1, G_2 and H and these constitute the fermionic irreps of O. G_1 and G_2 are 2-dimensional representations and H is 4-dimensional. The full details of the representation matrices are not relevant to this discussion, however, we note that the matrices of G_1 are obtained by restricting SU(2) to the elements of O^D and that, on the lattice, 2-component spinors transform according to the G_1 representation.

The angular momentum content of these representations can again be determined using the projection formula in Eq. 6.25, where N_G now denotes the number of elements in O^D and the sum is over the 8 conjugacy classes of the double group. Table 6.3 summarises the irreducible representations of O and their low-lying constituent states.

So far, we have considered the irreducible representations of the group of proper rotations. However, the extension to O_h is clear: including spatial inversion simply doubles the number of irreps. For example, the single irrep R of the group O corresponds to the irreps R^g and R^u of O_h where the superscript g denotes an even-parity representation and u indicates an odd-parity representation.

Lattice irrep	Dimension	Continuum irreps
A_1	1	0, 4...
A_2	1	3, 5...
E	2	2, 4...
T_1	3	1, 3...
T_2	3	2, 3...
G_1	2	$\frac{1}{2}, \frac{7}{2}\ldots$
G_2	2	$\frac{5}{2}, \frac{7}{2}\ldots$
H	4	$\frac{3}{2}, \frac{5}{2}\ldots$

Table 6.3: Irreducible representations of the group of proper cubic rotations listed with their dimensions and lower lying angular momenta of their constituent states.

6.7.1 Constructing lattice operators

In this study, we make the static quark symmetries manifest at the outset and construct interpolating operators specifically for the light degrees of freedom. These operators are then combined with the static (anti)quark propagator to evaluate static-light correlation functions. For example, a two-point function for a hadron containing a single static quark is given by

$$C(t) \sim \langle \Omega | \ell^\dagger(t,x) W^\dagger(t,0;\mathbf{x}) \ell(0,\mathbf{x}) | \Omega \rangle, \tag{6.26}$$

where $W^\dagger$ is the path-ordered product of temporal links appearing in the static-quark propagator and ℓ is a colour-triplet combination of quark fields and link-variables. The projection matrix, P_+, appearing in the static-quark propagator is not shown because it can be incorporated into the choice of the light interpolating fields.

Under the action of an element, R, of the group O_h the interpolating operators transform according to

$$U(R) \ell_i^{(\alpha)} U^\dagger(R) = \sum_j \ell_j^{(\alpha)} D_{ij}^{(\alpha)}(R)^*, \tag{6.27}$$

where $U(R)$ represents the action of the group element, R, and $D^{(\alpha)}(R)$ is the corresponding matrix in the irrep labelled α.

To systematically construct interpolating operators for each of the lattice irreps we adopt the following procedure:

We identify linearly-independent sets of simple prototype functions which transform amongst themselves under O_h. For concreteness, consider the example of a static-light meson. In this case, suitable prototype operators are two-component spinors representing the light quark which may be displaced with respect to the static quark. In the following, we refer to the position of the static quark as the origin. The elemental operators are then two-component fields connected to the origin by a gauge-covariant path. We can use the upper or lower components of the four-component Dirac field in the prototype operators, noting that switching between components simply changes the parity of the representations.

The action of O_h on a set of prototype operators, denoted $\{\phi\}$, generates a representation of the group. Interpolating operators for the constituent irreps can be formed from linear combinations of the prototype functions. More specifically, consider the following set of operators

$$\{\phi_i^{(\alpha)}\} = P_{11}^{(\alpha)}\{\phi\}, \tag{6.28}$$

where the projection operator is defined as

$$P_{ij}^{(k)} = \frac{d_\alpha}{N_{O_h^D}} \sum_{R \in O_h^D} D_{ij}^{(\alpha)}(R)\mathcal{O}_R. \tag{6.29}$$

The sum is over elements of the double group, O_h^D, because the projection formula is only valid for single-valued representations. $\mathcal{O}_R$ denotes the operation of the group element, R, on the set $\{\phi\}$ and $D^{(\alpha)}(R)$ is the corresponding matrix in the α irrep which has dimension d_α. One chooses a (non-zero) element, $\ell_1^{(\alpha)}$, from the set in Eq. 6.28 and computes

$$\ell_i^{(\alpha)} = P_{i1}\ell_1^{(\alpha)}, \quad i = 2, ...d_\alpha. \tag{6.30}$$

The resulting set of operators, $\{\ell_i^{(\alpha)}\}$, transforms according to Eq. 6.27

For a static-light meson, the simplest interpolating operators are 2-component spinors located at the origin. The upper components of the light quark spinor form a G_1^g irrep, while the lower components transform according to the G_1^u representation. From Table 6.3 one can see that it is possible to probe the S-wave meson and $\frac{1}{2}^+$ P-wave meson using these operators, however spatially-extended operators are required to access other orbital excitations.

The simplest non-local operators can be constructed from the set of six elemental operators consisting of light quark spinors connected to the origin by straight-line paths of equal length. The paths of these prototype operators are perpendicular to the faces of the cube centred at the origin. From these basic units, it is possible to construct operators which transform according to the G_1^g, G_1^u, H^g and H^u irreps. To construct operators for the G_2^g and G_2^u irreps, we used spinors lying along the planar diagonals of the cube.

By repeating this for test functions with increasingly complex paths one can choose interpolating operators which maximise overlap with the states of interest.

The manipulations of the elemental operators required to project out the irreducible representations were performed using a program written in Mathematica.

6.8 Smearing and variational techniques

As well as constructing operators which coupled to definite irreducible representations of O_h, measurements were further enhanced by smearing the quark fields and link variables and applying a variational technique to compute hadron energies.

Quark smearing

Interpolating operators constructed from point-like quark sources do not generally have a good overlap with the low-lying states. This is because, physically, a quark is not expected to be restricted to a single point inside a hadron. Operators constructed

from smeared quark fields can have considerably larger overlap with the physical states.

In this study, we applied Jacobi smearing to the light quark fields. The smeared quark field is given by

$$\psi^{'}(x) = \left(1 + \frac{\kappa^2}{4n_\kappa}\triangle\right)^{n_\kappa} \psi(x), \tag{6.31}$$

where n_κ is the number of iterations of the smearing operator and κ is a real-valued weighting factor. The three-dimensional Laplacian operator is defined as

$$\triangle\psi(x) = \sum_{k=1}^{3} \left(U_k\psi(x+\hat{k}) + U_k^\dagger(x-\hat{k}) - 2\psi(x)\right). \tag{6.32}$$

The smearing procedure is gauge covariant and preserves the O_h symmetry. Smeared quark sources are not point-like but have a finite spatial distribution and better model the distribution of quarks inside hadrons.

Stout Links

Contamination by ultraviolet modes is further reduced by smearing the gauge fields. Link smearing is similar to quark smearing - each iteration of the smearing algorithm adds to each link variable a weighted sum of neighbouring links. For example, spatial links may be updated according to

$$U_i^{(n+1)}(x) = U_i^{(n)}(x) + \rho S_i^{(n)}(x), \tag{6.33}$$

where ρ is a real-valued weight factor and $S_i(x)$ denotes the sum of spatial staples going from the lattice site x to the site $x+\hat{\imath}$

$$S_i^{(n)}(x) = \sum_{j\neq i} U_j^{(n)}(x)U_i^{(n)}(x+\hat{\jmath})U_j^{\dagger(n)}(x+\hat{\imath}) + U_i^{\dagger(n)}(x-\hat{\jmath})U_i^{(n)}(x-\hat{\jmath})U_j^{(n)}(x-\hat{\jmath}+\hat{\imath}). \tag{6.34}$$

This smearing operation preserves the cubic symmetries of the lattice. The combination of links is not, however, an element of SU(3) and the smeared link must be projected back into the gauge group with each iteration of the smearing algorithm. The projection is non-analytic which can be problematic for Monte Carlo algorithms. To circumvent this problem, Morningstar and Peardon [53] developed a gauge-smearing algorithm which stays within SU(3), eliminating the need for link-variable projection. To do this, they defined the following matrix

$$Q_i(x) = \frac{i}{2}\left(\Omega_i^\dagger(x) - \Omega_i(x)\right) - \frac{i}{6}\mathrm{Tr}\left(\Omega_i^\dagger(x) - \Omega_i(x)\right), \tag{6.35}$$

where

$$\Omega_i(x) = \rho S_i(x) U_i^\dagger(x). \tag{6.36}$$

$Q_i(x)$ is hermitian and traceless and $e^{iQ_i(x)}$ is an element of SU(3). The smearing operation is given by

$$U_i^{(n+1)}(x) = \exp\left(iQ_i(x)\right) U_i^{(n)}(x), \tag{6.37}$$

and the smeared link, $U_i^{(n+1)}$, is an element of SU(3). Note that link smearing can be applied at separate stages of the simulation. On one hand, it enters into the generation of gauge configurations and quark propagators. A good choice of smearing parameters in that case are those which maximise the expectation value of the plaquette, which renders tadpole improvement unnecessary. In addition, link smearing may be used in the measurement procedure to maximise the overlap of the interpolating operators with the states of interest.

In this study, only the spatial links were smeared. In principle the smearing algorithm can be extended to include temporal links, however, on temporally-fine anisotropic lattices this is unnecessary.

The Variational approach

Rather than determining energies from the asymptotic behaviour of a single two-point correlation function, we employed a well-known variational technique [54, 55]. In this approach, for each channel, a number of different levels of Jacobi smearing are applied to the light quark fields and a correlator matrix is constructed. The energies of the low-lying states can then be determined from the eigenvalues of the correlator matrix at large times.

With point propagators additional inversions of the fermion matrix are required for each additional level of smearing. On the other hand, all-to-all propagators facilitate the use of the variational approach because the fermion propagator is expressed in terms of separable fields and smearing is only applied in the evaluation of the correlation matrix.

6.9 Simulation details

This study was performed on $N_f = 2$ dynamical background configurations. These configurations were generated using the anisotropic gauge action detailed in Chapter 2 and ARIA; the links in the fermion action were stout smeared and the gauge action was tadpole improved. The bare sea quark mass was set at $a_t m_0 = -0.057$ which corresponded to the strange quark mass in the quenched simulation. The anisotropy in these simulations was close to six but did require further tuning.

Initially, 250 configurations were generated on an $8^3 \times 48$ lattice. To begin with, only static-light mesons were considered. The mass of the light valence quark was fixed at the sea quark mass. The light quark propagator was computed using 100 eigenvectors and a single time diluted noise vector.

First, only S-wave and P-wave mesons were considered. On the lattice, the S-wave meson is in the G_1^- channel while the $\frac{1}{2}^+$ and $\frac{3}{2}^+$ are in the G_1^+ and H^+ channels respectively. The notation used here is the lattice analogue of the continuum J_ℓ^P notation, i.e. G_1 and H denote the transformation properties of the light degrees of freedom under proper rotations and the superscript denotes the overall parity of the meson. As mentioned earlier, extended operators were required for the H^+ meson and both local and extended operators were used for the G_1^- and G_1^+ mesons. The extended operators were constructed from the set of 6 prototype operators with straight-line offsets discussed earlier. Both single and double stout-link displacements were considered. Five levels of Jacobi smearing were applied to the light quark fields to construct a variational basis for the correlation matrices. For a given lattice representation, each element of the correlation matrix was obtained by averaging over the full set of basis operators.

The statistical errors on the resulting effective mass plots were extremely small, however, none of the plots showed a plateau. This is clearly illustrated in Figure 6-2 which plots the effective mass of the lowest-lying state in the G_1^- channel. The fall-off in the signal at large times is quite unexpected, because in static-light systems only

the light quark can propagate backwards in time and we expect this to be suppressed by gauge symmetry. Note, however, that this drift could not have been resolved in data with larger statistical errors.

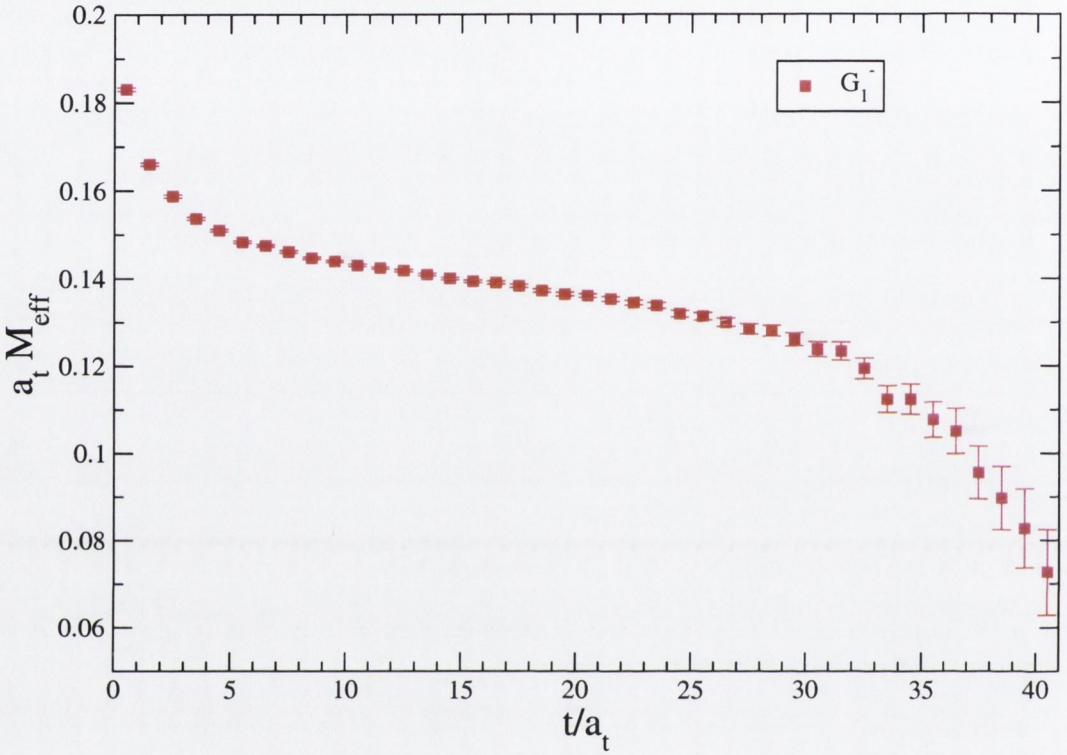

Figure 6-2: The effective binding energy for the lowest-lying state in the G_1^- irrep (the S-wave meson) obtained on the $8^3 \times 48$ lattice. The light quark propagator was evaluated using 100 low-lying eigenvectors and a single time-diluted noise vector. The drift in the effective binding energy could not have been resolved with poorer statistics.

The spatial lattice spacing, determined from the static inter-quark potential and confirmed in a study of the charmonium spectrum on the same background configurations, was found to be approximately 0.2 fm. This was smaller than had been anticipated and we suspected that the spurious drift in the effective masses was due to finite-size effects. Therefore, configurations were generated on an $8^3 \times 80$ lattice at the same coupling and sea quark mass. Preliminary measurements showed clear plateaux in effective masses. Time constraints meant that only 176 background configurations were generated. This time the light quark propagator was estimated using two time-diluted noise vectors.

The final results for the spectrum of static-light mesons were obtained using the following operators:

Local operators were used for the G_1^- channel. In this case the use of extended operators was found to have no noticeable impact on the signal. This is consistent with the the identification of the lowest-lying state in the G_1^- representation with the S-wave meson, which has a wave function that peaks at the origin. For the G_1^+ and H^+ channels, single-link displacements were used. Single-link displaced operators were also used for the H^- channel where we hoped to observe the $\frac{3}{2}^-$ D-wave meson. For this channel, we also tested planar-diagonal displacements but obtained a noisier signal. Finally, as stated earlier, diagonally-displaced operators were required for the G_2^- representation. In all cases, cleaner signals were obtained by coupling operators involving the lower components of the light quark spinor to a static quark and interpolating operators which involved upper components of the light quark fields to a static anti-quark. This is expected, of course, if one considers solutions to the Dirac equation in a simple static potential.

Once again, 5 levels of smearing were applied to the light quark fields to obtain a correlator matrix. For each element of the matrix, we averaged over all rows in the irreducible representation and we also averaged over both systems containing a static quark and systems containing a static anti-quark but with the same overall quantum numbers.

Figure 6-3 shows effective mass plots for the lowest-lying states in each of the irreducible representations. Clear signals are evident across all channels. From this figure, we draw the following conclusions. The lowest-lying state in the G_1^- channel can be identified unambiguously as the $\frac{1}{2}^+$ state. Splittings are observed between the lightest states in the G_1^+ and H^+ channels we identify as the two P-wave states. However, within errors no splitting is observed between the lowest energy states in the G_2^- and H^- channels. This may indicate that the D-wave states are (almost) degenerate or that the $\frac{5}{2}^-$ D-wave meson which appears in both channels is, in fact, lighter than the $\frac{3}{2}^-$ state. For heavy-light mesons, the inversion of orbitally-excited

multiplets with respect to the 'standard ordering' has been predicted by quark models [56, 57]. In these models, the spin-orbit coupling receives opposing contributions from single-gluon exchange and Thomas precession of the light quark in the confining part of the effective potential. At small inter-quark separation (i.e. low orbital angular momentum), one-gluon exchange dominates while at higher orbital angular momentum the contribution from Thomas precession takes over. Multiplet inversion

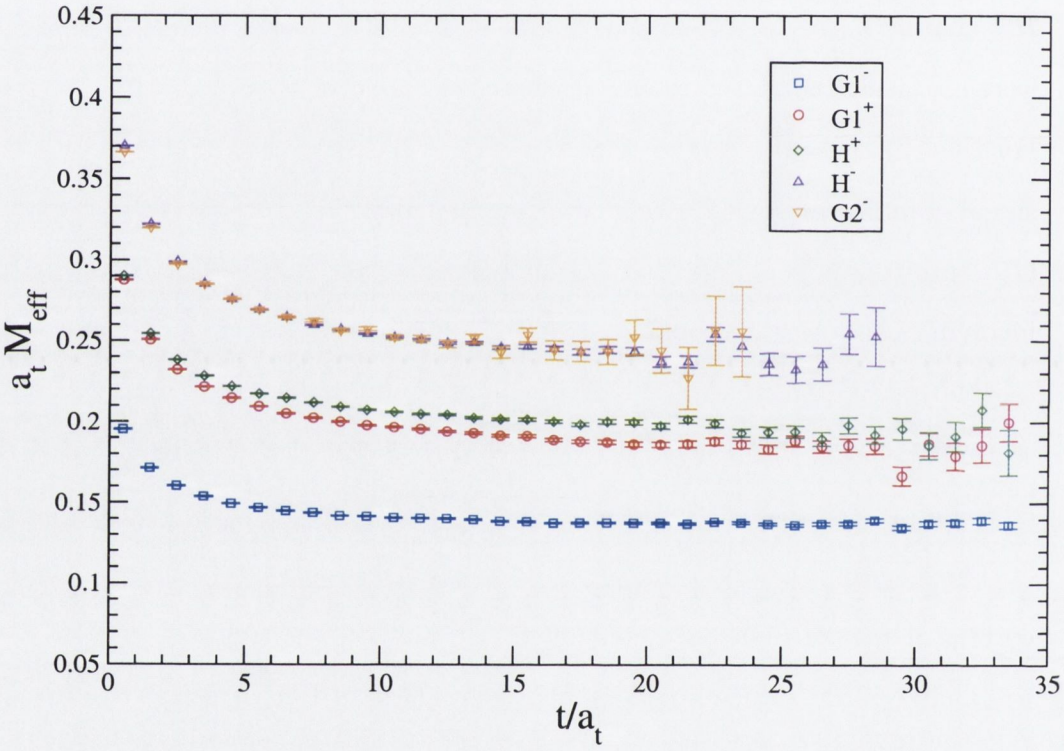

Figure 6-3: Effective mass plots for the static-light mesons

has been considered in a number of lattice studies of heavy-light mesons, more recently for static-light mesons on dynamical background configurations in Refs [58, 59]. The authors of those studies claim to identify non-degenerate D-wave states however the splitting between these states is extremely small and it is not clear whether that result is statistically significant. In any case, this is an interesting point that merits further study.

Mass-splittings

In the static-limit, only energy differences are of direct physical significance. In this study, hadron mass differences were determined to a high precision. Fits to the mass differences of mesons are shown in figure 6-4 to figure 6-6. Mass differences were determined by fitting to the ratio of correlators, however, in each case we demanded that both correlators exhibit individual plateaux in the fit region. Figure 6-4 shows a fit to the energy difference between the $\frac{1}{2}^+$ P-wave and the S-wave. The fit indicates an accuracy of 2% and, in lattice units, yields a value of 0.0481(8). Assuming an inverse temporal lattice spacing of $a_t^{-1} \sim 6$ GeV gives a result in physical units of just under 300 MeV. This is less than the value of 468(43)MeV obtained in another lattice study of the static-light spectrum [60], but it is not inconsistent with quark model predictions [61]. Also, we must emphasise that, although statistical uncertainties are clearly under control, we have not attempted to quantify systematic errors.

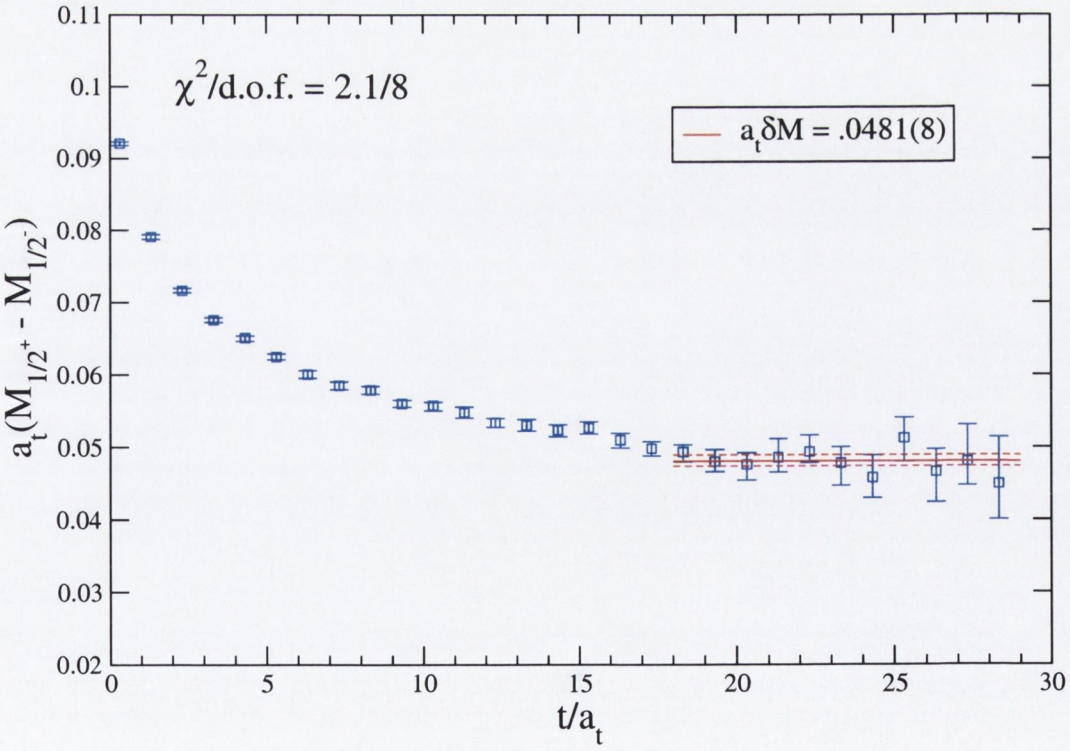

Figure 6-4: Mass splitting between the $\frac{1}{2}^+$ P-wave and S-wave static-light mesons.

Figure 6-5 shows the mass-splitting of the P-wave multiplet which yields $a_t\delta M = 0.0119(7)$. Although it appears that a plateau begins at about timeslice 6, this does not coincide with the plateau region of the individual states. Finally, the effective

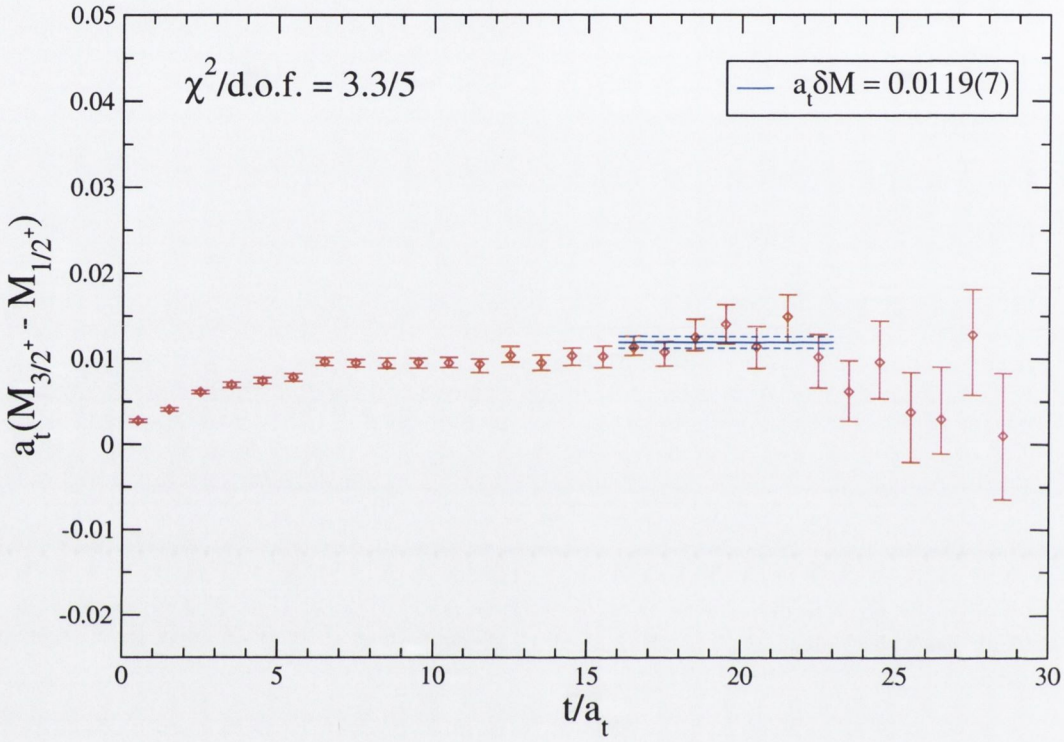

Figure 6-5: Mass splitting between the $\frac{3}{2}^+$ and $\frac{1}{2}^+$ P-wave states. The fit is performed in the region where both states exhibit a plateau.

energy difference between the lowest-lying state in the H^- channel and the S-wave meson is plotted in figure 6-6. The excellent fit, $a_t\delta M = 0.1073(7)$, can only be achieved because of the fine resolution of the temporal direction.

6.9.1 Static-light baryons

To compute the energies of the static-light baryons, we used local diquark operators. For the Λ_b channel, operators transforming according to the A_1^g irrep were used. The Σ_b required operators transforming according to the T_1^g irrep. These channels can be accessed using local operators. The operators used were

$$\mathcal{O}^a(A_1^g) = \epsilon^{abc}\psi_1^b C\gamma_5 \left(\frac{1 \pm \gamma_0}{2}\right)\psi_2^c, \quad \mathcal{O}_i^b(T_1^g) = \epsilon^{abc}\psi_1^b C\gamma_i \left(\frac{1 \pm \gamma_0}{2}\right)\psi_2^c, \qquad (6.38)$$

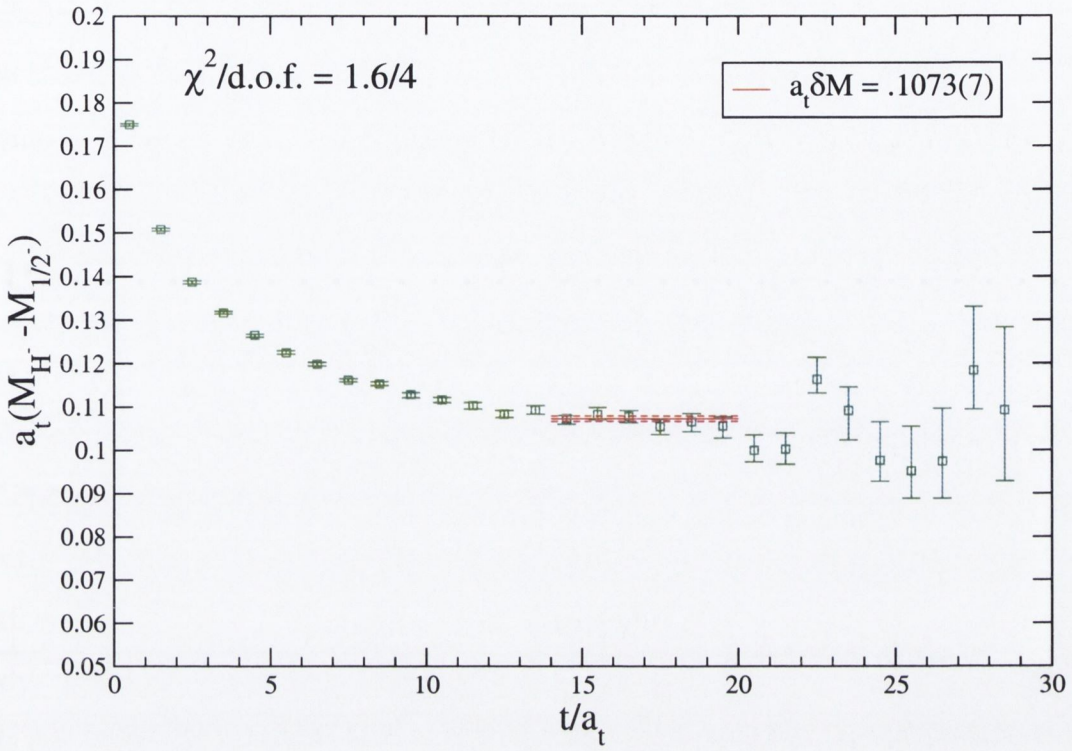

Figure 6-6: Mass splitting between the lowest-energy state in the H^- channel and the S-wave meson. As detailed in the text, we could not positively identify the H^- D-wave state.

where C is the charge conjugation matrix and ψ_i are the light quark fields. Preliminary results for the static-light baryons were presented at Lattice 2005 [62]. These results were obtained on 136 of the background configurations used for the static-light mesons. Each light quark propagator was evaluated using a single time-diluted noise vector. This time, cleaner signals were obtained by allowing the diquark states constructed from the large (upper) components of the light quark fields to propagate forwards in time and by using the lower components of the quark fields in the backward propagating states. Figure 6-7 shows the effective binding energies of the lowest-lying states in the baryonic (diquark) channels along with the S-wave static-light meson. One can clearly resolve splitting between the baryonic states. A preliminary estimate of the mass differences between the baryons and the static-light

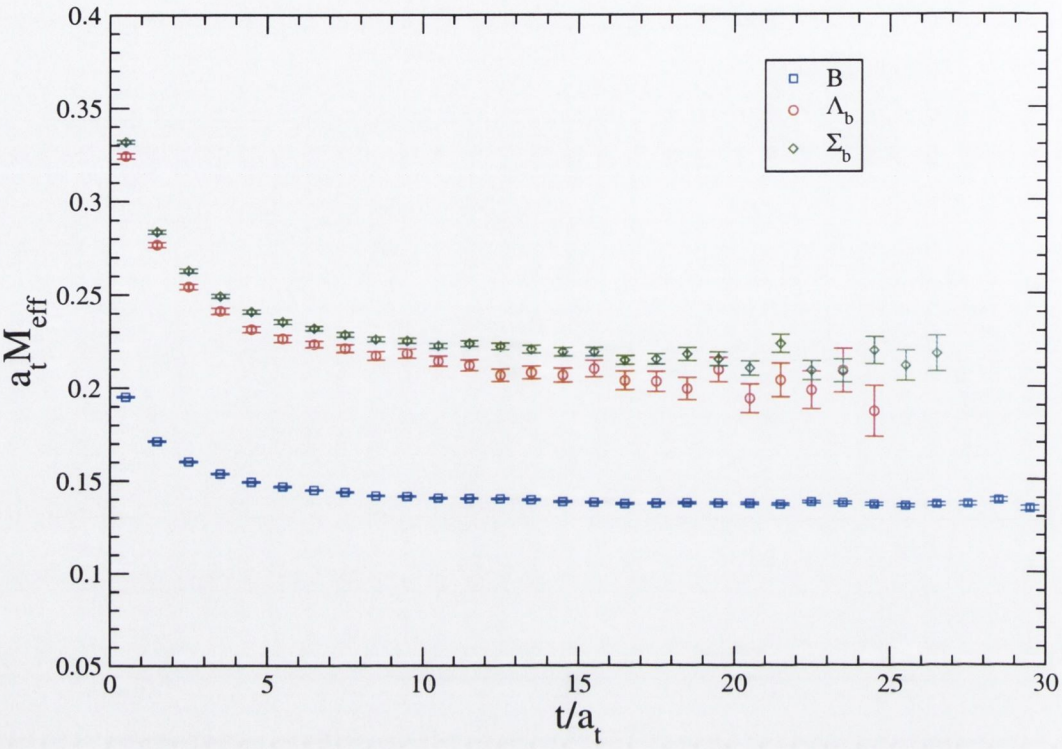

Figure 6-7: Effective mass plots for the static-light Λ_b and Σ_b together with the static-light S-wave meson.

mesons is, in lattice units,

$$a_t \delta M(\Lambda_b) = 0.0684(19),$$

$$a_t \delta M(\Sigma_b) = 0.0781(24).$$

The mass differences were, once again, determined by fitting to the ratio of correlators. In this case, the ratio of the baryonic correlators was too noisy too allow a reliable fit. However, from previous experience with mesons, we expect that using eigenvectors and higher levels of dilution for the light quark propagators should greatly improve the signals for these states. From the difference of the fits, we estimate a baryon splitting of $\delta(\Sigma_b - \Lambda_b) \sim 60$ MeV with a statistical uncertainty of about 40%.

Recently, a number of simulations of static-light baryons have been performed with a view to studying diquark correlations. One such study is presented in Ref [63]. That study involved a number of quark masses which were lighter than the single

quark mass used in this investigation. In that case, the binding energy differences were found to increase with decreasing light quark masses and those results were not inconsistent with our value for the baryon splitting.

6.10 Conclusions

This chapter described a study of the spectrum of static-light hadrons on dynamical background configurations. It combined a number of seemingly disparate topics.

Typically, static-light correlation functions are quite noisy. Using conventional point-propagators for the light quarks means that source and sink operators in a static-light two-point function are restricted to a few spatial lattice sites. In this study, to enhance the signal, all-to-all propagators were used for the light quarks. This allowed us to place source and sink operators at each spatial lattice site yielding a dramatic increase in statistics.

Our simulation was performed on an anisotropic lattice and we described how the quark and gluon anisotropies can be tuned on a dynamical background.

To maximise overlap with the states of interest, we used interpolating operators which transform under the irreducible representations of the lattice symmetry group, O_h. By constructing operators specifically for the light degrees of freedom it is possible to exploit static-light degeneracies to optimally determine hadron mass-splittings.

The focus of the study was the spectrum of orbitally excited mesons. P-wave and D-wave states were considered, most of which can only be accessed using spatially extended interpolating operators. All-to-all propagators facilitate the use of non-local operators. Furthermore, by constructing operators specifically for the light degrees of freedom, one can exploit static-light degeneracies to optimally determine the energy differences between hadrons.

In our results, one can clearly identify the static-light P-wave states. Excellent signals were also obtained for the G_2^- and H^- channels which contain the D-wave states. However, within errors, the lowest-lying states in these channels are degener-

ate. This might indicate inversion of the D-wave multiplet, which has been predicted by phenomenological models but has not previously been observed on the lattice. A more conclusive study must include an analysis of systematic errors and will identify higher-lying states in each lattice channel. In principle, higher orbital excitations as well as radial excitations can be identified by comparing excited states across the lattice irreps. In practice, this is a formidable task. However, strong signals for the ground states in each channel have been obtained using only time-diluted noise vectors, and the excellent signal obtained using a combination of eigenvectors and time-dilution on the $8^3 \times 48$ lattice indicates that progress can be made in this regard in the near future.

Finally, we considered static-light baryons which can be accessed using local operators. The two-point correlators for these channels were significantly noisier than for the static-light mesons. However, we are confident that clear signals can be obtained by using eigenvectors and higher levels of dilution in the evaluation of the light quark propagators.

Chapter 7

Concluding remarks

Lattice simulations of heavy quark systems, in particular simulations of hadrons containing b-quarks, are challenging. However, they are necessary to confirm that QCD is the true theory of the strong interaction and to search for physics beyond the Standard Model.

To overcome practical restrictions, a number of formalisms have been developed specifically for the heavy quark sector, these include NRQCD, the Fermilab formalism and HQET. Studies using these approaches have already achieved considerable success. The first part of this thesis constituted a feasibility study of an alternative approach to heavy hadron simulations, that is, the use of temporally-fine anisotropic lattices to suppress discretisation effects which scale with the mass of the heavy quark. The asymmetric discretisation of space-time introduces two additional parameters not associated with the isotropic formalism, the quark and gauge anisotropies, which must be appropriately tuned to regain continuum QCD. The anisotropic formalism will only be a viable option in heavy-quark simulations if these additional parameters are relatively straight-forward to tune and, as hoped, depend only mildly on the quark mass.

The non-perturbative tuning of the anisotropies on quenched background configurations was detailed in Chapter 4. In this case, the gauge anisotropy does not depend on the parameters of the fermion action and results for the fermion anisotropy were

promising, showing negligible variation over a range of quark masses.

Chapter 5 outlined a perturbative investigation of the fermion action. This was a preliminary study which laid the foundations for more advanced work. A naive comparison between the one-loop perturbative estimate for a simple quantity like the spatial tadpole coefficient and the corresponding value determined in a simulation showed poor quantitative agreement. However, it was argued that two-loop effects could account for such a discrepancy. Therefore, in light of recent advances in automating lattice perturbation theory, a fully perturbative approach to renormalisation may still be viable on spatially-coarse anisotropic lattices. This can be tested by performing a more comprehensive numerical investigation over a number of different lattice spacings and by computing the two-loop corrections explicitly.

The final chapter departed somewhat from the earlier theme and described a study of heavy-light hadrons in the static quark limit. Potentially, a lot can be learnt from static-light simulations although, conventionally, these have been less accurate than other approaches. A new method of computing all-to-all light quark propagators was described which yielded a dramatic improvement in the statistical accuracy of our results. As well as their obvious relevance to heavy-light spectroscopy, static-light simulations may also be used to explore the effect of quark correlations inside hadrons.

To summarise, this thesis describes a new toolkit for heavy quark simulations. Although much work has already been done in this area, considerable challenges remain and the continuing development of novel methods for heavy quark physics is of critical importance.

Appendix A

Lattice Feynman Rules

The infinite-volume Feynman rules required to compute the one-loop quark self-energy are as follows:

The gauge propagator

The inverse free gluon propagator is defined as

$$D^{-1}_{\mu\nu}(k) = \frac{1}{\alpha}\tilde{k}_\mu\tilde{k}_\nu + \sum_\beta \left(\tilde{k}_\beta\delta_{\mu\nu} - \tilde{k}_\mu\delta_{\beta\nu}\right) q_{\mu\beta}\tilde{k}_\beta, \tag{A.0.1}$$

where

$$\tilde{k}_\mu = \frac{2}{a_\mu}\sin\left(\frac{k_\mu a_\mu}{2}\right), \tag{A.0.2}$$

$$q_{\mu\nu} = (1-\delta_{\mu\nu})\left(1 + \frac{1}{12}[\bar{k}^2_\mu + \bar{k}^2_\nu]\right), \tag{A.0.3}$$

with

$$\begin{aligned} \bar{k}_0 &\equiv 0, \\ \bar{k}_i &\equiv a_s\tilde{k}_i, \quad i = 1,2,3. \end{aligned} \tag{A.0.4}$$

Then

$$D_{\mu\nu}(k) = \frac{1}{\left(\tilde{k}^2\right)^2}\left[(\alpha - G_{\mu\nu}(k))\tilde{k}_\mu\tilde{k}_\nu + \delta_{\mu\nu}\sum_\beta \tilde{k}_\beta^2 G_{\nu\beta}(k)\right], \tag{A.0.5}$$

where $G_{\mu\nu}$ is given in Ref [64],

$$\begin{aligned} G_{\mu\nu}(k) &= \frac{1}{\triangle_4}\left[\left(\tilde{k}^2 - \tilde{k}_\nu^2\right)\left(q_{\mu\rho}q_{\mu\tau}\tilde{k}_\mu^2 + q_{\mu\rho}q_{\rho\tau}\tilde{k}_\rho^2 + q_{\mu\tau}q_{\rho\tau}\tilde{k}_\tau^2\right)\right. \\ &+ \left(\tilde{k}^2 - \tilde{k}_\mu^2\right)\left(q_{\nu\rho}q_{\nu\tau}\tilde{k}_\nu^2 + q_{\nu\rho}q_{\rho\tau}\tilde{k}_\rho^2 + q_{\nu\tau}q_{\rho\tau}\tilde{k}_\tau^2\right) \\ &+ q_{\mu\rho}q_{\nu\tau}\left(\tilde{k}_\mu^2 + \tilde{k}_\rho^2\right)\left(\tilde{k}_\nu^2 + \tilde{k}_\tau^2\right) + q_{\mu\tau}q_{\nu\rho}\left(\tilde{k}_\mu^2 + \tilde{k}_\tau^2\right)\left(\tilde{k}_\nu^2 + \tilde{k}_\rho^2\right) \\ &- q_{\mu\nu}q_{\rho\tau}\left(\tilde{k}_\rho^2 + \tilde{k}_\tau^2\right)^2 - \left(q_{\mu\rho}q_{\nu\rho} + q_{\mu\tau}q_{\nu\tau}\right)\tilde{k}_\rho^2\tilde{k}_\tau^2 \\ &\left. - q_{\mu\nu}\left(q_{\mu\rho}\tilde{k}_\mu^2\tilde{k}_\tau^2 + q_{\mu\tau}\tilde{k}_\mu^2\tilde{k}_\rho^2 + q_{\nu\rho}\tilde{k}_\nu^2\tilde{k}_\tau^2 + q_{\nu\tau}\tilde{k}_\nu^2\tilde{k}_\rho^2\right)\right], \end{aligned} \tag{A.0.6}$$

with $\mu \neq \nu \neq \rho \neq \tau$, and $\triangle_4$ is given by

$$\triangle_4 = \sum_\mu \tilde{k}_\mu^2 \prod q_{\nu\mu} + \sum_{\mu>\nu,\rho>\tau,\{\rho,\tau\}\bigcap\{\mu,\nu\}=0} \tilde{k}_\mu^2\tilde{k}_\nu^2 q_{\mu\nu}\left(q_{\mu\rho}q_{\nu\tau} + q_{\mu\tau}q_{\nu\rho}\right) \tag{A.0.7}$$

The fermion propagator

For ARIA, the free fermion propagator is given by

$$S_0(p) = a_t\left(\frac{-i\gamma_\mu\mathcal{P}_\mu(p)\sin\left(a_\mu p_\mu\right) + \mathcal{M}(p)}{\sum_\mu\left(\mathcal{P}_\mu\sin\left(a_\mu p_\mu\right)\right)^2 + \mathcal{M}^2(p)}\right), \tag{A.0.8}$$

where

$$\mathcal{P}_0(p) \equiv 1, \tag{A.0.9}$$

$$\mathcal{P}_i(p) \equiv \frac{\mu_r}{\xi}\left(1 + \frac{2}{3}\sin^2\left(\frac{a_s p_i}{2}\right)\right), \quad i = 1,2,3;$$

$$\mathcal{M}(p) \equiv 2r\sin^2\left(\frac{a_t p_0}{2}\right) + \frac{16s}{\xi}\sum_j \sin^4\left(\frac{a_s p_j}{2}\right) + \mu_r a_t m_0. \tag{A.0.10}$$

1-Gluon–2-Quark vertex

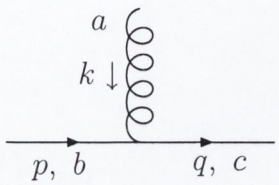

$$V_1(p,q,k,\mu,a) \;=\; -\lambda_\mu(p,q,k)T^a_{cb}, \tag{A.0.11}$$

where

$$\begin{aligned}\lambda_0(p,q,k) \;=\; & \gamma_0 \cos\left(\frac{a_t p_0 + a_t q_0}{2}\right) - ir \sin\left(\frac{a_t p_0 + a_t q_0}{2}\right) \\ & + \frac{1}{4\xi}\cos\left(\frac{a_t k_0}{2}\right)\sum_j \sigma_{j0}\sin(a_s k_j)\end{aligned} \tag{A.0.12}$$

$$\begin{aligned}\lambda_j(p,q,k) \;=\; & \mu_r \gamma_j \left[\frac{4}{3}\cos\left(\frac{a_s p_j + a_s q_j}{2}\right) - \frac{1}{3}\cos(a_s p_j + a_s q_j)\cos\left(\frac{a_t k_0}{2}\right)\right] \\ & -i4s\left[2\sin\left(\frac{a_s p_j + a_s q_j}{2}\right) - \sin(a_s p_j + a_s q_j)\cos\left(\frac{a_s k_j}{2}\right)\right] \\ & + \frac{1}{4}\cos\left(\frac{a_s k_j}{2}\right)\sigma_{0j}\sin(a_t k_0)\end{aligned} \tag{A.0.13}$$

2-Gluon–2-Quark vertex

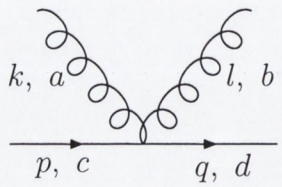

The temporal vertex is given by

$$\left[i\gamma_0 \frac{a_t}{2} \sin\left(\frac{a_t(p_0+q_0)}{2}\right) - \frac{a_t r}{2} \cos\left(\frac{a_t(p_0-q_0)}{2}\right)\right] \{T^a, T^b\}_{dc} \qquad \text{(A.0.14)}$$

and for spatial momenta

$$\left[i\gamma_j \mu_r a_s \left(\frac{2}{3} \sin\left(\frac{a_s(p_j+q_j)}{2}\right) - \frac{1}{3} \sin\left(a_s p_j + a_s q_j\right) \cos\left(\frac{a_s k_j}{2}\right) \cos\left(\frac{a_s l_j}{2}\right)\right)\right.$$
$$\left. -8a_s s \cos\left(\frac{a_s(p_j+q_j)}{2}\right) - 8a_s s \cos\left(a_s p_j + a_s q_j\right) \cos\left(\frac{a_s k_j}{2}\right) \cos\left(\frac{a_s l_j}{2}\right)\right] \{T^a, T^b\}_{dc} \qquad \text{(A.0.15)}$$

Bibliography

[1] H.B. Nielsen and M. Ninomiya, Nucl. Phys. B185, 20 (1981).

[2] C.T.H. Davies et al., Phys. Rev. Lett. 92, 022001 (2004).

[3] F. Maresca and M. Peardon, hep-lat/0411029.

[4] P.H. Ginsparg and K.G. Wilson, Phys. Rev. D25, 2649 (1982).

[5] K. Symanzik, Nucl. Phys. B226, 187 (1983).

[6] K. Symanzik, Nucl. Phys. B226, 205 (1983).

[7] M. Lüscher and P. Weisz, Commun. Math. Phys. 97, 59 (1985), Erratum-ibid. 98, 443 (1985).

[8] M. Lüscher and P. Weisz, Phys. Lett. B158, 250 (1985).

[9] M. Lüscher and P. Weisz, Nucl. Phys. B266, 309 (1986).

[10] M. Nobes, hep-lat/0501009.

[11] G.P. Lepage and B. Thacker, Phys. Rev D43, 196 (1991).

[12] G.P. LePage, L. Magnea, C. Nakhleh, U. Magnea and K. Hornbostel, Phys. Rev D46, 4052 (1992).

[13] G. Parisi, in High Energy Physics 1980, XX Int. Conf., edited by L. Durand and L.G. Pondrom (AIP, New York, 1981).

[14] G.P. Lepage and P.B. Mackenzie, Phys. Rev. D48, 2250 (1993).

[15] U. Heller, Phys. Lett. B362, 123 (1995).

[16] C. Morningstar and M. Peardon, Phys. Rev. D56, 4043 (1997), Phys. Rev D60, 034509 (1999).

[17] J. Harada, A. S. Kronfeld, H. Matsufuru, N. Nakajima, and T. Onogi, Phys. Rev D64, 074501 (2001), hep-lat/0103026.

[18] H.W. Hamber and C. M. Wu, Phys. Lett. B133, 351 (1983).

[19] S. Collins, R.G. Edwards, U.M. Heller and J.H. Sloan, Nucl. Phys. Proc. Suppl. 47, 455 (1996).

[20] A.S. Kronfeld, Nucl. Phys. Proc. Suppl. 53, 401 (1997).

[21] T.R. Klassen, Nucl. Phys. B533, 557 (1998).

[22] M. Alford, I.T. Drummond, R.R. Horgan, H. Shanahan, and M. Peardon, Phys. Rev D63, 074501 (2001), hep-lat/0003019.

[23] A. Hart, G.M. von Hippel, R.R. Horgan, L.C. Storoni, J. Comput. Phys. 209, 340 (2005).

[24] M. Nobes and H.D. Trottier, hep-lat/0309086.

[25] G.P. Lepage, J. Comput. Phys. 27, 192 (1978).

[26] A.X. El-Khadra, A.S. Kronfeld, and P.B. Mackenzie, Phys. Rev. D55, 3933 (1997).

[27] B.P.G. Mertens, A.S. Kronfeld, A.X. El-Khadra, Phys. Rev. D58, 034505 (1998).

[28] S. Hashimoto and M. Okamoto, Phys. Rev. D67, 114503 (2003).

[29] N.H. Shakespeare, H.D. Trottier, Phys. Rev. D58, 034502 (1998).

[30] H.J. Rothe, Lattice Gauge Theories: An Introduction, World Sci. Lect. Notes Phys. 59 (1997).

[31] R. Wohlert, DESY preprint 87-069 (1987).

[32] G. Parisi, Prolegomena to any future computer evaluation of the QCD mass spectrum. Invited talk at Summer Inst. Progress in Gauge Field Theory, Cargèse, France, Sep 1-15, 1983.

[33] Colin J. Morningstar and J. Shigemitsu, Phys. Rev. D57, 6741 (1998).

[34] Q.J. Mason, private communication.

[35] A. Hart, R.R. Horgan and L.C. Storoni, Phys. Rev. D70, 034501 (2004).

[36] N. Di Césaré, `http://acm.emath.fr/~dicesare`.

[37] C.T.H. Davies and B.A. Thacker, Phys. Rev. D45, 915 (1992).

[38] C. Morningstar, Phys. Rev. D48 2265 (1993); D50, 5902 (1994).

[39] S. Groote and J. Shigemitsu, Phys. Rev. D62, 014508 (2000).

[40] M. Della Morte, A. Shindler, R. Sommer, JHEP 0508, 051 (2005).

[41] Y. Kuramashi, Phys. Rev. D58, 034507 (1998).

[42] G.P. Lepage, Nucl. Phys. Proc. Suppl. 26, 45 (1992).

[43] E. Eichten and B. Hill, Phys. Lett. B240, 193 (1990).

[44] R.L. Jaffe, hep-ph/0507149.

[45] J. Foley, K.J. Juge, A. Ó Cais, M. Peardon, S.M. Ryan, J.I. Skullerud, hep-lat/0505023.

[46] A Ó Cais, Ph.D. thesis, School of Mathematics, Trinity College Dublin; submitted in November 2005.

[47] R. Morrin, M. Peardon and S.M. Ryan, hep-lat/0510016.

[48] G. Martinelli and C.T. Sachrajda, Phys. Lett. B354, 423 (1995).

[49] S. Basak et al., hep-lat/0506029.

[50] S. Basak et al., hep-lat/0506029.

[51] P. Lacock, C. Michael, P. Boyle, P. Rowland, Phys. Rev. D54, 6997 (1996).

[52] J.F. Cornwell, Group Theory in Physics - An Introduction (Academic Press).

[53] C. Morningstar and M. Peardon, Phys. Rev. D69, 054501 (2004).

[54] C. Michael, Nucl. Phys. B 259, 58 (1985).

[55] M. Lüscher and U. Wolff, Nucl. Phys. B 339, 222 (1990).

[56] H.J. Schnitzer, Phys. Lett. B226, 171 (1989).

[57] N. Isgur, Phys. Rev. D62, 014025 (2000).

[58] A.M. Green, J. Koponen, C. McNeile, C Michael, G. Thompson, Phys. Rev. D69, 094505 (2004).

[59] J. Koponen, hep-lat/0409087.

[60] G.S. Bali, Phys. Rev. D68, 071501 (2003).

[61] W.A. Bardeen, E.J. Eichten, C.T. Hill, Phys. Rev. D68, 054024 (2003).

[62] J. Foley, A. Ó Cais, M. Peardon, S.M. Ryan, J.I. Skullerud, PoS(LAT2005) 213 (2005).

[63] K. Orginos, PoS(LAT2005) 054 (2005).

[64] P. Weisz, Nucl. Phys. B212, 1 (1983), P. Weisz and R. Wohlert, Nucl. Phys. B236, 397 (1984); Erratum-ibid. B247, 544 (1984).